

Alfred Neuhold

**Structures of Buried Interfaces in
Organic Multilayer Devices: X-ray
Reflectivity Based Studies**

DOCTORAL THESIS

For obtaining the academic degree of
Doktor der technischen Wissenschaften

Doctoral Programme of Technical Sciences

Technical Physics



Graz University of Technology

Supervisor:

Ao. Univ.-Prof. Dipl.-Ing. Dr.techn. Roland Resel

Institute of Solid State Physics

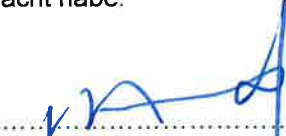
Graz, August 2012

Deutsche Fassung:
Beschluss der Curricula-Kommission für Bachelor-, Master- und Diplomstudien vom 10.11.2008
Genehmigung des Senates am 1.12.2008

EIDESSTATTLICHE ERKLÄRUNG

Ich erkläre an Eides statt, dass ich die vorliegende Arbeit selbstständig verfasst, andere als die angegebenen Quellen/Hilfsmittel nicht benutzt, und die den benutzten Quellen wörtlich und inhaltlich entnommene Stellen als solche kenntlich gemacht habe.

Graz, am 29.08.2012


.....
(Unterschrift)

Englische Fassung:

STATUTORY DECLARATION

I declare that I have authored this thesis independently, that I have not used other than the declared sources / resources, and that I have explicitly marked all material which has been quoted either literally or by content from the used sources.

29.08.2012
.....
date


.....
(signature)

To Setareh

Acknowledgments

First of all I want to thank my supervisor Ao. Univ.-Prof. Dipl.-Ing. Dr. techn. Roland Resel for giving me the opportunity to work in his group, for his scientific support and for guiding me through my PhD period. He allocated my funding and enabled me many conference and synchrotron stays. But more importantly I appreciated his open mind and patient attitude. He perfectly understands to give all of his group members enough space to find their own working style, which creates an amazing group atmosphere. Thank you Roland!

This work would also not be the same without my fantastic group members Tatjana Djuric, Heinz-Georg Flesch, Armin Moser, Markus Neuschitzer, Michael Dohr, Alexander Pichler, Christoph Lercher and Jirí Novák. Special thanks to my office colleague Reinhold Hetzel. All of you decisively supported me during my work. Furthermore I really enjoyed the amazing discussion about *the real way of life* in the last years. I personally learned a lot from each of you. Thank you!

Many thanks to my collaboration partners in the last three years, especially to the ISOTEC team like Stefanie Fladischer and Werner Grogger from the Institute for Electron Microscopy and Fine Structure Research & Graz Centre for Electron Microscopy and Elke Kraker and Bernd Lamprecht from the Institute for Surface Technologies and Photonics, Weiz. Without your outstanding knowledge about microscope investigations, sample preparation and the fruitful discussion about our work, this thesis would miss important contents. I also want to thank Ingo Salzmann (Humboldt Universität zu Berlin) and Detlef-M. Smilgies (CHESS, Ithaca) for supporting me during the synchrotron experiments.

Apart from our group I want to thank all of the people from the Institute of Solid State Physics. Especially Hannes Brandner, Simon J. Ausserlechner and Egbert Zojer for providing samples and important discussions. Special thanks to Birgit Kunert, Elisabeth Stern and Harald Kerschbaumer. I also want to thank Gabin Gbabode from the Université Libre de Bruxelles for his support with ellipsometry measurements and the group of Christian Teichert from the Montanuniversität Leoben, especially Stefan Lorbek for the microscope investigations.

For funding I want to acknowledge the Austrian Research Promotion Agency within the research project ISOTEC.

Special thanks go to the “4 GREAT M´S” (Manni, Marco, Michi, Mulla). Since the day I met these four guys at the very beginning of my study, we became deep friends, which hold now more than ten years. Thank you dudes for the awesome moments we had apart from studies.

Moreover, I want to thank my friends from the “Fössls Runde” for perfect moments we shared together, especially Marc for his deep friendship and the fantastic moments we spend together in the pure nature. I will not forget to thank my deep friends from Semriach for the amazing days together.

I would like to thank my family, my Mum, my Dad and my Brother for the support in every moment of my life. You always kept your faith in me and let me know that I am doing the right. Finally I deeply want to thank Setareh for supporting me mentally during my PhD period and I am proud to dedicate this doctoral thesis to you!

Preface

This doctoral thesis comprises the work I have done since autumn 2009 at the Institute of Solid State Physics at the Graz University of Technology. My work has been focused on buried interfaces of organic/inorganic multilayer thin film arrangements probed by several x-ray analysis methods. Such multilayer stacks are frequently used in organic semiconducting devices like thin film transistors, organic light emitting diodes or organic photodiodes. The knowledge of the interfacial structure can support the understanding of the device performance. After the introduction in chapter 1, the fundamental knowledge of x-ray scattering techniques and the experimental equipment – used through this work – are introduced (chapter 2). Chapter 3 contains an already published work about an x-ray reflectivity study combined with a microscope study of an organic/inorganic multilayer stack and the following chapter 4 contains a combined analytical study using transmission electron microscopy and x-ray reflectivity study of Ag diffusion into thin organic layers. Both studies have been done in cooperation with the Institute for Electron Microscopy and Fine Structure Research of the Graz University of Technology. The studies comprise decisive parts of x-ray analysis investigation performed by myself and microscope parts with the same weight performed by Stefanie Fladischer, who will submit the content of chapter 4 to a peer-reviewed journal. Chapter 5 shows an x-ray reflectivity investigation of an orthogonal soluble polymer stack, where the choice of the non-polar solvent can significantly change the interface morphology in between the polymers. This work will also be submitted to a scientific journal. Chapter 6 comprises an investigation of x-ray radiation damage on organic semiconducting materials during beam exposure. A comparison of the used simulation software packages will finalize this thesis (Appendix A).

Abstract

The study focuses on the characterization of the interface morphology in organic/inorganic as well as organic/organic multilayer stacks. The knowledge of the interface morphology in thin film is of fundamental interest for integrating them into an electric device, because the structure of interfaces significantly influences the device performance. In this work x-ray reflectivity measurements were used as the main investigation technique to probe buried interface morphologies and the obtained parameters were compared with parameters from several microscope techniques like atomic force microscopy, transmission electron microscopy and scanning electron microscopy. In addition, x-ray diffraction analysis like specular x-ray diffraction and grazing incidence diffraction were used to get an insight to the crystallographic structure of the used organic semiconducting materials. The main part of this thesis is assigned to the structural study of physical vacuum-deposited, organic multilayer films integrated into an organic/inorganic photodiode. The photodiode consists of a gold electrode, a silver top electrode and the organic materials *copper (II) phthalocyanine (CuPc)*, *perylene tetracarboxylic bisbenzimidazole (PTCBI)* and *aluminium-tris(8-hydroxyquinolin) (Alq₃)*, which are sandwiched in between the metal electrodes. X-ray analysis and microscopy methods reveal the roughness evolution and the crystallographic structure of the individual organic materials in the multilayer stack. Furthermore, the top organic/metallic interface of the photodiode was probed. The top silver electrode was prepared by several different deposition techniques and the possible diffusion of the metal ions into the subjacent organic layer, either *Alq₃* or *4,7-diphenyl-1,10-phenanthroline (Bphen)*, was examined by x-ray reflectivity measurements and transmission electron microscopy. Here, the investigations show Ag diffusion into the amorphous *Alq₃* layer, which could not be observed in the crystalline *Bphen* layer. A further part of this work covers the attempt of an interface investigation on an orthogonal soluble polymer stack. The organic semiconducting material *poly-(3-hexylthiophene) (P3HT)* was optionally dissolved in two different non-polar solvents (chloroform or toluene) and spin cast onto a water soluble *poly-(4-styrenesulfonic acid) (PSSA)* layer. The buried polymer/polymer interface was probed by x-ray reflectivity and the roughness parameters were cross checked by atomic force microscopy. Depending on the used *P3HT* solvent, the polymer/polymer interface shows significant variations of the interface and surface roughness. Grazing incidence x-ray diffraction was used to discover the molecular alignment within the thin films. Edge-on alignment of molecules was observed in the

toluene dissolved *P3HT* layer and face-on alignment for the chloroform dissolved *P3HT* layer. The polymer stack was additionally integrated into a bottom-gate top-contact transistor and the device performance could be related to the morphology of the polymer/polymer interface. Since the stability of soft matter materials during beam exposure is a crucial issue, the terminatory chapter of this thesis comprises a systematic investigation of radiation damage on organic semiconducting materials during x-ray beam exposure at synchrotron radiation facilities. Three frequently used organic semiconducting materials were compared. The observed structural material degradation of the investigated *P3HT* layer was connected to the measured beam exposure during the experiments. In contrast, the crystallographic structure of the vacuum deposited *α -sexithiophene* layer and the *pentacene* layer were not affected by the intense synchrotron x-ray radiation.

Kurzfassung

Im Rahmen dieser Dissertation wurden Grenzflächenuntersuchungen an organisch/organisch und organisch/anorganischen Vielschichtsystemen durchgeführt. Diese Vielschichtsysteme wurden in elektronische Bauteilen implementiert und beeinflussen maßgeblich deren elektrischen Eigenschaften. Aus diesem Grund sind Kenntnisse der Grenzflächenmorphologie in Vielschichtsystemen von essenzieller Bedeutung. In dieser Arbeit wurde die Röntgenreflexion an Oberflächen und Materialgrenzflächen als fundamentale Untersuchungsmethode gewählt. Die daraus gewonnenen Materialparameter wurden mit Resultaten aus der Rasterkraftmikroskopie, Transmissionsmikroskopie und Rasterelektronenmikroskopie verglichen. Anschließend wurden Röntgenstrukturuntersuchungen angewandt um die Kristallstruktur der halbleitenden, dünnen Schichten zu bestimmen. Der Hauptteil dieser Dissertation handelt von Strukturuntersuchungen von aufgedampften organischen Halbleiterschichten, welche Teilschichten einer organischen Fotodiode bilden. Die Fotodiode besteht aus einer Goldelektrode, einer abschließenden Silberelektrode und den dazwischen eingebetteten organischen Materialien *copper (II) phthalocyanine (CuPc)*, *perylene tetracarboxylic bisbenzimidazole (PTCBI)* und *aluminium-tris(8-hydroxyquinolin) (Alq₃)*. Der Fokus dieser Arbeit liegt in der Bestimmung der Rauheitsentwicklung an den Grenzflächen der organischen Materialien und in der Bestimmung der Kristallstruktur der einzelnen organischen Schichten. Des Weiteren wurde speziell die organisch/metallische Grenzfläche untersucht, wobei die oberste Silberschicht mit verschiedenen Aufbringetechniken hergestellt wurde. Dabei wurde die mögliche Metaldiffusion in die darunterliegenden organischen Schichten, entweder *Alq₃* oder *4,7-diphenyl-1,10-phenanthroline (Bphen)*, mittels Röntgenreflexion und Transmissionselektronmikroskopie untersucht. Die vermutete Ag Diffusion konnte nur in der amorphen *Alq₃* Schicht festgestellt werden. In kristalline *Bphen* Schicht konnten keine Silberpartikel festgestellt werden. Ein weiterer Teil dieser Arbeit handelt von Grenzflächenuntersuchungen an orthogonal löslichen Polymerschichten. Das organische, halbleitende Material *poly-(3-hexylthiophene) (P3HT)* wurde optional in zwei verschiedene Lösungsmittel (entweder Toluol oder Chloroform) gelöst und anschließend auf die polar lösliche *poly-(4-styrenesulfonic acid) (PSSA)* Schicht aufgebracht. Die entstandene Polymergrenzschicht wurde anschließend mit Röntgenreflexion gemessen und die daraus gewonnenen Rauheitswerte wurden mit einem Rasterkraftmikroskop verglichen. Weiters wurde die

kristallographische Molekülausrichtung in den dünnen Polymerschichten mittels Röntgenstrukturanalyse unter einem streifend einfallenden Röntgenstrahl bestimmt. Dabei wurde eine aufrecht stehende Ausrichtung der *P3HT* Moleküle entlang der Seitenketten festgestellt, wenn das Polymer in Toluol gelöst wurde und flach aufliegende Ausrichtung, wenn Chloroform als Lösungsmittel verwendet wurde. Die Polymerschichten wurden anschließend in einen Dünnschichttransistorapplikation integriert. Abhängig vom verwendeten Lösungsmittel änderte sich die Morphologie der Grenzfläche und damit auch die elektrischen Eigenschaften des Transistors. Der abschließende Teil dieser Dissertation befasst sich mit einer Strahlenfestigkeitsuntersuchung von ausgewählten, oft verwendeten, organischen Halbleitermaterialien welche auf Synchrotron-Großanlagen gemessen wurden. Die Materialien wurden bei energetisch hoher Röntgenstrahlung mittels Strukturanalysemethoden und Röntgenreflexionsmethoden untersucht. Dabei konnten strukturelle Änderungen in *P3HT* Schichten auf die Strahlenbelastung während des Experiments zurückgeführt werden. Im Gegensatz dazu wurden keine strukturellen Degradationen bei aufgedampften *α -sexithiophene* Schichten oder aufgedampften *pentacene* Schichten detektiert. Diese Materialien sind definitiv resistenter gegen intensive Strahlenbelastung.

Table of Contents

I. FUNDAMENTALS	14
1 Introduction	1-15
2 Scattering Theory	2-16
2.1 X-ray Interaction with Matter	2-16
2.2 Crystallography and Specular X-ray Diffraction (XRD)	2-18
2.3 X-ray Reflectivity (XRR) – Scattering Theory	2-23
2.3.1 The Index of Refraction.....	2-23
2.3.2 Snell-Descartes Law and Fresnel Reflectivity	2-26
2.3.3 XRR – The Parratt Formalism	2-30
2.3.4 XRR – The Matrix Method	2-35
2.4 XRR on Rough Surfaces.....	2-38
2.5 XRR Laboratory Equipment	2-44
2.5.1 Rockingcurves	2-48
2.6 Grazing Incidence X-ray Diffraction (GIXD).....	2-51
2.6.1 Fundamentals.....	2-51
2.6.2 GIXD Experimental Setups.....	2-54
II. EXPERIMENTAL	58
3 Structure and Morphology of an Organic/Inorganic Multilayer Stack: An X-ray Reflectivity Study	3-59
3.1 Motivation.....	3-59
3.2 Introduction.....	3-60
3.3 Experimental	3-61
3.4 Results and Discussion	3-64
3.5 Conclusion	3-73
3.6 Acknowledgement.....	3-74

3.7	Supplementary Information	3-75
3.7.1	Not Published Information	3-78
4	Diffusion of Ag into Organic Semiconducting Materials: A Combined Analytical Study Using Transmission Electron Microscopy and X-ray Reflectivity	4-81
4.1	Motivation.....	4-82
4.2	Introduction.....	4-83
4.3	Experimental Details	4-84
4.4	Results and Discussion	4-87
4.5	Conclusion	4-93
4.6	Acknowledgement.....	4-93
5	X-ray based tools for the investigation of buried interfaces in organic electronic devices	5-94
5.1	Motivation.....	5-94
5.2	Introduction.....	5-96
5.3	Experimental Section	5-97
5.3.1	Materials and Thin Film Preparation	5-97
5.3.2	Structural Investigations	5-99
5.3.3	Device Fabrication	5-100
5.4	Results and Discussion	5-100
5.4.1	XRR and AFM Results	5-100
5.4.2	Grazing incidence X-ray diffraction results	5-106
5.4.3	Device performance	5-108
5.5	Conclusion	5-110
5.5.1	Acknowledgements	5-111
6	X-ray radiation damage of organic semiconductor thin films during grazing incidence diffraction experiments	6-112

6.1	Motivation.....	6-112
6.2	Introduction.....	6-114
6.3	Materials and Methods	6-115
6.4	Results	6-116
6.5	Discussion.....	6-120
6.6	Conclusion	6-122
6.7	Acknowledgements	6-122
III.	APPENDIX A: XRR Software Comparison	123
A.1	Introduction.....	123
A.2	Software Introduction.....	124
A.3	Software Comparison.....	128
A.4	Conclusion	130
IV.	BIBLIOGRAPHY.....	131
V.	PUBLICATIONS	144
VI.	CONFERENCES.....	146
VII.	CURRICULUM VITAE.....	150

Part 1

I. FUNDAMENTALS

1 Introduction

X-ray diffraction analysis exists just 100 years, since Friedrich, Knipping and Laue discovered the phenomena of diffraction of x-rays by crystals in the year 1912. The diffraction effect occurs if the x-ray impinges on the periodic structure of a crystal and the wavelength of the radiation corresponds to the interatomic distances in the crystal, which is in the range of 0.15 to 0.4 nm. Constructive and destructive interference phenomena can be observed, when crystalline structures are exposed to x-rays in a specific manner.

In the last few decades x-ray scattering analysis frequently were used to investigate surfaces and interfaces of thin films due to their enormous significance in technological applications. Especially soft matter materials like liquid crystals, polymers, molecular glasses, molecular crystals or other materials are used as active materials or protective coatings in the semiconducting technology. Thin films with high quality surfaces and interfaces require characterisation techniques on atomic length scale. X-ray scattering techniques are puissant tools for structure analysis. In particular x-ray reflectivity can probe the layer thickness, the surface roughness and interface roughness as well as the variation of the electron density of thin films in the sub-nanometre regime.

However, x-ray scattering methods exhibit a non – neglecting drawback; only the amplitude of the scattered x-ray beam can be measured. The second important information of the phase is lost after the scattering process. In literature, this is often denoted as the *phase problem*. Hence no direct picture of the surface or interface of thin films can be observed. Complementary investigation methods like atomic force microscopy or transmission electron microscopy are often used to additionally illustrate complementary information about the material.

The following chapters will introduce the scattering theory following the textbooks by Metin Tolan (Tolan 1999), Jean Daillant and Alain Gibaud (Daillant & Gibaud 2009) and Jens-Als Nielsen(Als-Nielsen & McMorrow 2001).

2 Scattering Theory

2.1 X-ray Interaction with Matter

X-rays are electromagnetic waves with a wavelength in the range of $10^{-8} - 10^{-10}$ nm. The propagation of x-rays is described with an electric field vector of a monochromatic plane wave as

$$\mathbf{E}(\mathbf{r}) = E_0 e^{i(\mathbf{k}\cdot\mathbf{r} - \omega t)}, \quad (2.1)$$

where \mathbf{k} is the wave vector along the direction of propagation \mathbf{r} . In general, x-rays interact with the electric field of the electrons and negligibly weak with the atomic nuclei. Three fundamental events occur if an x-ray photon impinges into matter:

- elastic scattering
- inelastic scattering
- absorption

The inelastic interaction explains the partially energy loss of the photon in matter, which is the origin of the Compton Effect and Photo-Electric Effect (James 1982). During the absorption process, the energy of the x-ray photon is totally transferred to an atom. A subsequently event of photon emission with lower energy is called fluorescence. The third interaction process is the elastic scattering or Thomson scattering process (Thomson 1910). Here, the incoming radiation forces the electrons to oscillate with the same frequency and each electron becomes a source of dipole radiation with identical wavelength. If the phase relation between the incoming wave and the scattered wave stays constant, this process is called coherent elastic scattering, which is an additionally important difference to the Compton Effect. The latter effect is incoherent. During an elastic scattering process the energy of the interacting waves are conserved. However, the momentum may be transferred, which leads to the definition of the scattering vector $\mathbf{q} = (q_x, q_y, q_z)$ as

$$\hbar\mathbf{q} = \hbar\mathbf{k}' - \hbar\mathbf{k}, \quad (2.2)$$

where $\hbar\mathbf{k}$ and $\hbar\mathbf{k}'$ are the initial and final momenta of the photon. The theory of radiation frequently uses the wave number k instead of the wavelength λ , which is denoted as

$$|\mathbf{k}| = \frac{2\pi}{\lambda}. \quad (2.3)$$

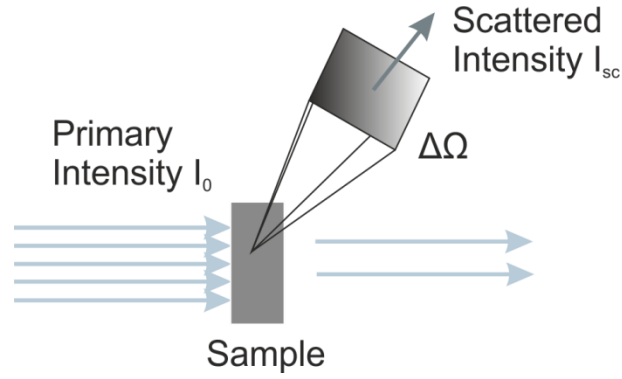


Figure 2.1: X-ray beam with an intensity I_0 impinge into matter and part of the intensity will be scattered I_{sc} under the solid angle $\Delta\Omega$.

The direction of the wave vector changes but not its magnitude:

$$|\mathbf{k}| = |\mathbf{k}'|. \quad (2.4)$$

Another very important quantity in scattering theory is the *differential scattering cross-section* ($d\sigma/d\Omega$), determining the flux of the scattered photons into an elementary solid angle $\Delta\Omega$, pointing towards the detector, and normalized by the incidence flux and the solid angle of the detector, $\Delta\Omega$ (Als-Nielsen & McMorrow 2001).

$$\left(\frac{d\sigma}{d\Omega} \right) = \frac{\text{number of x-ray photons scattered per second into } \Delta\Omega}{(\text{incident flux})(\Delta\Omega)} = \frac{I_{sc}}{(I_0 / A_0)(\Delta\Omega)} \quad (2.5)$$

where the incident flux Φ is defined by I_0/A_0 . I_0 is the incident beam intensity and A_0 is the cross section area (Figure 2.1). The incident x-ray beam impinges into the matter and the scattered intensity is calculated by

$$I_{sc} = \Phi \Delta\Omega \left(\frac{d\sigma}{d\Omega} \right) \quad (2.6)$$

The total cross-section for Thomson scattering is found by integrating the differential cross section over all possible scattering angles and has the dimension of an area [L^2] or barn.

The corresponding *absorption cross-section* σ_a is defined by

$$\sigma_a = \frac{W_{4\pi}}{\Phi} \quad (2.7)$$

where $W_{4\pi}$ is the number of absorption events. Here, the subscript 4π reminds us that the photoelectron liberated from the atom in the absorption process may be emitted into any direction in 4π steradians.

Depending on the x-ray source, the differential cross-section for Thomson scattering is

$$\left(\frac{d\sigma}{d\Omega}\right) = r_e^2 P \quad \text{with } P = \begin{cases} 1 & \text{synchrotron: vertical scattering plane} \\ \cos^2 \Theta & \text{synchrotron: horizontal scattering plane} \\ (1 + \cos^2 \Theta) / 2 & \text{unpolarized source (x-ray tube)} \end{cases} \quad (2.8)$$

where P is the polarization factor, Θ the scattering angle and r_e is the classical radius of the electron.

$$r_e = \frac{e^2}{4\pi\epsilon_0 m_e c^2} = 2.818 \times 10^{-15} \text{ m} \quad (2.9)$$

with the e is the elementary charge ($e = 1.602176565 \times 10^{-19} \text{ C}$), ϵ_0 is the vacuum permittivity ($\epsilon_0 = 8.854187817620 \times 10^{-12} \text{ As/Vm}$), m_e is the electron mass ($m_e = 9.10938291 \times 10^{-31} \text{ kg}$) and c is the speed of light ($c = 299792458 \text{ m/s}$).

2.2 Crystallography and Specular X-ray Diffraction (XRD)

In the ancient times of x-ray diffraction experiments only highly crystalline materials were investigated. Although this has changed in the last decades, x-ray diffraction analyses are still indispensable for crystal structure determination of single crystals, polycrystalline materials and semi - crystalline materials. Here, the basic ideas of crystallography and specular x-ray diffraction will be described. A detailed description can be found in the books of Weißmantel & Harmann (Weißmantel & Hamann 1995), Birkholz (Birkholz 2006) and Pietsch, Holý and Baumbach (Pietsch, Holy, & Baumbach 2004).

In general a crystal structure is theoretically described by its crystal lattice and its basis. The crystal lattice is mathematically described by an arrangement of points (point lattice), which contains the unit cell of the crystal and supports to describe symmetry operations within the crystal. The lattice is expressed by a right handed coordination system, which is not necessarily orthogonal. The amount and the position of atoms or molecules in the unit cell is determined by the basis. The three dimensional unit cell is a parallelepiped and is defined by the base vectors \mathbf{a} , \mathbf{b} , \mathbf{c} and the angles α , β and γ in between of them. A general lattice vector can be explicitly written as

$$\mathbf{R}_n = n_1 \mathbf{a} + n_2 \mathbf{b} + n_3 \mathbf{c} \quad (2.10)$$

with the integers n_1 , n_2 , n_3 .

In the field of x-ray diffraction analysis the diffraction phenomena are mostly represented in reciprocal space. One reason is the independency of the wavelength of the radiation used in different experimental setups (see below). The reciprocal space is directly related to the real space. Thus the unit vectors of the reciprocal unit cell are described by

$$\mathbf{a}^* = \frac{\mathbf{b} \times \mathbf{c}}{V}, \mathbf{b}^* = \frac{\mathbf{a} \times \mathbf{c}}{V}, \mathbf{c}^* = \frac{\mathbf{a} \times \mathbf{b}}{V} \quad (2.11)$$

where V denotes the volume of the unit cell in direct space. The unit cell in reciprocal space is now expressed by \mathbf{a}^* , \mathbf{b}^* , \mathbf{c}^* and its angles α^* , β^* , γ^* . The volume of the unit cell in reciprocal space $V^* = V^{-1}$. A general vector in reciprocal space is written as

$$\mathbf{G}_{hkl} = h\mathbf{a}^* + k\mathbf{b}^* + l\mathbf{c}^*. \quad (2.12)$$

The integer indices of eq. (2.12) are the so-called Miller indices (Miller 1839). This vector \mathbf{G} stands perpendicular to the lattice plane of the direct lattice. The length of \mathbf{G} is the reciprocal value of the lattice spacing d_{hkl} of the lattice plane (hkl), defined by

$$d_{hkl} = \frac{2\pi}{|\mathbf{G}_{hkl}|} \quad (2.13)$$

As described in section 2.1 the fundamental interaction process between x-ray radiation and matter is called Thomson scattering (Thomson 1910). The interaction process is mathematically described by the kinematic scattering theory or Born approximation, where the scattered wave inside the sample is equal to the wave outside and the investigated sample consists of a homogenous electron density distribution. Therefore, refraction is neglected, multiple scattering in the sample is not considered and the scattering amplitude is simply added up. Here, each electron of each illuminated atom in the material contributes to the scattering process. The total scattering length of each atom is defined by the atomic form factor f^0

$$f^0(\mathbf{q}) = \int \rho(\mathbf{r}) e^{i\mathbf{q} \cdot \mathbf{r}} d\mathbf{r}, \quad (2.14)$$

where $\rho(\mathbf{r})$ is the electron density of the material. In general the atomic scattering length $f(\mathbf{q})$ is a complex number written as

$$f(\mathbf{q}, \omega) = f^0(\mathbf{q}) + f'(\omega) + if''(\omega) \quad (2.15)$$

with the dispersion correction f' and f'' . It should be clear that the latter two variables depend on the energy (frequency ω) of the radiation (Als-Nielsen & McMorrow 2001). These terms are also known as resonant terms (see chapter 2.3.1).

Please note that all atoms in the unit cell as well as the position of the atoms in the crystal will contribute to the scattering process. Thus, the scattering amplitude $F(\mathbf{q})^{\text{crystal}}$ for a crystal is described by the structure factor of the unit cell and the sum over the lattice sites, written as

$$F^{\text{crystal}}(\mathbf{q}) = \sum_{\mathbf{r}_j} f_j(\mathbf{q}) e^{i\mathbf{q}\cdot\mathbf{r}_j} \sum_{\mathbf{R}_n} e^{i\mathbf{q}\cdot\mathbf{R}_n} = F(\mathbf{q}) \sum_{\mathbf{R}_n} e^{i\mathbf{q}\cdot\mathbf{R}_n}, \quad (2.16)$$

where \mathbf{R}_n are a set of lattice vectors determining the crystal, \mathbf{r}_j are the position of the atoms in the unit cell and $F(\mathbf{q})$ is the *structure factor*.

The contribution of the crystal lattice in eq. (2.16) can also be expressed by the so called Laue function or slit interference function

$$\left| \sum_{\mathbf{R}_n} e^{i\mathbf{q}\cdot\mathbf{R}_n} \right|^2 = \left| \sum_{n_1, n_2, n_3} e^{i\mathbf{q}(n_1\mathbf{a} + n_2\mathbf{b} + n_3\mathbf{c})} \right|^2 = \frac{\sin^2\left(\frac{n_1\mathbf{q}\cdot\mathbf{a}}{2}\right) \sin^2\left(\frac{n_2\mathbf{q}\cdot\mathbf{b}}{2}\right) \sin^2\left(\frac{n_3\mathbf{q}\cdot\mathbf{c}}{2}\right)}{\sin^2\left(\frac{\mathbf{q}\cdot\mathbf{a}}{2}\right) \sin^2\left(\frac{\mathbf{q}\cdot\mathbf{b}}{2}\right) \sin^2\left(\frac{\mathbf{q}\cdot\mathbf{c}}{2}\right)}, \quad (2.17)$$

which is only non-zero if

$$\mathbf{q}\cdot\mathbf{a} = 2\pi h; \quad \mathbf{q}\cdot\mathbf{b} = 2\pi k; \quad \mathbf{q}\cdot\mathbf{c} = 2\pi l. \quad (2.18)$$

The scattering intensity is proportional to the square of the structure factor

$$I = EE^* \sim |F(\mathbf{q})|^2 = F(\mathbf{q})F^*(\mathbf{q}), \quad (2.19)$$

or more accurately

$$I = EE^* = |F(\mathbf{q})|^2 \frac{\sin^2\left(\frac{n_1\mathbf{q}\cdot\mathbf{a}}{2}\right) \sin^2\left(\frac{n_2\mathbf{q}\cdot\mathbf{b}}{2}\right) \sin^2\left(\frac{n_3\mathbf{q}\cdot\mathbf{c}}{2}\right)}{\sin^2\left(\frac{\mathbf{q}\cdot\mathbf{a}}{2}\right) \sin^2\left(\frac{\mathbf{q}\cdot\mathbf{b}}{2}\right) \sin^2\left(\frac{\mathbf{q}\cdot\mathbf{c}}{2}\right)}. \quad (2.20)$$

The latter equation contains the so called *phase problem in structure determination*. Since the structure factor of the unit cell contains a complex term, the inverse transformation of eq. (2.19) to obtain the atomic position from the peak intensity is impossible.

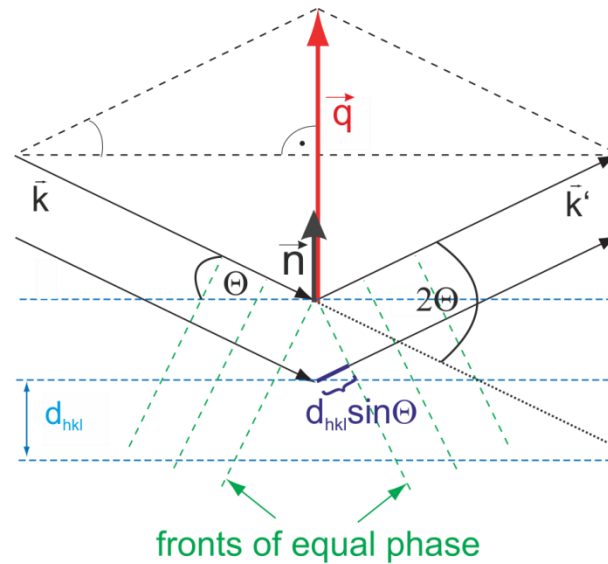


Figure 2.2: Scattering geometry on an arbitrary netplane. The scattering vector $\mathbf{q} = \mathbf{k}' - \mathbf{k}$ can be additionally estimated by eq. (2.23)

Combining eq. (2.11), eq. (2.12) and eq. (2.18), one gets the famous **Laue condition** for diffraction:

$$\mathbf{q} = \mathbf{G} \quad (2.21)$$

The latter condition shows that the scattering vector \mathbf{q} has to be identical with a reciprocal space vector \mathbf{G} to get constructive interference in diffraction experiment. Now the physical meaning of the reciprocal lattice can be understood in the following way; an arbitrary set of integers h, k, l , i.e., an arbitrary reciprocal vector \mathbf{G}_{hkl} (eq. (2.12)) leads to a scattering vector \mathbf{q} that satisfies the Laue equations. Hence, the allowed values for constructive interference from a three dimensional lattice, the reciprocal lattice, which exhibiting base vectors. This vectors are pairwise orthogonal to the direct vectors in the real space and therefore define the diffracting crystal itself.

In real space diffraction is described with two conditions, the **parallelism condition** and **Bragg's law**, illustrated in Figure 2.2.

- The **parallelism condition** just presupposes that the crystal has to be placed in such a way that the normal vector \mathbf{n} of the investigated netplane (hkl) is parallel to the scattering vector \mathbf{q} .
- **Bragg's law** expresses the fact, that constructive interference will only be observable under specific diffraction angles 2θ and if the wavelength λ of the radiation is in the range of the lattice plane distance d_{hkl} :

$$\lambda = 2d_{\text{hkl}} \sin\left(\frac{2\Theta}{2}\right) \quad (2.22)$$

To achieve a diffraction feature, these two conditions have to be fulfilled simultaneously during the diffraction experiment. The scattering vector in z-direction can also be expressed by

$$q_z = \frac{4\pi}{\lambda} \sin\frac{2\Theta}{2}, \quad (2.23)$$

which has the big advantage that one can compare the measured data independent of the wavelength of the x-ray source. In general the scattering vector $\mathbf{q} = (q_x, q_y, q_z)$ comprises three components. Depending on the nature of the experiment only some of these components have to be considered. E.g. in a specular scan only variations of q_z are measured. In the chapter 2.6 grazing incidence x-ray diffraction will be introduced, where the other two components of the scattering vector additionally get useful due to the fact that this diffraction analysis comprises information of the in-plane structure of crystals. Depending on the experimental setup (goniometer geometry) the data will be represented in so-called *reciprocal space maps*, which are two dimensional intensity plots with the out-of-plane coordinates q_z and the in-plane coordinate $q_p = \sqrt{q_x^2 + q_y^2}$ (Moser 2012).

2.3 X-ray Reflectivity (XRR) – Scattering Theory

Scattering of electromagnetic waves is explained by introducing the index of refraction $n(\mathbf{r})$ and solving the Maxwell equations in consideration of specific boundary conditions, which are appearing if electromagnetic waves enter from vacuum into a medium (Born, Wolf, & Bhatia 1999).

2.3.1 The Index of Refraction

The propagation of electromagnetic radiation in vacuum can be represented by a 4 - vector potential E_τ ($\tau = 0, 1, 2, 3$) defined by (Daillant & Gibaud 2009)

$$E_0 = \frac{\Phi}{c}, \quad (E_1, E_2, E_3) = \mathbf{E} \quad (2.24)$$

where Φ is the scalar electric potential and \mathbf{E} is the 3 - vector potential. The E_τ follows the Lorentz gauge and excluding charges gives

$$\Delta E_\tau = \frac{1}{c^2} \frac{\partial^2 E_\tau}{\partial t^2}, \quad \Delta = \sum_{x_i=x,y,z} \frac{\partial^2}{\partial x_i^2} \quad (2.25)$$

where c is the speed of light. If we exclude time-depend problems and consider monochromatic radiation, we will end up with the well suiting **Helmholtz equation**, that describes the propagation of plane waves with the wave vector k_0 .

$$(\Delta + k_0^2)E = 0 \quad (2.26)$$

Regarding the propagation of electromagnetic radiation within a medium extends eq. (2.26) with the index of refraction $n(\mathbf{r})$, characterized by the permittivity ϵ and the permeability μ of the medium. Here we assume just homogenous and isotropic mediums, which is naturally not the case.

$$\Delta_r \mathbf{E}(\mathbf{r}) + k^2 n^2(\mathbf{r}) \mathbf{E}(\mathbf{r}) = 0 \quad (2.27)$$

with

$$n(\mathbf{r}) = \sqrt{\frac{\epsilon \mu}{\epsilon_0 \mu_0}} \approx \sqrt{\epsilon_r} \quad (2.28)$$

where μ and ϵ are the permeabilities in the medium and μ_0 and ϵ_0 permeabilities in vacuum. The wave vector simply has changed by the refraction index $n(\mathbf{r})$, which is defined as the ratio of the speed of light c_0 in vacuum to the phase speed of light ($c_M = c_0/n$)

in the medium. One has to know the refractive index of the medium to understand the interaction processes between matters and x-rays. The classical model to describe the interaction processes are elastically bound electrons to a rigid grid of atoms. The fundamental equation of an applied motion in an electromagnetic field yields

$$m \frac{d^2 \mathbf{r}}{dt^2} + h \frac{d\mathbf{r}}{dt} + k\mathbf{r} = -e\mathbf{E} \quad (2.29)$$

where h is a friction coefficient and k is the spring constant. The solution of the eq. (2.29) shows that the electrons follow the behaviour of a harmonic oscillator and the displacement of the electrons is described by

$$\mathbf{r} = \frac{-e}{m(\omega_0^2 - \omega^2) + i\omega \frac{h}{m}} \mathbf{E} e^{i\omega t} \quad (2.30)$$

where $\omega_0 = \sqrt{k/m}$ is the eigen pulsation of the electron pounded to the nucleus and ω is the frequency of the x-ray radiation.

The atomic scattering length of a single oscillator is defined to be the amplitude of the outgoing spherical wave and can be written in units of r_e as

$$f_s = \frac{\omega^2}{(\omega^2 - \omega_0^2 + i\omega h)} \quad (2.31)$$

We now have to distinguish between three possible frequency regimes, either $\omega_0 \gg \omega$, $\omega_0 = \omega$ and $\omega_0 \ll \omega$.

$\omega_0 \gg \omega$: Rayleigh scattering, which describes the scattering of the visible light at gases or small particles. The total scattering cross section can be written as

$$\sigma_T = \left(\frac{8\pi}{3} \right) \left(\frac{\omega}{\omega_0} \right)^4 r_e^2 \quad (2.32)$$

$\omega_0 = \omega$: If the eigen frequency of the electron is equal to the frequency of the incoming radiation, one has to include the dispersion correction into eq. (2.31). The dispersion correction contains the real part f_s' and an imaginary part f_s'' , which are also called resonant terms. The following absorption cross section σ_a of a single oscillator can be presented by a delta function centred at $\omega_0 = \omega$

$$\sigma_{a,s}(\omega) = 4\pi r_e c \delta(\omega - \omega_0) \quad (2.33)$$

where the phase speed of light c is given by ω/k .

$\omega_0 \ll \omega$: The electron can be considered as free (Thomson scattering) and $f_s = 1$ ($= r_e$). Here the total scattering cross section per electron is estimated by

$$\sigma_T = \left(\frac{8\pi}{3} \right) r_e^2 \quad (2.34)$$

Since for x-rays $\omega_0 \ll \omega$, one can assume that far from the absorption edge

$$\mathbf{r} \approx \frac{e\mathbf{E}}{m\omega^2}. \quad (2.35)$$

Considering the dielectric polarisation \mathbf{P} ,

$$\mathbf{P} = \epsilon_0 \chi \mathbf{E} = -\frac{\rho_e \mathbf{E}}{m\omega^2} \quad (2.36)$$

where ρ_e is the electron density and χ the dielectric susceptibility that can be written

$$\chi = \epsilon_r - 1 = -\frac{\rho_e e^2}{\epsilon_0 m \omega^2}. \quad (2.37)$$

For $\chi \ll 1$, the refractive index n is expressed

$$n = \sqrt{\epsilon_r} = 1 - \frac{\rho_e e^2}{2\epsilon_0 m \omega^2}. \quad (2.38)$$

Including the classical radius r_e gives a refractive index of

$$n(\mathbf{r}) = 1 - \frac{r_e \rho_e(\mathbf{r}) \lambda^2}{2\pi} = 1 - \delta(\mathbf{r}). \quad (2.39)$$

Considering the absorption modifies the index of refraction to

$$n(\mathbf{r}) = 1 - \frac{r_e \rho_e(\mathbf{r}) \lambda^2}{2\pi} + i \frac{\lambda}{4\pi} \mu(\mathbf{r}) = 1 - \delta + i\beta, \quad (2.40)$$

where μ is the linear absorption coefficient of the material, ρ_e is the number of electrons per unit volume and λ is the wavelength of the radiation. ρ_e is well known for crystalline materials due to the distinct unit cell.

Typical values for the dispersion δ are in the range of $10^{-5} - 10^{-6}$ and the absorption values β are 10^{-7} to 10^{-8} . For x-rays, δ is always positive; hence the index of refraction is slightly smaller than unity and therefore the phenomena of **total external reflection** can occur.

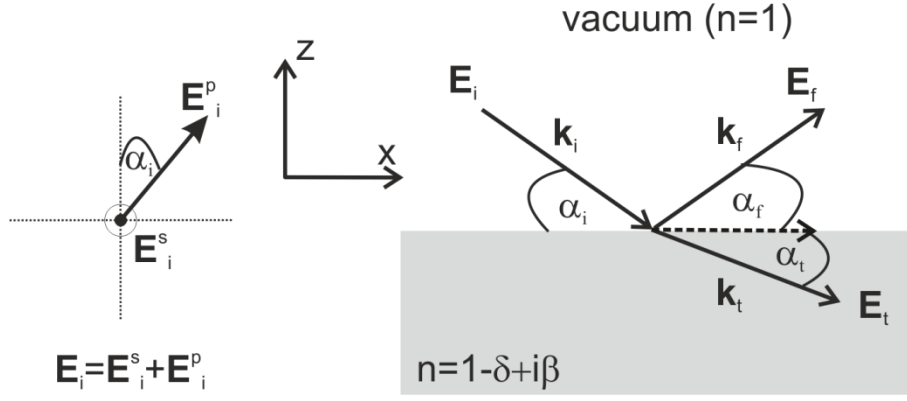


Figure 2.3: The wave field \mathbf{E}_i is split into a part perpendicular (\mathbf{E}_i^s) and parallel (\mathbf{E}_i^p) to the plane of incidence (x,z-plane) (left). Schema of a reflection and transmission of an incident wave polarised along y and travelling in the x-z plane of incidence (right).

2.3.2 Snell-Descartes Law and Fresnel Reflectivity

As described in the previous chapter, the propagation of an electromagnetic wave in a homogenous medium is explained by the Helmholtz Equation (2.27) and the solutions of it are plane waves eq. (2.1). If the plane wave impinges into an ideally flat surface, the linearly polarized, incident wave ($\mathbf{E}_i(\mathbf{r}, t) = \mathbf{E}_i e^{i(\mathbf{k}_i \cdot \mathbf{r} - \omega_i t)}$) can be expressed by its component parallel \mathbf{E}_i^p to the plane of incidence (p-polarized) and perpendicular \mathbf{E}_i^s to the plane of incidence (s-polarized) (Figure 2.3, left). The impinging incident wave will split in one part which is reflected ($\mathbf{E}_r(\mathbf{r}, t) = \mathbf{E}_r e^{i(\mathbf{k}_r \cdot \mathbf{r} - \omega_r t)}$) at the surface and another part which is transmitted ($\mathbf{E}_t(\mathbf{r}, t) = \mathbf{E}_t e^{i(\mathbf{k}_t \cdot \mathbf{r} - \omega_t t)}$). The electrical fields of both refracted parts can also be expressed by an s-polarized component and a p-polarized component. Figure 2.3 (right) illustrates refraction of a plane wave, which is polarised into the y direction and propagate along the x-z plane. The components of the wave vectors of the individual electric fields are given as

$$\begin{pmatrix} \mathbf{k}_i \\ \mathbf{k}_r \\ \mathbf{k}_t \end{pmatrix} = \begin{pmatrix} k_0 \cos(\alpha_i) \mathbf{e}_x + k_0 \sin(\alpha_i) \mathbf{e}_z \\ k_0 \cos(\alpha_r) \mathbf{e}_x + k_0 \sin(\alpha_r) \mathbf{e}_z \\ k_0 \cos(\alpha_t) \mathbf{e}_x - k_0 \sin(\alpha_t) \mathbf{e}_z \end{pmatrix} \quad (2.41)$$

Due to the boundary conditions, the tangential component of the electric field must be continuous at the interface ($z = 0$). If one assumes that the transmitted beam is completely absorbed by the medium the following expression is fulfilled:

$$\mathbf{E}_i e^{i(k_0 \cos(\alpha_i) \mathbf{e}_x - \omega_i t)} + \mathbf{E}_r e^{i(k_0 \cos(\alpha_r) \mathbf{e}_x - \omega_r t)} = \mathbf{E}_t e^{i(k_0 \cos(\alpha_t) \mathbf{e}_x - \omega_t t)} \quad (2.42)$$

Using the fact that $k_0 = |k_i| = |k_r| = |k_f| = 2\pi/\lambda$, $\omega \equiv \omega_i = \omega_f = \omega_t$ at $\mathbf{e}_x = 0$ at $t = 0$ simplifies eq. (2.42) and leads to the law of reflection

$$\alpha_i = \alpha_f. \quad (2.43)$$

Considering $k_t = n\omega/c_0$ gives the **Law of Snell – Descartes**

$$\cos(\alpha_i) = n \cos(\alpha_t) \quad (2.44)$$

and one can now easily understand the phenomena of total external reflection. Due to the fact that the index of refraction n is always smaller than unity there exists a critical angle α_c of incidence, where no beam impinges into the medium (dashed arrow in Figure 2.3). Setting $\alpha_t = 0$ and using the index of refraction for x-rays without absorption modifies the law of Snell-Descartes in the following way

$$\cos(\alpha_c) = n = 1 - \delta \quad (2.45)$$

For small angles, $\cos(\alpha_c)$ can be approximated as $1 - \alpha_c^2/2$. Using the latter fact together with eq. (2.39) and eq. (2.45), the **critical angle of total external reflection** α_c given by:

$$\alpha_c = \sqrt{\frac{\lambda^2 r_e \rho_e}{\pi}} \quad (2.46)$$

The critical angle directly includes the value of the absolute electron density ρ_e of the medium at a given x-ray wavelength λ . The magnitude of the critical angle is in a range of 0.22° for silicon with CuK_α radiation and even smaller for organic materials due to the lower electron densities (Tolan 1999).

Considering the Maxwell equations together with the boundary conditions one can describe the amplitudes of the electric field as

$$E_i + E_r = E_t. \quad (2.47)$$

One can now simply determine the coefficient for reflection $r = E_r/E_i$ and the coefficient of transmission $t = E_t/E_i$. Using the z - component of the incoming ($k_{i,z}$) and the transmitted ($k_{t,z}$) wave vector, the reflection and transmission coefficient becomes

$$k_{i,z} = k \sin(\alpha_i) \text{ and} \quad (2.48)$$

$$k_{t,z} = k \sqrt{n^2 - \cos^2(\alpha_i)} \approx k \sqrt{\alpha_i^2 - \alpha_c^2} \quad (2.49)$$

and the **Fresnel formulas for s-polarized waves** can be written as (Born, Wolf, & Bhatia 1999):

$$r_s = \frac{k_{i,z} - k_{t,z}}{k_{i,z} + k_{t,z}} \quad (2.50)$$

$$t_s = \frac{2k_{i,z}}{k_{i,z} + k_{t,z}} \quad (2.51)$$

In case of **p-polarized waves** one gets the following Fresnel equations (Born, Wolf, & Bhatia 1999):

$$r_p = \frac{n^2 k_{i,z} - k_{t,z}}{n^2 k_{i,z} + k_{t,z}} \quad (2.52)$$

$$t_p = \frac{2k_{i,z}}{n^2 k_{i,z} + k_{t,z}} \quad (2.53)$$

Since the index of refraction for x-rays is very close to unity there will be no difference and therefore only s-polarization will be considered.

The intensity R of the reflected x-ray wave under small angle with absorption is given by

$$R(\alpha) = rr^* = \left| \frac{\alpha_i - \sqrt{\alpha_i^2 - \alpha_c^2 - 2i\beta}}{\alpha_i + \sqrt{\alpha_i^2 - \alpha_c^2 - 2i\beta}} \right|^2 \quad (2.54)$$

Using the wave-vector transfer \mathbf{q} , the reflected intensity finally becomes

$$R(\mathbf{q}) = \frac{\left| q_z - \sqrt{q_z^2 - q_c^2 - \frac{32i\pi^2\beta}{\lambda^2}} \right|}{\left| q_z + \sqrt{q_z^2 - q_c^2 - \frac{32i\pi^2\beta}{\lambda^2}} \right|} \rightarrow \frac{q_c^4}{16q_z^4} \text{ for } q_z \gg q_c \quad (2.55)$$

with

$$\begin{aligned} q_z &= 2k \sin(\alpha_i) \\ q_c &= 2k \sin(\alpha_c) \end{aligned} \quad (2.56)$$

The Fresnel reflectivity $R(\mathbf{q})$ has a plateau of total external reflection when $q_z < q_c$, a very steep decrease at $q_z = q_c$ and a $1/q_z^4$ power law when $q_z > 3q_c$. The reflectivity can be also defined by the ratio of the reflected intensity $I(\mathbf{q})$ at a certain wave vector transfer and the intensity of the incident beam:

$$R(\mathbf{q}) = \frac{I(\mathbf{q})}{I_0} \quad (2.57)$$

and

$$I(\mathbf{q}) = I_0 \int \frac{d\sigma}{d\Omega}(\mathbf{q}) d\Omega \quad (2.58)$$

with the differential scattering cross-section $d\sigma/d\Omega$ eq. (2.5) (Als-Nielsen & McMorrow 2001)

$$\left(\frac{d\sigma}{d\Omega} \right)_{\text{Fresnel}} = \left(\frac{r_0 \rho}{q_z} \right)^2 \left(\frac{A_0}{\sin \alpha_i} \right) \int e^{i(q_x x + q_y y)} dx dy. \quad (2.59)$$

Here, ρ is the electron density and A_0 is the illuminated surface area.

The transmitted intensity T is given by

$$T(\alpha) = tt^* = \left| \frac{2\alpha_i}{\alpha_i + \sqrt{\alpha_i^2 - \alpha_c^2 - 2i\beta}} \right|^2 \text{ or} \quad (2.60)$$

$$T(\mathbf{q}) = \left| \frac{2q_z}{q_z + \sqrt{q_z^2 - q_c^2 - \frac{32i\pi^2\beta}{\lambda^2}}} \right| \quad (2.61)$$

and has a maximum at $q_z = q_c$. The maximum in transmission is known as Yoneda wing and will be further explained in chapter 2.6.1.

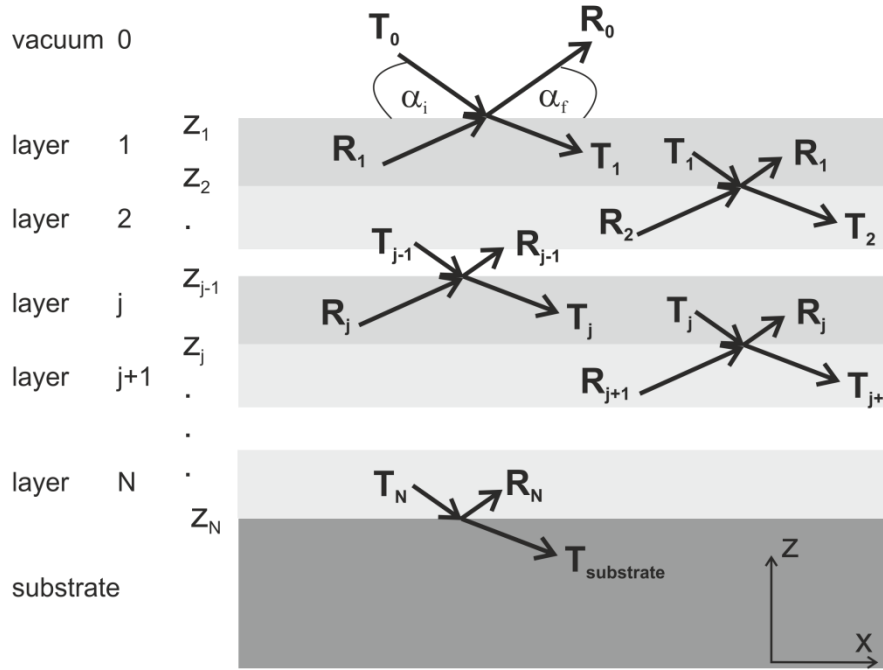


Figure 2.4: Sketch of a stack consisting of $N+1$ layers with N interfaces. The incident wave amplitude $T_0 = 1$ and the reflected substrate wave $R_{\text{substrate}} = 0$. (Tolan 1999)

2.3.3 XRR – The Parratt Formalism

For technical applications the case of multiple scattering on several interfaces is of large interest, especially at thin film investigations of multilayer coatings. Parratt developed a recursive formalism to describe multiple scattering of N layers deposited on an semi-infinite thick substrate (Parratt 1954) (Figure 2.4). In this formalism, each layer j has its thickness $d_j = z_{j-1} - z_j$ and its own refractive index n_j . $\mathbf{k}_{i,j}$ and T_j are the wave vector and the amplitude of transmittance and $\mathbf{k}_{r,j}$ and R_j the corresponding parameters for the reflected wave. The transmitted impinging wave amplitude T_0 at the top layer is set to unity and the reflected wave inside the substrate $R_{\text{substrate}}$ is set to zero. The ratio X_j of the amplitude of the reflected wave and the transmitted wave at the lower interface of layer j is given by the recursive formula

$$X_j = \frac{R_j}{T_j} = e^{-2ik_{z,j}z_j} \frac{r_{j,j+1} + X_{j+1}e^{2ik_{z,j+1}z_j}}{1 + r_{j,j+1} + X_{j+1}e^{2ik_{z,j+1}z_j}} \quad (2.62)$$

with

$$r_{j,j+1} = \frac{k_{z,j} - k_{z,j+1}}{k_{z,j} + k_{z,j+1}}, \quad (2.63)$$

which is the Fresnel coefficient of the interface while $k_{z,j} = k\sqrt{n_j^2 - \cos^2(\alpha_i)}$ denotes the z-component of \mathbf{k} in layer j. The specular reflected intensity R ($\alpha_i = \alpha_f$) is obtained from eq. (2.62) by a N-steps iteration analysis and estimated by

$$R = |X_0|^2 = |R_0|^2 \quad (2.64)$$

With the estimated amplitude R_0 and using the fact of $T_0 = 1$ one can calculate the following amplitudes R_j and T_j by

$$\begin{aligned} R_{j+1} &= \frac{1}{t_{j+1,j}} \left\{ T_j r_{j+1,j} e^{-i(k_{z,j+1} + k_{z,j})z_j} + R_j e^{-i(k_{z,j+1} - k_{z,j})z_j} \right\} \\ T_{j+1} &= \frac{1}{t_{j+1,j}} \left\{ T_j e^{i(k_{z,j+1} - k_{z,j})z_j} + R_j r_{j+1,j} e^{i(k_{z,j+1} + k_{z,j})z_j} \right\} \end{aligned} \quad (2.65)$$

with the Fresnel coefficient $t_{j+1,j} = 1 - r_{j+1,j}$. For larger incident angle the reflectivity decreases according to eq.(2.55). However, there appear superimposing Kiessig fringes (Kiessig 1931), which comprise the thickness values of the layers estimated by

$$d = \frac{2\pi}{\Delta q_z} \quad (2.66)$$

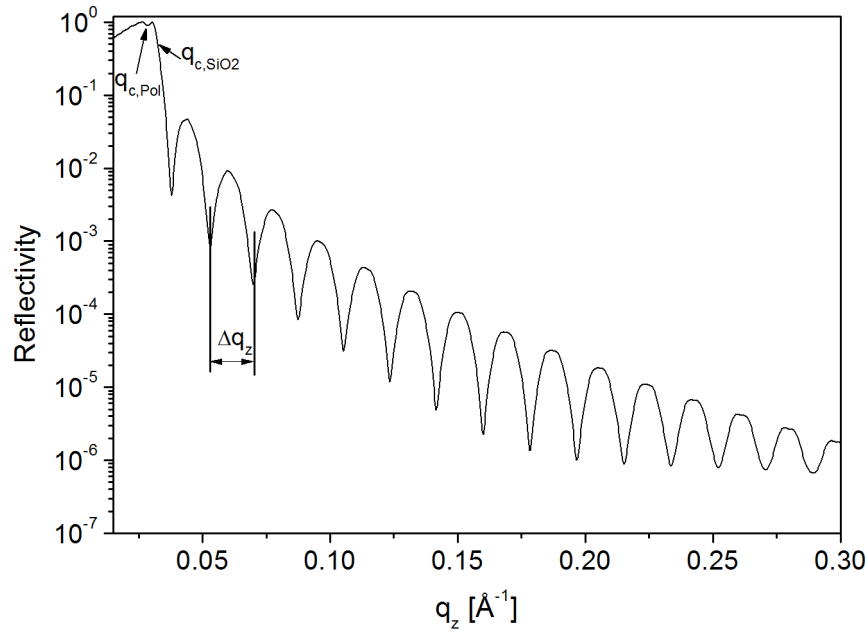


Figure 2.5: Calculated reflectivity of a polymer layer thickness of 34 nm on thermally oxidized silicon oxide with silicon as substrate. One can clearly distinguish the critical scattering vector of the polymer $q_{c,Pol}$ and the critical scattering vector of the silicon oxide q_{c,SiO_2} .

Figure 2.5 illustrates a calculated reflectivity of a multilayer stack containing a polymer layer with a simulated thickness of 34 nm on top of a 150 nm thick silicon oxide. One can clearly distinguish between the critical wave vector transfer of the polymer film ($q_{c,pol}=0.024 \text{ \AA}^{-1}$) and the critical wave vector transfer of the silicon oxide ($q_{c,SiO_2}=0.029 \text{ \AA}^{-1}$).

In the latter approach, the interface roughness and the surface roughness have been not considered, which will be included in the following step. First of all one has to mathematically describe the roughness of an interface. A rough surface or interface always contains density fluctuations in z-direction. Hence the index of refraction, which contains the electron density within a layer, has to be modified from a sharp, stepped change between one layer j to the next layer $j+1$ to a more mathematical specification of the interface. In specular direction, only the z-component of the wave vector transfer \mathbf{q} is of interest. Therefore, the structure laterally averaged over (x, y) is probed and the one dimensional index of refraction is written as

$$n_j(z) = \iint n_j(x, y, z) dy dx \quad (2.67)$$

The abrupt interface at z_j will be replaced by an ensemble of interfaces (Figure 2.6), weighted by the probability function $P_j(z)$ with a mean value of

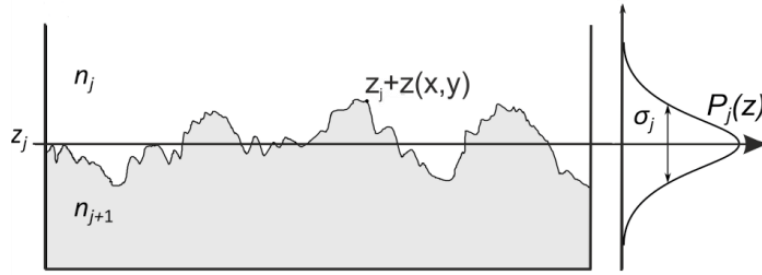


Figure 2.6: Schema of surface (interface) roughness, which is mathematically described by the probability function $P_j(z)$.

$$\mu_j = \int z P_j(z) dz \quad (2.68)$$

and the root-mean-square roughness is now defined as

$$\sigma_j^2 = \int (z - \mu_j)^2 P_j(z) dz. \quad (2.69)$$

According to (Tolan 1999) we assume a continuous index of refraction written as

$$n_j(z) = \frac{n_j + n_{j+1}}{2} - \frac{n_j - n_{j+1}}{2} \operatorname{erf}\left(\frac{z - z_j}{\sqrt{2}\sigma_j}\right) \quad (2.70)$$

with the error function denoted by

$$\operatorname{erf}(z) = \frac{2}{\sqrt{\pi}} \int_0^z e^{-t^2} dt. \quad (2.71)$$

Assuming a Gaussian probability density ($\mu_j = 0$)

$$P_j(z) = \frac{1}{\sqrt{2\pi}\sigma_j} e^{-\frac{z^2}{2\sigma_j^2}} \quad (2.72)$$

results finally in modified Fresnel coefficients

$$\begin{aligned} \tilde{r}_{j,j+1} &= r_{j,j+1} e^{-2k_{z,j}k_{z,j+1}\sigma_j^2} \\ \tilde{t}_{j,j+1} &= t_{j,j+1} e^{\frac{1}{2}(k_{z,j}-k_{z,j+1})^2\sigma_j^2} \end{aligned} \quad (2.73)$$

The factor $\exp(-2k_{z,j}k_{z,j+1}\sigma_j^2)$ in $\tilde{r}_{j,j+1}$ is called Croce-Névoť factor (Croce & Névoť 1976).

These coefficients directly describe a single surface and can be used in Parratt's recursive formalism, with one important consideration; the roughness σ_j of each layer must be significant smaller than its layer thickness d_j . Summing up, one can estimate the layer

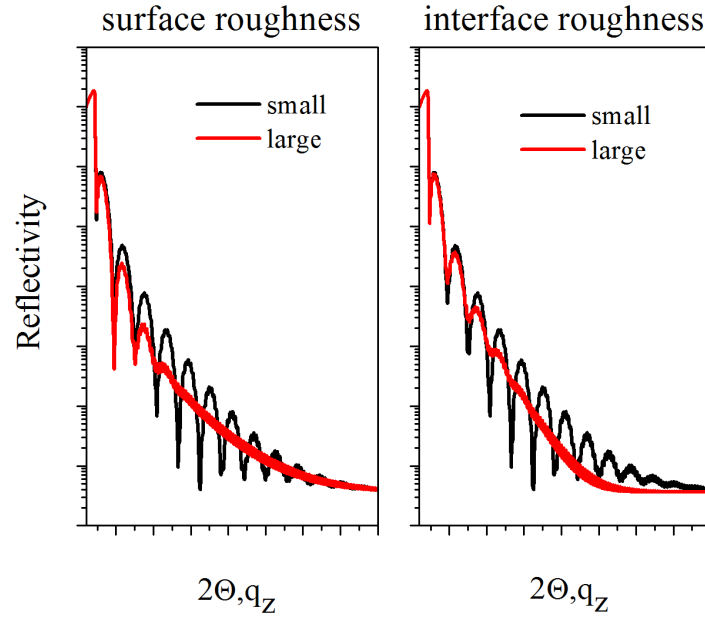


Figure 2.7: Schema of x-ray reflectivity graphs with respect to the diffraction angle or out of plane component of the scattering vector q . The surface roughness and the interface roughness differ by the slope of the graph as well as by the deepness of the Kiessig fringes.

thickness d , the interface as well as the surface roughness σ and the electron density of the used materials ρ_e in a multilayer arrangement by using the Parratt formalism. Figure 2.7 illustrates a simulated reflectivity pattern with different interface roughness and surface roughness. One can clearly distinguish between small and large roughness by the steepness of the slope and the deepness of the Kiessig fringes in the reflectivity graphs.

Multilayer systems where the conditions of $\sigma_j \ll d_j$ are not fulfilled uses the so-called **effective-density model** according to (Tolan 1999). This approach needs a reasonable “initial guess” of the dispersion evolution $\delta(z)$ (eq. (2.39)) in the multilayer stack. In this model, the profile of the interfaces are determined by the function $Y_j(z)$, which has the following limits $Y_j(z) \rightarrow \pm 1$ for $z \rightarrow \pm\infty$, e.g. $Y_j(z) = \tanh[z\pi/(2\sqrt{3}\sigma_j)]$ or $Y_j(z) = \text{erf}[z/(\sqrt{2}\sigma_j)]$. In addition one has to introduce a second quantity, the fraction $W_j(z)$ of the material j at the position z written as

$$W_j(z) = \begin{cases} \frac{1}{2}[1 + Y_j(z - z_j)] & \text{for } z \leq \zeta_j \\ \frac{1}{2}[1 - Y_j(z - z_{j-1})] & \text{for } z > \zeta_j \end{cases} \quad (2.74)$$

where ζ_j denotes the depth at which the upper and lower profiles of the interface j are connected continuously and is defined as

$$\zeta_j = \frac{\sigma_j z_{j-1} + \sigma_{j-1} z_j}{\sigma_j + \sigma_{j-1}}. \quad (2.75)$$

Within the effective density model, q becomes $-\infty$ at the substrate and $q = +\infty$ at the surface. The final dispersion profile $\delta(z)$ finally is estimated by

$$\delta(z) = \frac{\left(\sum_{j=1}^{N+1} \delta_j W_j(z) \right)}{\sum_{j=1}^{N+1} W_j(z)} \quad (2.76)$$

In this model the parameters δ_j , σ_j and $d_j = z_{j-1} - z_j$ are those which have to be refined. For small roughness $\sigma_j \ll d_j$ each of the N considered layers are treated as independent and the Fresnel coefficients eq. (2.73) are used. Here, the interface roughness σ_j denotes the width between material j and j and material $j+1$. For rough interfaces the parameters $\delta(z)$ is always less than the nominal value δ_j and is then called *effective density at depth z* . The “first guess” of these parameters stems from the reflectivity simulations using the Parratt formalism, which is explained above. One example of the effective density model applied to an inorganic/organic multilayer stack is given in chapter 3.

2.3.4 XRR – The Matrix Method

A similar thought to the concept above is the matrix method, first invented by F. Abelès (Abelès 1950). Here, the main principle of the matrix method will be described by following the textbook of Gibaud and Vignaud (Daillant & Gibaud 2009). In general, the wave vector $\mathbf{k}_{i,j}$ at an specific layer j is described by a propagating wave in upwards and downwards direction and the magnitude of the electrical field is denoted by

$$U(\pm \mathbf{k}_{i,j}, z) = E_j^\pm e^{\pm i \mathbf{k}_{i,j} z}. \quad (2.77)$$

Here, E_j is the amplitude of the travelling wave in layer j .

Two boundary conditions are used:

- 1) The continuity of the tangential component of the electrical field together with the conservation of $k_{x,j}$ at the depth z_{j+1} of the interface, mathematically spoken;

$$U(k_{z,j}, z_{j+1}) + U(-k_{z,j}, z_{j+1}) = U(k_{z,j+1}, z_{j+1}) + U(-k_{z,j+1}, z_{j+1}). \quad (2.78)$$

- 2) The first derivate of the electrical field has to be conserved;

$$k_{z,j}[U(k_{z,j}, z_{j+1}) - U(-k_{z,j}, z_{j+1})] = k_{z,j+1}[U(k_{z,j+1}, z_{j+1}) - U(-k_{z,j+1}, z_{j+1})]. \quad (2.79)$$

These two general equations are now written in matrix form and are valid for each interface $j, j+1$

$$\begin{bmatrix} U(k_{z,j}, z_{j+1}) \\ U(-k_{z,j}, z_{j+1}) \end{bmatrix} = \begin{bmatrix} p_{j,j+1} & m_{j,j+1} \\ m_{j,j+1} & p_{j,j+1} \end{bmatrix} \begin{bmatrix} U(k_{z,j+1}, z_{j+1}) \\ U(-k_{z,j+1}, z_{j+1}) \end{bmatrix} \quad (2.80)$$

with

$$\begin{aligned} p_{j,j+1} &= \frac{k_{z,j} + k_{z,j+1}}{2k_{z,j}} \\ m_{j,j+1} &= \frac{k_{z,j} - k_{z,j+1}}{2k_{z,j}} \end{aligned} \quad (2.81)$$

The so-called refraction matrix ξ in equation (2.80) transforms the magnitude of the electrical field from medium j to medium $j+1$. This matrix not unimodular and has a determinant of $k_{z,j+1}/k_{z,j}$. The electrical field changes from layer to layer with the layer thickness d by $z_{j+1} = z_j + d$. The corresponding matrix v

$$v = \begin{bmatrix} e^{-ik_{z,j}d} & 0 \\ 0 & e^{ik_{z,j}d} \end{bmatrix} \quad (2.82)$$

is called translation matrix.

Each multilayer system of N layers can now be simulated with the matrix method by estimating the magnitude of the electrical field. Starting from the substrate z_s upwards to the top layer $z_1 = 0$, the matrix is given by

$$\begin{bmatrix} U(k_{z,0}, z_1) \\ U(-k_{z,0}, z_1) \end{bmatrix} = \xi_{0,1} v_1 \xi_{1,2} \dots \xi_{N,s} \begin{bmatrix} U(k_{z,s}, z_s) \\ U(-k_{z,s}, z_s) \end{bmatrix} \quad (2.83)$$

All the matrices are 2×2 matrixes and the product of these matrices is called transfer Matrix M

$$\mathbf{M} = \begin{bmatrix} M_{11} & M_{12} \\ M_{21} & M_{22} \end{bmatrix}. \quad (2.84)$$

Due to the fact that $U(k_{z,s}, z_s) = 0$, the coefficient of reflection and transmission is denoted by

$$\begin{aligned} r &= \frac{M_{12}}{M_{22}} \\ t &= \frac{1}{M_{22}} \end{aligned} \quad (2.85)$$

For x-rays, each matrix element of the transfer matrix can be expressed by the electron density of the layer j and the wavelength of the radiation by

$$k_{z,j} = -k_0 \sqrt{\alpha_i^2 - 2\delta_j - 2i\beta_j} \quad (2.86)$$

Finally one has to introduce the roughness parameter to the matrix method, which is done in a similar way like the previous chapter. The Fresnel coefficient of the flat interface is just reduced by the Croce-Névoť factor (Croce & Névoť 1976) and the coefficient of reflection is written as

$$\frac{r_{j,j+1}^{\text{rough}}}{r_{j,j+1}^{\text{flat}}} = e^{-2k_{z,j+1}k_{z,j}\sigma_{j+1}^2}. \quad (2.87)$$

2.4 XRR on Rough Surfaces

In the chapter 2.3.3 the root-mean-square (r.m.s) roughness was introduced to the Parratt formalism and the Matrix method by the Croce-Névoit factor. Here the basic statistical approach will be discussed containing additional morphology parameters following the book of Zhao, Wang and Lu (Zhao, Wang, & Lu 2001a).

In general a random rough surface is mathematically described by the function $h = h(\mathbf{r})$, while h is the surface height of a rough surface with respect of a smooth reference surface and \mathbf{r} is the position vector on the surface. A random rough surface can be characterized by its height distribution function $p(h)$, which defines the probability of a surface height between h and $h+dh$ at any point on the surface with $p(h)dh$. The distribution $p(h)$ is a non-negative function and is normalized in a way that

$$\int_{-\infty}^{\infty} p(h)dh = 1. \quad (2.88)$$

For the statistically description of the distribution of a random variable h one can simply estimate the moment m by

$$m_n = \int_{-\infty}^{\infty} (h - \bar{h})^n p(h)dh \quad (2.89)$$

The first order moment is the average surface height \bar{h} and is set to zero. The second order moment of the variable h is frequently used to physically describe an r.m.s. surface roughness σ and is defined by

$$m_2 = \sigma^2 = \int_{-\infty}^{\infty} h^2 p(h)dh \quad (2.90)$$

The 3rd and 4th order moment describes the skewness and kurtosis of a randomly rough surface, respectively. Note that the latter parameters are dimensionless, whilst the r.m.s. roughness is in units of length. The discussed height distribution function only describes the statistical properties of the random variable h and cannot reflect the connection between random variables at different positions. This means that different rough surfaces can have the same height distribution $p(h)$ and also the same r.m.s. roughness but due to different height variation at different length scales, they can look completely different. Figure 2.8 (left) shows an example of a surface profile with the same distribution function $p(h)$. Hence, one needs to

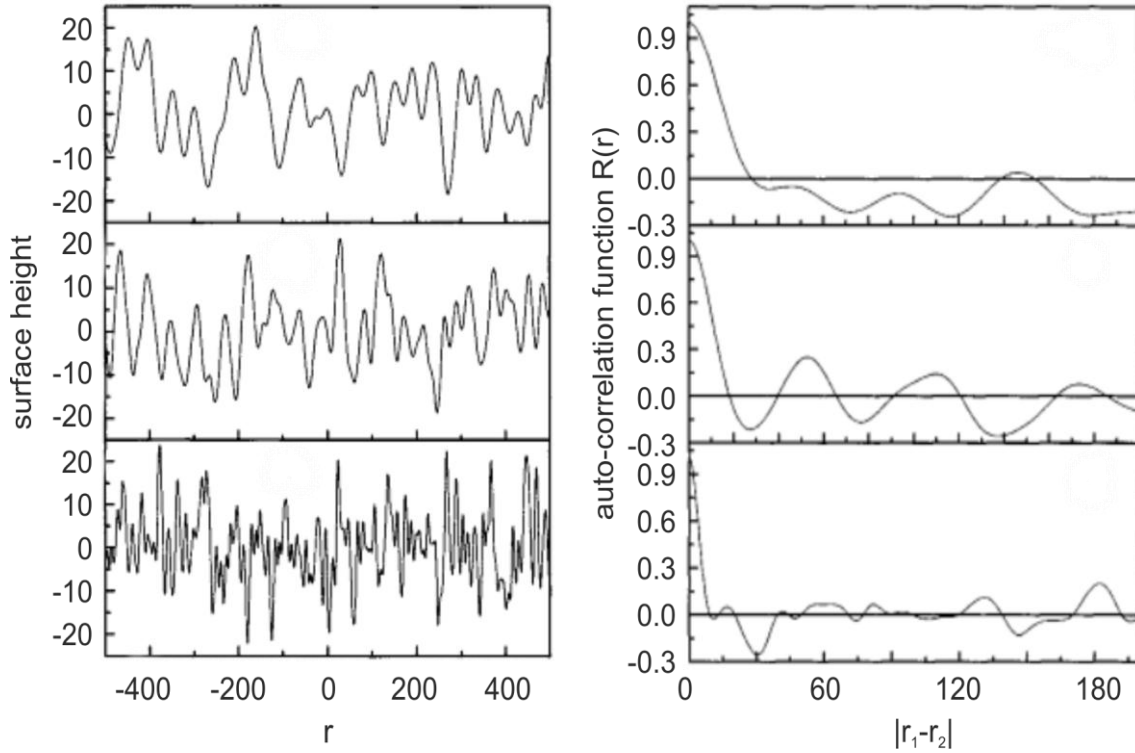


Figure 2.8: Surface profiles with the same roughness value but different correlation lengths ξ (left) and the corresponding auto correlation function (right) (Zhao, Wang, & Lu 2001)

know the connection of a random field $h(\mathbf{r})$ at two different positions \mathbf{r}_1 and \mathbf{r}_2 to give physically unambiguous information of a surface. Thus, the joint distribution probability function $p_j(h_1, h_2; \mathbf{r}_1, \mathbf{r}_2)$ of $[h(\mathbf{r}_1), h(\mathbf{r}_2)]$, which has to fulfil eq. (2.88), is related to the height distribution and the correlation of heights between two separated points. The most important statistical characteristic of a joint distribution is the auto-correlation function $R(\mathbf{r}_1, \mathbf{r}_2)$, which is defined by

$$R(\mathbf{r}_1, \mathbf{r}_2) = \frac{1}{\sigma^2} \int_{-\infty}^{\infty} \int_{-\infty}^{\infty} h_1 h_2 p_j(h_1, h_2; \mathbf{r}_1, \mathbf{r}_2) dh_1 dh_2 \quad (2.91)$$

For a homogenous and isotropic rough surface, $R(\mathbf{r}_1, \mathbf{r}_2)$ depends only on the distance between two positions \mathbf{r}_1 and \mathbf{r}_2 via

$$R(\mathbf{r}_1, \mathbf{r}_2) = R(|\mathbf{r}_1 - \mathbf{r}_2|). \quad (2.92)$$

The lateral correlation length ξ of an auto-correlation function is usually defined as the value of the distance between \mathbf{r}_1 and \mathbf{r}_2 at which the auto-correlation function drops to $1/e$ of its initial value at $|\mathbf{r}_1 - \mathbf{r}_2| = 0$,

$$R(\xi) = \frac{1}{e} \quad (2.93)$$

The correlation length ξ defines a representative lateral dimension of a rough surface, which means that if the distance between two surface points is within ξ , the heights at these two points are correlated. Figure 2.8 (right) illustrates an example of three different auto-correlation lengths, where the top image has the largest and the bottom image the smallest correlation length. Therefore the bottom surface looks rougher. In literature there exist several auto-correlation functions $R(|\mathbf{r}_1 - \mathbf{r}_2|)$ like

$$\begin{aligned} \text{Gaussian} & \quad e^{-\frac{|\mathbf{r}_1 - \mathbf{r}_2|^2}{\xi^2}} \\ \text{Exponential} & \quad e^{-\frac{|\mathbf{r}_1 - \mathbf{r}_2|}{\xi}} \\ \text{Lorentzian} & \quad \frac{\xi^4}{\left(\xi^2 + |\mathbf{r}_1 - \mathbf{r}_2|^2\right)^2} \cdot \\ \text{Power Law} & \quad \left(1 + \frac{|\mathbf{r}_1 - \mathbf{r}_2|^2}{\xi^2}\right)^{-\frac{3}{2}} \end{aligned} \quad (2.94)$$

The surface roughness σ and the lateral correlation length ξ alone are not enough to give a full description of the surface roughness. The missing parameter is called the Hurst parameter α ($0 < \alpha < 1$), which describes the height fluctuation at the surface; small α values produce very rough surfaces while high values of α defines more regular surfaces. The latter parameter is associated to fractal surfaces with dimensions of $D = 3 - \alpha$ as established by Mandelbrodt (Mandelbrot 1991). Figure 2.9 (left) illustrates three different surfaces with same r.m.s surface roughness and same lateral correlation length, but different Hurst parameter α . The physical understanding of α can be expressed by the jaggedness of a surface. Note that the surface roughness σ , the lateral correlation length ξ and the Hurst parameter α are independent of each other and completely describe a self-affine surface.

Very frequently another two statistical parameters are used to describe a surface, the height-height correlation function $C(\mathbf{R})$ and the mean quadratic height difference function $g(\mathbf{R})$ (Tolan 1999).

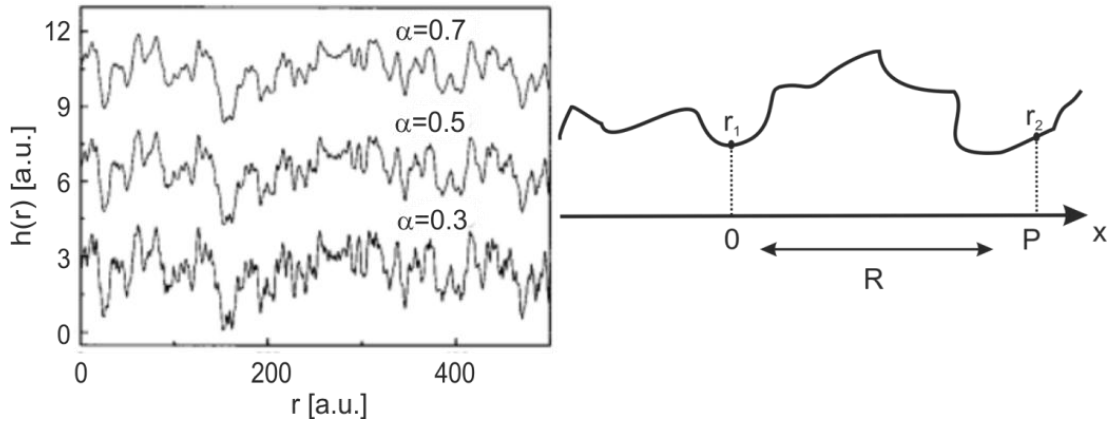


Figure 2.9: Rough surface profile with different Hurst parameters (left). The surfaces have the same surface roughness and the same lateral correlation length. The right image illustrates a sketch of a surface contour $z(\mathbf{R})$.

$C(\mathbf{R})$ is defined by

$$C(\mathbf{R}) = \frac{1}{A} \int_A z(\mathbf{r}_{\parallel}) z(\mathbf{r}_{\parallel} + \mathbf{R}) d\mathbf{r}_{\parallel} = \langle z(\mathbf{r}_{\parallel}) z(\mathbf{r}_{\parallel} + \mathbf{R}) \rangle_{\mathbf{r}_{\parallel}} \quad (2.95)$$

where $\mathbf{R} = (X, Y)$ is the lateral vector see (Figure 2.9 (right)) and A is a large area. $z(\mathbf{r}_{\parallel})$ is a contour function, which means that for each lateral point $\mathbf{r}_{\parallel} = (x, y)$, the value of $z(\mathbf{r}_{\parallel})$ gives the height of the surface with respect to the mean interface location. Using eq.(2.95), the r.m.s. roughness is written as

$$\sigma^2 = C(\mathbf{0}) = \langle z^2(\mathbf{r}_{\parallel}) \rangle_{\mathbf{r}_{\parallel}} \quad (2.96)$$

Many isotropic solid surfaces are described simply by the Gaussian correlation function (Sinha *et al.* 1988), written as

$$C(\mathbf{R}) = \sigma^2 e^{-\left(\frac{R}{\xi}\right)^{2\alpha}} \quad (2.97)$$

The second function $g(\mathbf{R})$ is directly correlated to σ and $C(\mathbf{R})$ and is defined by

$$g(\mathbf{R}) = \langle [z(\mathbf{r}_{\parallel}) - z(\mathbf{r}_{\parallel} + \mathbf{R})]^2 \rangle_{\mathbf{r}_{\parallel}} = 2\sigma^2 - 2C(\mathbf{R}) \quad (2.98)$$

After the statistical treatment of a rough surface we will now introduce height fluctuations at interfaces into the x-ray reflectivity formulism. Here we will use the approach that scattering is assumed to be weak so that multiple reflections may be neglected and one can modify the Fresnel differential cross section (eq.(2.59)) and include an additional roughness factor. One consequence of the existence of a rough interface is that the reflectivity is no longer necessarily strictly specular, it contains a diffuse component.

Considering the statistical treatment to a rough surface, one can modify the Fresnel differential cross section by the Baker-Hausdorff theorem (Als-Nielsen & McMorrow 2001) written as

$$\left(\frac{d\sigma}{d\Omega}\right) = \left(\frac{r_0\rho}{q_z}\right)^2 \left(\frac{A_0}{\sin\alpha_i}\right) \int e^{-q_z^2 \frac{g(\mathbf{R})}{2}} e^{i(q_x x + q_y y)} dx dy \quad (2.99)$$

Here $A_0 = L_x L_y$, where L_x and L_y are the dimensions of the surface in x-direction and y-direction. In literature, this is often called *Cut-Off*.

For *surfaces without correlation*, where the height of \mathbf{r}_1 is independent of the height of \mathbf{r}_2 , no matter how close \mathbf{r}_1 and \mathbf{r}_2 are, the latter equation is simplified by

$$\left(\frac{d\sigma}{d\Omega}\right) = \left(\frac{d\sigma}{d\Omega}\right)_{\text{Fresnel}} e^{-q_z^2 \sigma^2} \quad (2.100)$$

where $\sigma = \text{sqrt}(\langle z^2(\mathbf{r}_{\parallel}) \rangle)$ is the r.m.s roughness. The latter equation directly expresses that a rough surface reduces the reflectivity similar to the Croce-Névo factor introduced in chapter 2.3.3. Due to the uncorrelated height fluctuations, the scattering is confined to the specular direction like for the perfectly sharp interface. This points to the fact that for different models, the reflectivity cannot uniquely reveal the true nature of an interface. Hence, a complementary roughness determination method will support XRR roughness parameters significantly.

For *correlated surfaces*, the height fluctuation is isotropic in the plane of the surface, which means that $g(\mathbf{R})$ depends only on $\mathbf{R} = |\mathbf{R}| = \text{sqrt}(x^2 + y^2)$ (Als-Nielsen & McMorrow 2001). One can distinguish between two cases, depending on the behaviour of $g(\mathbf{R})$ in the limit of $\mathbf{R} \rightarrow \infty$. The first case is

$$g(\mathbf{R}) = \left\langle \left[z(\mathbf{r}_{\parallel}) - z(\mathbf{r}_{\parallel} + \mathbf{R}) \right]^2 \right\rangle_{r_{\parallel}} = 2lr^{2\alpha} \quad (2.101)$$

In this case the height fluctuation develops without limit as $\mathbf{R} \rightarrow \infty$ and the roughness is expressed by fractal surfaces with the Hurst parameter α . Here, the differential cross section can be simplified by setting $y = 0$, which means a broad resolution in q_y direction. The problem is then reduced to a one-dimensional integral where $g(\mathbf{R})$ depends only on $|x|$,

$$\left(\frac{d\sigma}{d\Omega}\right) = \left(\frac{r_0\rho}{q_z}\right)^2 \left(\frac{A_0}{\sin\alpha_i}\right) \int_0^\infty e^{-2q_z^2|x|^{2\alpha}/2} \cos(q_x x) dx. \quad (2.102)$$

The second case considers a finite height fluctuation when $\mathbf{r} \rightarrow \infty$ (see eq. (2.98)). If one consider now Gaussian height-height correlation function (eq. 2.97) it can be seen that for $R \ll \xi$, $g(\mathbf{R}) \approx R^{2\alpha}$. and that for $R \rightarrow \infty$, $g(\mathbf{R}) \rightarrow 2\sigma^2$ as required. The differential cross-section can then be described as

$$\left(\frac{d\sigma}{d\Omega}\right) = \left(\frac{r_0\rho}{q_z}\right)^2 \left(\frac{A_0}{\sin\alpha_i}\right) e^{-q_z^2\sigma^2} \int e^{q_z^2 C(\mathbf{R})} e^{i(q_x x + q_y y)} dx dy \quad (2.103)$$

By the following re-writing it is possible to separate the differential cross-section into a specular and a diffuse term by

$$\left(\frac{d\sigma}{d\Omega}\right) = \left(\frac{r_0\rho}{q_z}\right)^2 \left(\frac{A_0}{\sin\alpha_i}\right) e^{-q_z^2\sigma^2} \int \left[e^{q_z^2 C(\mathbf{R})} + 1 - 1 \right] e^{i(q_x x + q_y y)} dx dy \quad (2.104)$$

where the specular form of the uncorrelated surface is involved. The total cross-section may be rewritten in the form

$$\left(\frac{d\sigma}{d\Omega}\right) = \left(\frac{d\sigma}{d\Omega}\right)_{\text{Fresnel}} e^{-q_z^2\sigma^2} + \left(\frac{d\sigma}{d\Omega}\right)_{\text{diffuse}} \quad (2.105)$$

With the diffuse component is given by

$$\left(\frac{d\sigma}{d\Omega}\right)_{\text{diffuse}} = \left(\frac{r_0\rho}{q_z}\right)^2 \left(\frac{A_0}{\sin\alpha_i}\right) e^{-q_z^2\sigma^2} \int \left[e^{q_z^2 C(\mathbf{R})} - 1 \right] e^{i(q_x x + q_y y)} dx dy \quad (2.106)$$

A real surface always contains a natural rough surface and therefore the diffuse term of the scattering cross section is a non-negligible factor in the experiment. One possibility to investigate the roughness of a surface by its diffuse scattering intensity is a rockingcurve, which will be explained in chapter 2.5.1.

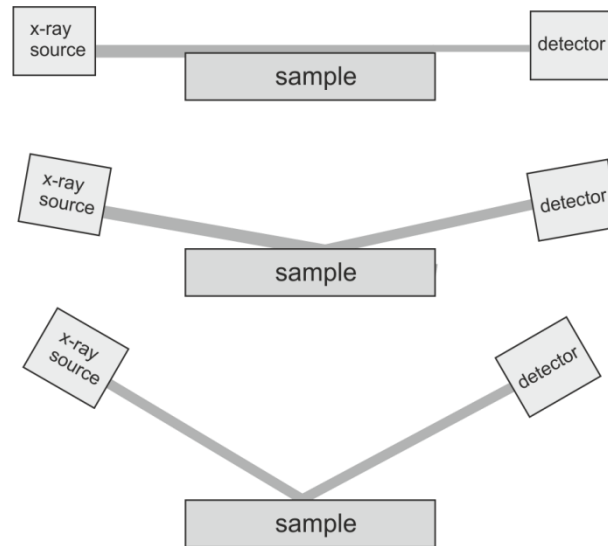


Figure 2.10: Sketch of illumination area variation during an x-ray reflectivity experiment

2.5 XRR Laboratory Equipment

In the latter chapter, the theoretical approach of x-ray reflectivity was introduced, which allows us to explain the general phenomena of XRR analysis. However, there are several technical requirements to an x-ray diffractometer.

From the experimental point of view the mechanical requirements on the goniometer was one challenging aspect in the past due to the fact that the glancing angle have to be adjusted very precisely. Nowadays the mechanics of the goniometers of a modern diffraction machine reached an accuracy of one-thousands of degree. Another important demand for an XRR experiment is a well-collimated radiation with low angular divergence. This is realised by proper slit optics or in these days frequently by multilayer mirrors.

Due to the fact that XRR experiments starts below the critical angle of external diffraction, the beam size is an important parameter. Assuming a rectangular beam with dimensions $w_1 \cdot w_2$ and an incidence angle of α_i , the so called footprint F of the beam on the surface of the sample is

$$F = \frac{w_1}{\sin \alpha_i} w_2 \quad (2.107)$$

Figure 2.10 illustrates the footprint behaviour on the sample. Starting from an incidence angle of zero the sample is adjusted to be half in the beam height. Thus the whole sample

surface is illuminated by the beam. Increasing the angle of incidence and reflectance, the footprint on the sample becomes continuously smaller.

X-ray reflectivity setups demand very small slits on both sides of the sample for optimal resolution. The beam height has to be e.g. smaller than 0.12 mm for silicon ($\alpha_c = 0.22^\circ$, CuK $_{\alpha}$) investigations (Gibaud, Vignaud, & Sinha 1993). Therefore the primary divergence slit has to be as small as possible. In addition the secondary slit has to match the aperture of the primary slit to reach the required angular resolution.

Another important parameter for an XRR experiment is the resolution function correction, because the resolution function differs from an exact δ function. Here we consider an elastic scattering process in the x,z – system (flat lying sample), where \mathbf{q} has two components

$$\begin{aligned} q_x &= k_0(\cos(\alpha_i) - \cos(\alpha_f)) \\ q_z &= k_0(\sin(\alpha_i) + \sin(\alpha_f)) \end{aligned} \quad (2.108)$$

with α_i and α_f denoting the angle of the incoming and outgoing beam and $k_0 = 2\pi/\lambda$. q_y is not considered due to the fact that in this direction the size of the slits is large enough to integrate the scattering intensity. The resolution parallel δq_x and perpendicular δq_z to the surface is now written

$$\begin{aligned} \delta q_x &= \frac{\Delta\lambda}{\lambda} q_x + k_0(\alpha_i \Delta\alpha_i + \alpha_f \Delta\alpha_f) \\ \delta q_z &= \frac{\Delta\lambda}{\lambda} q_z + k_0(\Delta\alpha_i + \Delta\alpha_f) \end{aligned} \quad (2.109)$$

For very small angles and specular conditions this is simplified to (M Tolan 1999)

$$\begin{aligned} \delta q_x &= q_z \Delta\alpha \\ \delta q_z &= 2k_0 \Delta\alpha \end{aligned} \quad (2.110)$$

One good approximation to determine the resolution of the diffraction machine is to measure the angular acceptance $\Delta\alpha$ of the direct beam in the small angle regime and to use its FWHM in eq.(2.110). The acceptance of the detector unit $\Delta\alpha_f$ is determined by the goniometer distance, the slit sizes and the optical elements.

X-ray reflectivity scans are $\Theta/2\Theta$ scans (specular scans) with a constant direction of the z -component of the scattering vector \mathbf{q} . During the scan, the incidence angle α_i (or Θ) and the finite angle α_f are kept identical and increased simultaneously and therefore only the variation of the magnitude of \mathbf{q} in z -direction is detected (Figure 2.12, left).

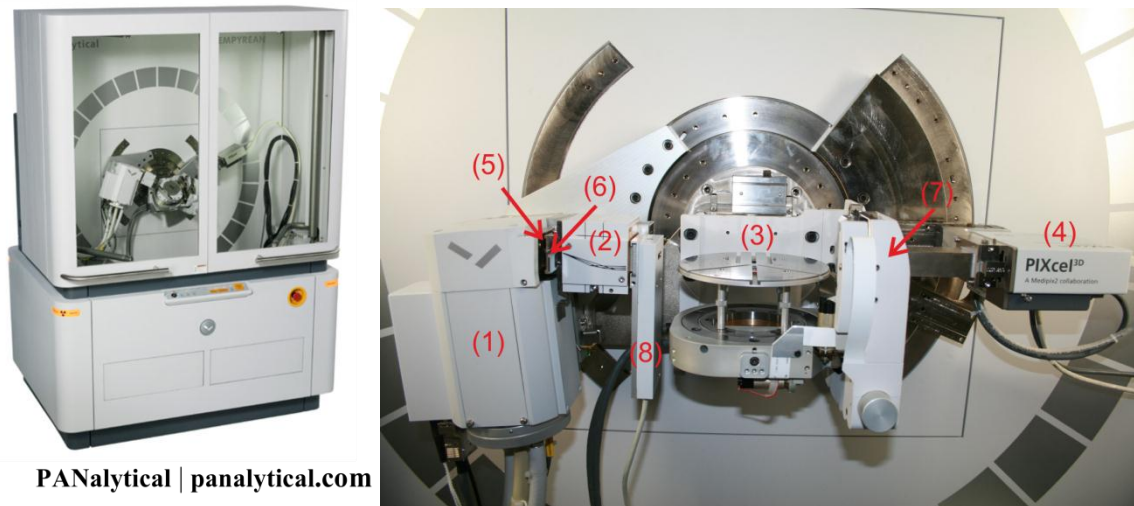


Figure 2.11: The PANalytical Empyrean diffractometer (left) and the different components used for XRR measurements (right).

Table 2.1: Typical setup of an XRR measurement.

x-ray tube	Cu radiation
primary slit	1/32°
beam mask	10 mm
programmable attenuator	Ni (0.125 mm) factor 144
multilayer mirror	monochromatized Cu _{Kα} ; divergence < 0.055°
goniometer distance	240 mm
secondary slit	0.1 mm
detector PIXcel ^{3D}	receiving slit mode (3channels used)

In this work XRR measurements have been performed on the PANalytical Empyrean $\omega/2\theta$ diffractometer (Figure 2.11, left), equipped with a cooper seal tube (1), a multilayer mirror (2), a 3 - axes cradle (3), and the PIXcel^{3D} detector (4). In addition, manually changeable primary slits (5) and secondary slits (6), a beam mask (7) and a programmable beam attenuator (8) are used for the measurements (Figure 2.11, left). Table 2.1 gives the detailed specifications of the diffraction components, which is well-

suiting for the XRR experiments. Here $2/3$ of $\text{Cu}_{K\alpha 1}$ radiation and $1/3$ of the $\text{Cu}_{K\alpha 2}$ radiation passes the multilayer mirror, which results in an x-ray wavelength of 0.154178 nm. The measured data was simulated with the X'Pert Reflectivity 1.3 software (PANalytical) (Dane *et al.* 1998) and will be explained in Appendix A.

The acceptance angle from the line focus of the x-ray tube is 0.8° . Using this setup, the beam height after the mirror is 0.08 mm and the irradiated length L on the sample is calculated by

$$L = 0.1 + \frac{0.08}{\sin(\alpha_i)} \quad (2.111)$$

The purpose of the mirror is to monochromize and collimate the beam after the beam mask. The multilayer mirror has a reflection factor of 65% for the $K_{\alpha 1}$ and $K_{\alpha 2}$ lines. 95% of the K_{β} line is rejected from the mirror.

Considering these diffractometer specifications, one can also give the longitudinal coherence length ξ_L and the transversal coherence length ξ_T (Als-Nielsen & McMorrow 2001). The longitudinal coherence length ξ_L is primarily set by the used tube radiation and is calculated by

$$\xi_L = \frac{\lambda^2}{2\Delta\lambda} \approx 30\text{nm} \quad (2.112)$$

for copper radiation, where $\Delta\lambda$ is calculated by $(\lambda_{K\alpha 2} - \lambda_{K\alpha 1})$. The transversal coherence length ξ_T has to be distinguished by its vertical part and horizontal part. The horizontal transversal coherence length is limited by the beam mask and therefore rather imprecise. However one can estimate the vertical transversal coherence ξ_{Tv} by

$$\xi_{Tv} = \frac{\lambda}{\alpha_i \frac{H}{D}}, \quad (2.113)$$

where D is the mirror-sample distance, H is the height of the beam after the mirror and α_i is the incident angle of the beam (Daillant & Gibaud 2009). Using the typical measurements range starting with $\alpha_i = 0.01^\circ$, the vertical transversal coherence length on the sample will be around 25 μm and at a α_i value of 5° the vertical transversal coherence length decreases to 50 nm.

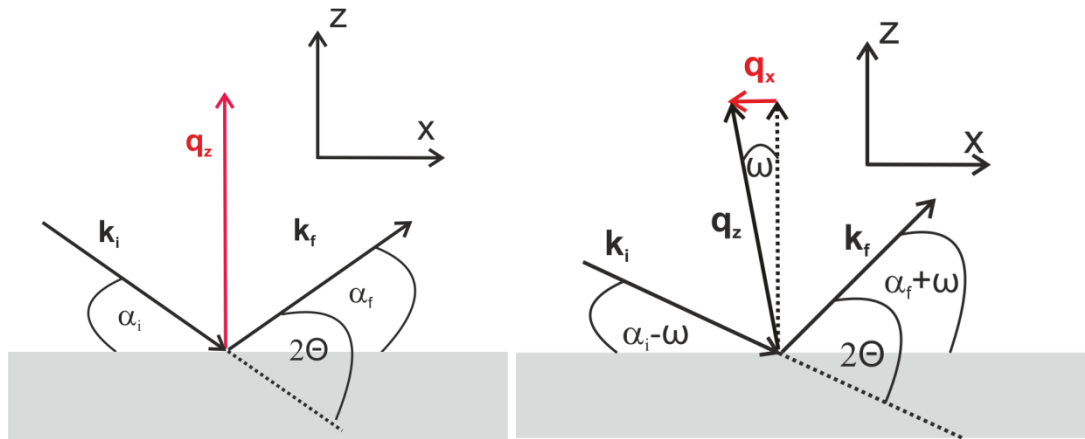


Figure 2.12: Measurement schema of a $\Theta/2\Theta$ scan (right) and a rocking curve scan (left).

2.5.1 Rockingcurves

One possibility to get valuable information from a rockingcurve is to perform it in the XRR regime at low angles. According to the work of V. Holý (Holý *et al.* 1993) one can get further roughness correlations of multilayer samples from rocking scans at very low scattering angles by additionally considering the non-specular (diffuse) contribution of the reflected wave. For incidence angles in the range of the critical angle one has to use the *Distorted Wave Born Approximation* (DWBA) to explain the observing phenomena mathematically (Sinha *et al.* 1988). This dynamical theory suffers the loss of its appliance at angles far away from the critical angle. There, the kinematical theory, the *Born approximation* (BA), becomes great significance. In general the kinematical treatment neglects refraction as well as multiple scattering processes. Using the DWBA several dynamical effects, which are e.g. observable during a rockingcurve scan like the Yoneda wing or dynamical interference fringes can be explained. Here, only the very fundamental approach will be discussed.

First of all, an introduction of the measurement principle will be given and one example of a rockingcurve should illustrate the measured dynamical effects. During a rocking scan the magnitude of q_z is kept constant, while the direction of it is varied. This can be achieved by a constant 2Θ angle between the incident beam and the scattered beam, while the orientation of the beam with respect to the sample surface is varied by ω . The measured

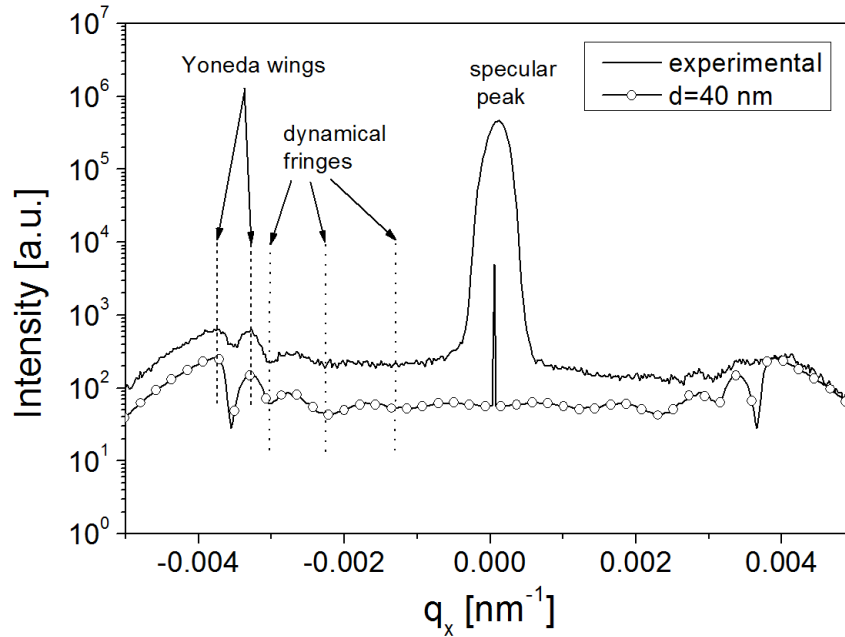


Figure 2.13: Rockingcurve scan (full line) of a 40 nm thick polymer layer at fixed specular position ($2\Theta = 0.97^\circ$) and the simulated curve with the same layer thickness (circle)

quantity during this coplanar scan is the diffuse scattered intensity I_{diffuse} with respect to the x-component of the scattering vector \mathbf{q} (Figure 2.12, right), where q_x is estimated via

$$q_x = \frac{4\pi}{\lambda} \sin\left(\frac{2\Theta}{2}\right) \sin\left(\omega - \frac{2\Theta}{2}\right) = q_z \sin\left(\omega - \frac{2\Theta}{2}\right). \quad (2.114)$$

$$I_{\text{diffuse}} \sim |t_i(\alpha_i)|^2 \frac{d\sigma}{d\Omega} |t_f(\alpha_f)|^2 \quad (2.115)$$

where $d\sigma/d\Omega$ is taken from eq.(2.105) (Tolan 1999).

Figure 2.13 shows a typical rocking curve (full line) of a 40nm thick polymer layer on top of a silicon oxide layer, measured at very low angles ($2\Theta = 0.97^\circ$). The lower two graphs are simulations of the measured data by using the software of Sergey Stepanov (Stepanov 1997) considering the DWBA formalism of Holý and Baumbach (Holý & Baumbach 1994). One can clearly observe two Yoneda wings of the polymer and the silicon oxide, which occur if the incident angle of the beam is equal to critical angle of the material. They are created by an enhancement of the transmitted wave amplitude at the inner sample surface. In addition, so-called dynamical fringes are created by the specular reflection of the diffuse scattered wave and/or by the diffuse scattering of the specular reflected wave of the upper and lower interface. These dynamical fringes are of pure dynamical nature and can be described by the DWBA theory due to multiple-scattering processes in the

individual layers. These fringes are comparable to the Kiessig fringes of a specular XRR measurement and are additionally illustrated in Figure 2.13. There the middle characteristic (circles) is simulated with the specular defined layer thickness of the polymer and the minima of the dynamical fringes coincide with the measurement. An arbitrary thickness (here 691nm) of the polymer layer in the simulation leads to a shift of the dynamical minima and no overlap is observable.

There exists a third dynamical effect, the Bragg-like peaks in periodic multilayer samples, which can be interpreted by the concept of *Umweganregung*. The latter effect can be explained by an excitation of a scattering process by another scattering process. The most pronounced peak in a rockingcurve is the specular peak, which is always observable at $q_x = 0$. Stettner et. al investigated a molecular-beam epitaxial grown $\text{CoSi}_2/\text{Si}/\text{CoSi}_2$ sample with diffuse x-ray scattering analysis and determined the rms roughness, the lateral correlation length as well as the Hurst parameter of the multilayer sample (Stettner *et al.* 1996). Furthermore, J.P. Schlomka used the DWBA theory to investigate epitaxial grown Si/Ge multilayer systems and determined the surface and interface morphology parameters mentioned above (Schlomka *et al.* 1995). These parameters were hardly extractable from the measurements performed on the polymer samples in Figure 2.13. Several simulations of the rms surface roughness, the lateral correlation length and the Hurst parameters could give no satisfying fit result, which is related to the rather less defined layer growth of the spin cast polymer films.

2.6 Grazing Incidence X-ray Diffraction (GIXD)

Grazing incidence x-ray diffraction is a surface - near diffraction analysis technique, which is recently used to investigate the crystallographic structure of thin films down to monolayers. There the incidence angle of the x-ray beam is set to the critical angle of total external reflection α_c (chapter 2.3.2) of the material, which emphasises this technique to be sensitive to surface layers of thin films due to the low penetration depth into the material.

In contrast to the specular x-ray diffraction or co-planar diffraction, which can be nicely described by summing up the scattering contributions of each individual electron by neglecting the refraction phenomena (Born approximation), here the scatterer is now replaced by a material distribution. If a plane wave now impinges into a material, the produced field of all points in the material is calculated via this distribution, which was first established by George H. Vineyard (Vineyard 1982). This establishment is well known as *Distorted Wave Born Approximation* (DWBA). The resulting field is called *distorted wave*, which is considered to illuminate each element of the real scatterer and the produced interaction finally will be summed up over all elements of the scatterer.

The following subchapters will introduce some additional fundamentals, which are important to understand the potency of the technique. Finally the used diffraction equipment will be introduced.

2.6.1 Fundamentals

While in the specular x-ray reflectivity the reflection coefficient at interfaces is important due to different electron densities, here the transmission coefficient in the small angle regime and the penetration depth are of large interest.

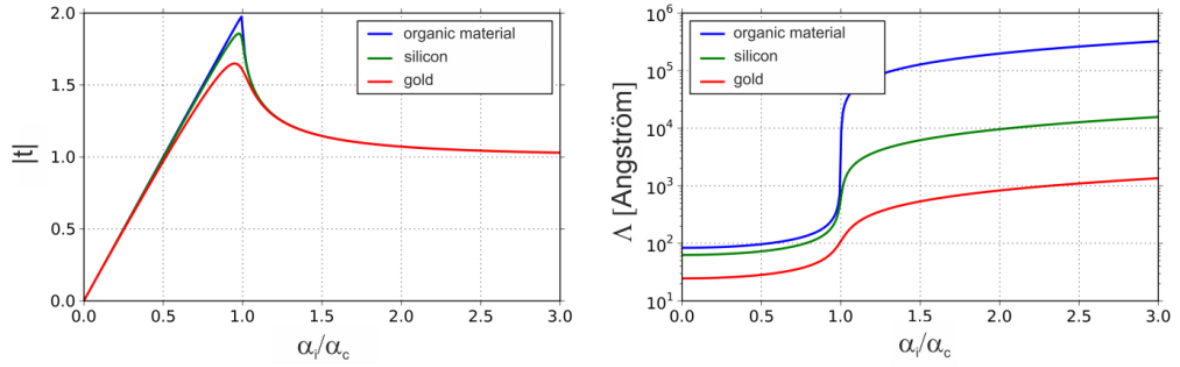


Figure 2.14: Absolute value of the transmission function (left) and the penetration depth Λ (right) for different materials as a function of the normalized angle of incidence α_i/α_c .

Considering eq. (2.60), the intensity transmittivity T is expressed by the incident angle and the critical angle of the x-ray beam (Daillant & Gibaud 2009). The transmitting part of the wave vector in x-direction is conserved, while $k_{t,z}$ (see eq. (2.49)) will now be extended with $n = 1 - \delta - i\beta$ by

$$k_{t,z} = k_0 \sqrt{n^2 - \cos^2(\alpha_i)} = k_0 \sqrt{n^2 - 1 + \sin(\alpha_i)^2} = k_0 \sqrt{\sin(\alpha_i)^2 - 2\delta - 2i\beta}, \quad (2.116)$$

(neglecting δ^2 -, $\delta\beta$, β^2 -terms), which introduces a complex part in the refraction. Thus the transmitted electrical field \mathbf{E}_t in z-direction can be written as

$$\mathbf{E}_t = t \mathbf{E}_0 e^{i(\mathbf{k}_t \cdot \mathbf{r} - \omega t)} \propto t e^{i(k_0 \cos(\alpha_i)x + \text{Re}\{k_{t,z}\}z)} e^{-\text{Im}\{k_{t,z}\}z}. \quad (2.117)$$

Using eq. (2.49) for small angles and neglecting absorption shows that $k_{t,z}$ becomes fully imaginary for $\alpha_i < \alpha_c$. Including this fact into eq. (2.117), a wave travelling parallel to the surface in x-direction, the so-called **evanescent wave**, is described. The evanescent wave is damped in z-direction by a factor $1/e$ and propagates with a penetration depth Λ of

$$\Lambda = \frac{\lambda}{\sqrt{2\pi}} \left\{ \sqrt{(\alpha_i^2 - \alpha_c^2)^2 + 4\beta^2} - (\alpha_i^2 - \alpha_c^2) \right\}^{-\frac{1}{2}}. \quad (2.118)$$

Figure 2.14 (right) illustrates the penetration depth for different materials with different electron densities. Λ is very low in the incidence beam range below the critical value and increases stepped at least for one order of magnitude at the critical angle.

Another important property of the transmission function eq. (2.60) is observed if the angle of incidence is equal to the critical angle. Here the intensity is maximized, which is

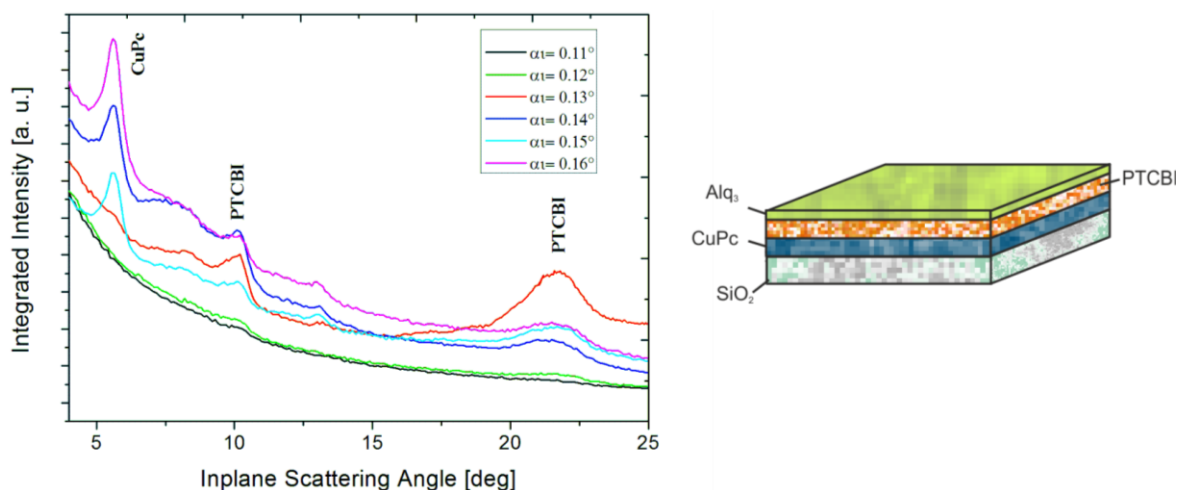


Figure 2.15: Integrated intensity linescans with respect to the in-plane scattering angle measured with GIXD with different angles of incidence of the x-ray beam (left) and the organic layer arrangement of the investigated stack (right).

described by a coherent coupling of the incident, the reflected and the transmitted field (Dosch 1992).

In Figure 2.14 (left) the transmission function reaches a maximum value of 2, which means that the theoretically observed intensity of the incident beam is enhanced by a factor of four and equal to $I_m = I \cdot |t|^2$. The maximum of the transmission function is frequently observed in GIXD experiments and the increased measured intensity at $\alpha_i = \alpha_c$ is called Yoneda wing (Yoneda 1963). The analogous observation will hold for the diffracted beam.

For organic materials the penetration depth is in a range of 5 nm at the critical angle and increases to 100 μm with higher angles of incidence. Next, one example of the surface sensitivity of the GIXD technique is shown. A multilayer stack, where three organic materials with different electron densities are deposited on top of each other was investigated by GIXD (Figure 2.15). Each organic layer comprises a layer thickness of ~ 30 nm, which is described in detail in chapter 3. Here the diffraction peaks of the individual materials appear and disappear by changing the angle of incidence of the beam. The amorphous Alq₃ top layer shows no contribution. However, by increasing α_i first diffraction features of the PTCBI layer arise (red line) followed by the diffraction feature of CuPc. At the highest α_i the lowest layer in the stack, the CuPc shows the highest diffraction intensity and the PTCBI content in the measurement almost vanished (purple line).

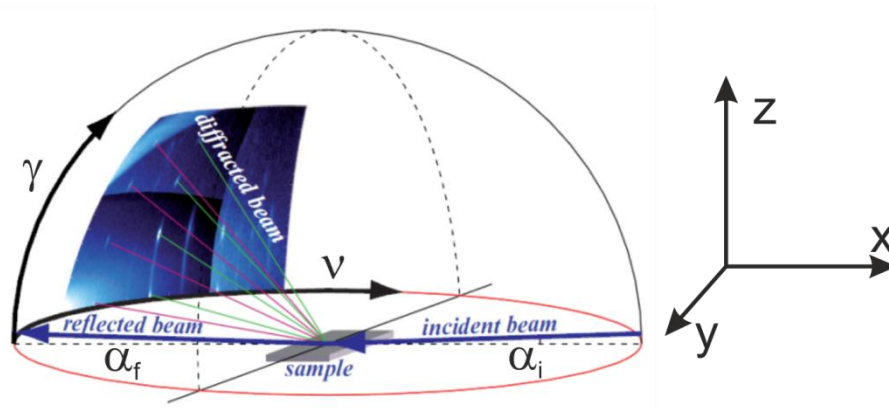


Figure 2.16: Schematic illustration of a GIXD geometry and a reciprocal space map obtained in the laboratory coordinate system (Salzmann 2009)

2.6.2 GIXD Experimental Setups

Grazing incidence x-ray diffraction is an in-plane scan and is sensitive to the netplanes of crystalline materials perpendicular to the surface horizon. As already discussed, the incident angle of the beam α_i is set to the critical angle of the investigated material to enhance the scattered intensity (see above), which is measured in our case with a 1D detector. The measurements are demonstrated in reciprocal space maps (RSM) using the out of plane component q_z and the in plane component $q_p = \sqrt{q_x^2 + q_y^2}$ of the scattering vector \mathbf{q} given by (Pietsch, Holy, & Baumbach 2004)

$$\begin{aligned} q_x &= \frac{2\pi}{\lambda} (\cos \alpha_f \cos \Theta_f - \cos \alpha_i \cos \Theta_i) \\ q_y &= \frac{2\pi}{\lambda} (\cos \alpha_f \sin \Theta_f + \cos \alpha_i \sin \Theta_i). \\ q_z &= \frac{2\pi}{\lambda} (\sin \alpha_i + \sin \alpha_f) \end{aligned} \quad (2.119)$$

Here Θ_i and Θ_f are the angles of the impinging and the detected wave with respect to the xz -plane. Figure 2.16 clearly illustrates the measurement geometry and demonstratively shows the interpretation of the measured data. The RSM is detected by rotating the detector and the sample on a goniometer by a common centre of rotation. The detector is moving along the xz - plane via the angle ν to determine the in-plane diffraction features and in the z - direction via the angle γ to observe the out of plane diffraction features. The RSM is finally calculated via the motor positions of the goniometer and the measured diffraction intensities. Depending on the used goniometer geometry one has to recalculate

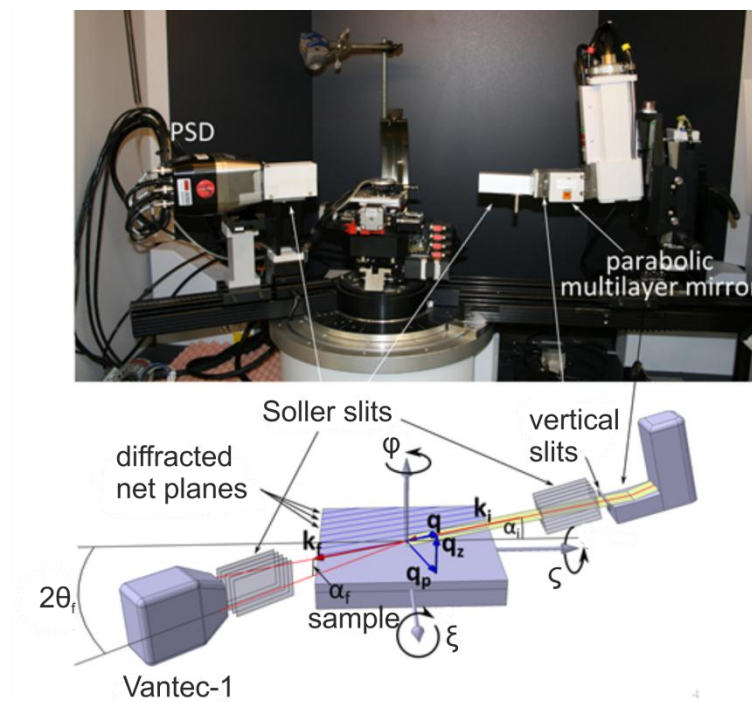


Figure 2.17: Image of the Bruker D8 Discover in GIXD geometry (top) and sketch of the experimental setup (bottom). (taken from (Neuschitzer 2012))

the coordinates from the laboratory coordinate system to the sample coordinate system to estimate the crystal system. In this work the self-made software PyGID, established by A. Moser (Moser 2012), was used to illustrate the RSM from the measured GIXD experiments of the laboratory equipment (Bruker) as well as from different synchrotron facilities (CHESS, HASYLAB, ESRF).

Laboratory Bruker D8 equipment:

The laboratory GIXD setup is realized on a 4-circle Bruker D8 Discover diffractometer modified with a Bruker Ultra GID add-on (Figure 2.17). The diffractometer is equipped with a conventional copper x-ray tube ($\lambda=1.5402 \text{ \AA}$), a long parabolic multilayer mirror (Schuster & Gobel 1995) acting as a monochromator, a primary slit (height: 0.6mm) and a Soller slit at the primary side. The secondary side consist of a secondary Soller slit and a position sensitive, one dimensional detector VANTEC-1 (Khazins *et al.* 2004). The goniometer is a 6-axis Euler cradle ($x, y, z, \varphi, \xi, \zeta$) and one has to use z – axis geometry, when using PyGID for RSM data evaluation (Moser 2012). Detailed information about the in-house GIXD setup is described by M. Neuschitzer *et. al* (Neuschitzer 2012).

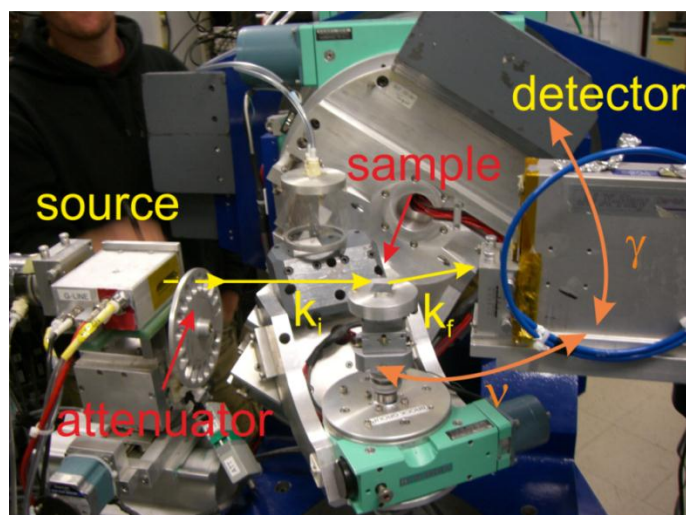


Figure 2.18: G2 diffractometer at CHESS. The goniometer angle ν corresponds to the Θ_f and the goniometer angle γ corresponds to α_f .

CHESS G2 beamline:

The RSM of the organic/inorganic multilayer photodiode investigation (chapter 3) has been measured at the G2 beamline at the synchrotron CHESS (Cornell High Energy Synchrotron Source) Ithaca, New York. There, radiation is generated by positrons, which circulate clockwise passing a 49-pole wiggler. The resulting wavelength of $\lambda=1.301 \text{ \AA}$ was set by a 0.5 mm thick single crystal beryllium (002) transmission monochromator. The G2 line is equipped with a six-circle kappa diffractometer supporting a large Soller collimator and a position-sensitive linear gas detector (ORDELA) with matching apertures of 8 mm horizontal and 100 mm vertical (Smilgies *et al.* 2005). A Helium atmosphere protected the sample from degradation during the beam exposure and an attenuator wheel in front of the sample saved the detector in terms of saturation. The sample was placed in the centre of the goniometer and the RMS was recorded by ν -scans for different detector elevations δ (Figure 2.18). The measurement data obtained from this goniometer setup are transformed in the PyGid software by using a *pseudo z-axis geometry* (Moser 2012).

HASYLAB W1 beamline:

Grazing incidence x-ray diffraction experiments were also performed at the W1 beamline of the synchrotron radiation source HASYLAB (Hamburg, Germany), which is based on the positron storage ring DORIS III ($E=4.45 \text{ GeV}$) and stimulated by a 16 – period wiggler. The x-ray radiation is set to a wavelength of 1.179 \AA by a Si(111) double crystal monochromator. The beamline is equipped with a primary slit system, a heavy-load

6+2 – circle goniometer, a flight tube with a secondary slit system and a one- dimensional position sensitive MYTHEN detector, which covers an out of plane range of 4° in one shot. Using a typical primary slit configuration of $0.2 \times 2 \text{ mm}^2$, the beam size at the sample is $1.4 \times 4 \text{ mm}^2$ and the beam divergence is $0.2 \times 2 \text{ mrad}^2$. During the measurements the samples were placed in a measurement chamber under He conditions and covered by an x-ray transparent graphite dome. For data evaluation one has to choose *pseudo 2+2 geometry* to correctly illustrate the RSM in the PyGID software package (Moser 2012).

ID10B at ESRF

Several experiments of this work were performed at the ID10B (TROIKA II) undulator beamline at the European Synchrotron Radiation Facility (ESRF) in Grenoble, France. The beamline uses photons in the range of 8 keV to 22.2 keV provided by a diamond (111) double – crystal monochromator and is perfectly suited to perform surface diffraction experiments as well as XRR experiments. Here, the wavelength of the x-ray beam was set to 1.54 \AA and the beam profile was set to $0.1 \text{ mm} \times 0.5 \text{ mm}$ (vertical x horizontal) by the primary slit optic. The beamline is equipped with a Huber goniometer where the sample can be either placed horizontally or vertically. GIXD measurements were performed with a one dimensional gas filled linear detector (GABRIEL/EMBL) with a large Soller slits in front, which will archive high azimuthal resolution. The samples were placed inside a He-filled measurement chamber. Specular x-ray reflectivity measurements were performed using a scintillation counter (CYBERSTAR) with slit optics in front of the detector. When using PyGID for data evaluation, one has to use the *pseudo z-axes geometry* (Moser 2012).

Part 2

II. EXPERIMENTAL

3 Structure and Morphology of an Organic/Inorganic Multilayer Stack: An X-ray Reflectivity Study

3.1 Motivation

The aim of this study was to characterize the structure of an organic/inorganic multilayer photodiode with different x-ray analysis methods as well as microscopy methods. The organic photodiode is implemented in an organic gas sensor, which was investigated and designed within the Cluster Project “Integrated Organic Sensors and Optoelectronic Technologies” (ISOTEC). The focus of the paper was set to the interfacial morphology of the multilayer stack as well as the crystallographic structure of the multilayer stack. The content of this study was equally contributed by myself and Stefanie Fladischer from the Institute for Electron Microscopy, Graz University of Technology. The manuscript was published in Journal of Applied Physics (AIP) and presented at several ISOTEC meetings and conferences. Figure 3.1 gives the copy of the head of the publication.

JOURNAL OF APPLIED PHYSICS **110**, 114911 (2011)

Structure and morphology of an organic/inorganic multilayer stack: An x-ray reflectivity study

Alfred Neuhold,^{1,a)} Stefanie Fladischer,² Stefan Mitsche,² Heinz-Georg Flesch,¹ Armin Moser,¹ Jiri Novak,¹ Detlef M. Smilgies,³ Elke Kraker,⁴ Bernhard Lamprecht,⁴ Anja Haase,⁴ Werner Grogger,² and Roland Resel¹

¹*Institute of Solid State Physics, Graz University of Technology, Petersgasse 16, 8010 Graz, Austria*

²*Institute for Electron Microscopy, Graz University of Technology and Center for Electron Microscopy, Steyrergasse 17, 8010 Graz, Austria*

³*Cornell High Energy Synchrotron Source (CHESS), Cornell University, Ithaca, New York 14850, USA*

⁴*Institute for Surface Technologies and Photonics, Joanneum Research Forschungsgesellschaft mbH, Franz Pichlerstrasse 30, 8160 Weiz, Austria*

(Received 29 June 2011; accepted 9 November 2011; published online 13 December 2011)

The internal morphology and crystallographic properties of a complete organic thin film multilayer stack are characterized via x-ray scattering techniques, atomic force microscopy (AFM), and scanning electron microscopy. The stack consists of the three organic layers – copper(II)phthalocyanine (CuPc), perylene tetracarboxylic bisbenzimidazole (PTCBI), and aluminum-tris(8-hydroxyquinolin) (Alq₃) – sandwiched between an optically semitransparent gold layer and a top silver electrode. The interface roughness progress is determined by the x-ray reflectivity, which is confirmed by the surface roughness determination via AFM. The crystallographic properties are characterized via x-ray diffraction. The CuPc layer is highly crystalline with preferentially oriented crystallites but forms a rough interface ($\sigma_{\text{RMS}} = 5.5$ nm) toward the PTCBI layer. The PTCBI layer grows with randomly distributed crystallites in a worm-like morphology with an interface roughness of $\sigma_{\text{RMS}} = 6.4$ nm toward the Alq₃ layer. The amorphous Alq₃ layer acts as smoothing layer and reduces the roughness σ_{RMS} to 5.8 nm. Within this study we demonstrate the applicability of x-ray reflectivity in characterizing the interface morphology of an organic multilayer stack device.

© 2011 American Institute of Physics. [doi:10.1063/1.3667171]

Figure 3.1: Copy of the head of the publication

3.2 Introduction

Stacks of thin organic films, which are sandwiched between inorganic materials, are of increased interest due to ongoing research in organic electronics. The respective devices covers a large number of applications like organic solar cells, light emitting devices, organic thin film transistors, etc. with a huge commercial demand due to its potential of low-cost fabrication or device miniaturization. The organic layers can be prepared by various deposition techniques like spin coating (Burroughes *et al.* 1990), organic vapor-phase deposition (Baldo *et al.* 1997)(Yang, Shtein, & Forrest 2005) or vacuum thermal evaporation (Tang & VanSlyke 1987)(Tang, VanSlyke, & Chen 1989)(Van Slyke, Chen, & Tang 1996). The structural properties of thin films like the alignment of the molecules relative to interfaces or the interface roughness, influence the device performance decisively (Mäkinen *et al.* 1999)(Dane *et al.* 1998). Therefore, a knowledge of morphology, defined crystallographic properties of the involved organic materials and especially a defined interface roughness in a multilayer arrangement is necessary for reliable and optimized device performance (de Boer *et al.* 2005)(Tang 1986).

In general x-ray scattering methods are widely used for the characterization of the structure and the organization of inorganic as well as organic materials which are grown as thin film layers (de Boer *et al.* 1998)(Vineyard 1948). In this study we determine the interface morphology of a stack of six organic / inorganic heterolayers by x-ray scattering(Gibaud & Hazra 2000) methods relate it to the crystallographic properties of the involved layers and compare the results with microscopic investigations.

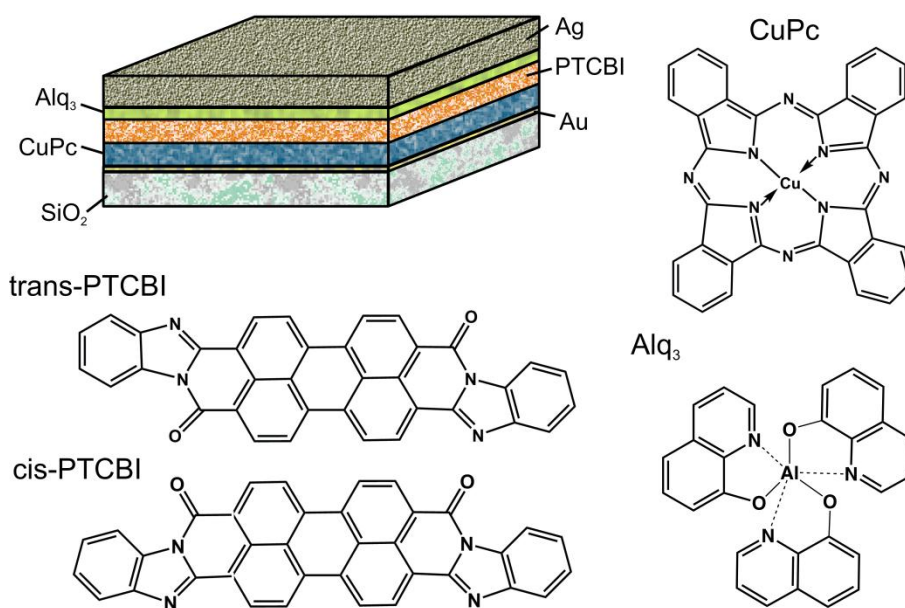


Figure 3.2: Multilayer arrangement of the organic photodiode on Si/SiO₂ substrate and the chemical structure of Copper (II) phthalocyanine (CuPc), trans- and cis- perylene tetracarboxylic bisbenzimidazole (trans-PTCBI) (cis-PTCBI) and aluminium-tris(8-hydroxyquinolin) (Alq₃), sandwiched between a gold and a silver electrode.

3.3 Experimental

Materials and multilayer preparation: Copper(II)phthalocyanine (CuPc) and aluminium-tris(8-hydroxyquinolin) (Alq₃) (provided by Sigma-Aldrich) and perylene tetracarboxylic bisbenzimidazole (PTCBI) (from SynTec GmbH) were purified two-times by thermal gradient sublimation before usage. Silicon wafers with a 100 nm thermal oxidized SiO₂ layer on top (from SilChem GmbH) were used as substrates. The multilayer arrangement (Figure 3.2) consists of stacked layers starting with a thin optically semitransparent Au layer followed by a CuPc layer, a PTCBI layer, an Alq₃ layer and an Ag top electrode. All these layers were prepared by physical vacuum deposition under high vacuum of $\sim 10^{-7}$ mbar at room temperature, except for the gold electrode, which was deposited by sputtering under high vacuum conditions ($\sim 10^{-5}$ mbar). The growth rate of the organic layers was 0.3 nm/s and the nominal thicknesses of the Au, CuPc, PTCBI, Alq₃ and Ag layers on Si/SiO₂ were 8.3 nm, 40 nm, 40 nm, 20 nm and 100 nm, respectively, as determined by a quartz crystal thickness monitor. This investigated stack system is used in a real device application with glass and plastic foil (PET) as substrates. It works as an organic photodiode and is used as detector unit in an opto-chemical sensor for multi analyte detection (Kraker *et al.* 2009) (Lamprecht *et al.* 2010).

X-ray methods: The specular x-ray diffraction (XRD) and x-ray reflectivity (XRR) measurements were performed on a Bruker D8 Discover diffractometer set up in Bragg-Brentano configuration using Cu K α radiation ($\lambda = 1.542 \text{ \AA}$). Conventional slit optics were used in combination with a graphite monochromator on the secondary side. For XRR measurements a slit setting of 0.05 mm / 0.1 mm / 0.1 mm (primary slit/anti scatter slit/receiving slit) was used and for XRD measurement the slit setup was changed to 0.2 mm / 0.2 mm / 0.2 mm. The measured XRR data were simulated with the software package WinGixa (Almelo 1997), which determines the layer thickness and electron density by fitting the data with Parratt's recursive formalism (Parratt 1954). The surface roughness and the interface roughness of the specimen were determined using the Nevot and Croce approach (Croce & Névo 1976). The difference between experimental result and fitted data are given as residuals. To cross check these results, pattern simulations were performed with X'Pert Reflectivity 1.3 software (PANalytical). This software package comprises a genetic fitting algorithm (Dane *et al.* 1998), which finds the vicinity of the global optimum of the fit and uses the Marquardt-Levenberg algorithm to finally optimize the parameters to the found local minimum. The error estimation of the fitting parameters corresponds to the chapter 15.6 of the Numerical Recipes (Press *et al.* 2007). Within the algorithm the error of one parameter is estimated while the other parameters were treated as fixed. Besides specular XRD, also grazing incidence x-ray diffraction (GIXD) measurements were performed to characterise crystallographic properties of the layers. GIXD experiments have been performed at the G2 beamline (Smilgies *et al.* 2005) ($\lambda = 1.301 \text{ \AA}$) at the synchrotron CHESS (Cornell High Energy Synchrotron Source) Ithaca, New York. A Helium atmosphere protected the sample from degradation during the beam exposure. The incidence angle ($\alpha_i = 0.15^\circ$) of the primary beam was optimized to maximize the scattering intensity from the multilayer; the scattered beam was detected with a one-dimensional position sensitive detector. The results of in-plane GIXD measurements are presented in form of reciprocal space maps, using the out of plane (q_z) and in-plane (q_p) components of the scattering vector q as coordinates (Pietsch, Holy, & Baumbach 2004). GIXD is complementary to specular XRD, since GIXD probes different volumes in the k -space.

Determination of the electron density profile: The electron density profile of the multilayer arrangement was calculated from the refraction index decrement $\Delta\rho$ of the individual materials together with the roughness and thickness of the individual layers, which have been determined by XRR measurements by using the effective density model

chapter 2.3.3. Thereby it is possible to construct the electron density progress $\rho_{el}(z)$ (perpendicular to the substrate surface) based on an initial guess of the dispersion δ_j , layer roughness σ_j and the interface position in z-direction of each layer.

$$\rho_{el}(z) = \frac{2\pi\delta(z)}{\lambda^2 r_e} \quad (3.1)$$

r_e denotes the classical electron radius ($r_e = 2.818 \times 10^{-15}$ m) and λ stands for the wavelength of the used x-rays.

Microscopy methods: Atomic force microscopy (AFM) measurements were performed on a Dimension 3100 microscope equipped with a hybrid closed loop scan head and a Nanoscope IVa controller (Digital Instruments, VEECO). All measurements were done in tapping mode with different Olympus cantilevers (2 - 40 N/m) depending on the sample characteristics. Scanning electron microscopy (SEM) was performed with a Zeiss Ultra 55 microscope equipped with a field emission gun. The high resolution images were recorded with a high efficiency in-lens secondary electron detector at an acceleration voltage of 3 kV.

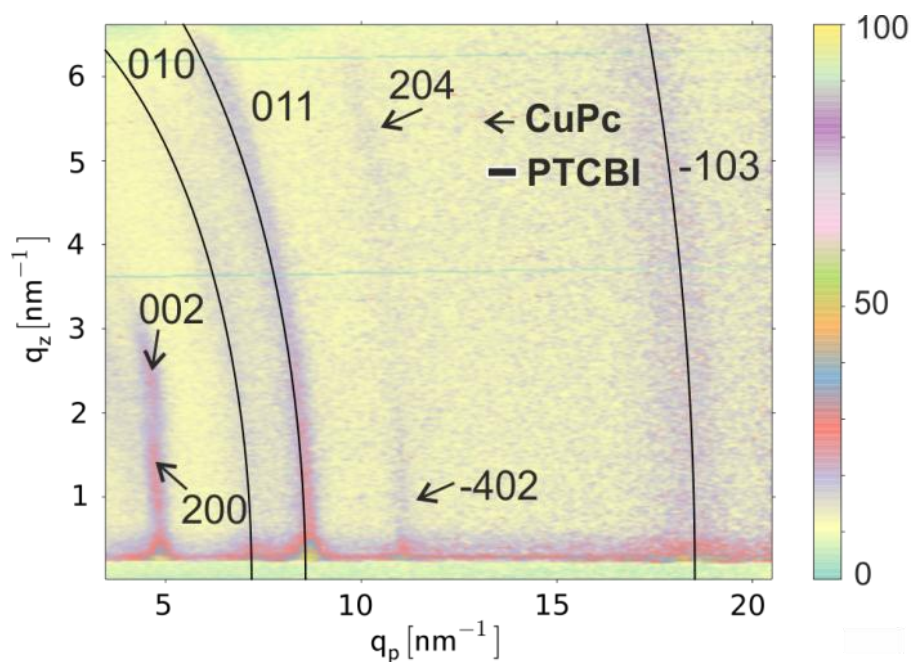


Figure 3.3: Reciprocal space map of the Si/SiO₂/Au/CuPc/PTCBI/Alq₃-stack. The diffraction spots of α -CuPc crystallites (arrow) and the diffraction rings from PTCBI crystallites (lines) are denoted by their Laue indices. No diffraction signal is observed from Alq₃.

3.4 Results and Discussion

X-ray diffraction results: Specular XRD scans were performed on the multilayer samples consisting of the four bottom layers (Au, CuPc, PTCBI and Alq₃). The 111, 200 and 220 reflections of crystalline gold are observed. However, the other weak diffraction peaks could not be clearly assigned to the organic layers. Therefore the involved crystallographic structures of the organic layers as well as the preferential orientation of the crystallites have to be determined by GIXD (Moser *et al.* 2009). The experimental result is given in Figure 3.3. Clear diffraction features of CuPc are identified: 200 and 002 as the main peaks and barely visible 204 and -402 peaks. The CuPc layer in the organic multilayer arrangement on top of the Au layer forms the α -phase ($a= 2.592$ nm, $b= 0.379$ nm, $c= 2.392$ nm, $\beta= 90.4^\circ$) (Resel *et al.* 1999). A comparison with the crystallographic structure reveals that the CuPc crystallites are preferentially oriented as a two – dimensional powder with the (427) plane parallel to the substrate surface. The crystallographic properties are used to determine the orientation of the molecules relative to the substrate surface: the disc-like CuPc molecules are lying with a 12° tilt of the π – conjugated plane relative to the gold surface, which has been previously observed as the preferred orientation plane of CuPc on gold (Floreato *et al.* 2008). The ring-like features in

the GIXD pattern of Figure 3.3 correspond to randomly distributed crystallites of PTCBI. PTCBI exists as a trans-isomer (Mizuguchi 2005a) and a cis-isomer (Mizuguchi 2005b), a mixture of these two isomers is obtained from syntheses as a racemic mix-PTCBI (Dhagat *et al.* 2009)(Rim *et al.* 2007), which was used for this work. By slightly changing the unit cell of the trans-isomer it was possible to index the observed diffraction rings ($a= 0.529$ nm, $b= 0.903$ nm, $c= 1.337$ nm, $\alpha= 89.4^\circ$, $\beta= 91.2^\circ$, $\gamma= 104.8^\circ$), so that the known crystal structure is slightly distorted. The PTCBI crystallites show no texture on top of the CuPc layer and yield 010, 011 and -103 diffraction features. The Alq₃ layer could not be detected directly by x-ray diffraction measurements, neither in the multilayer stack nor in a single layer. Therefore, it is concluded that Alq₃ forms an amorphous state.

Microscopy results: Figure 3.4 gives characteristic AFM images of multilayer stacks with different number of layers. The corresponding images are used to determine the surface roughness of each layer. The sputtered Au layer grows smoothly, but the layer does not fully cover the substrate due to its island like growth (Kaune *et al.* 2009); it has a RMS roughness of 0.3 nm (Figure 3.4a). The following CuPc layer forms islands on top of the Au layer, with a significantly higher surface roughness ($\sigma_{\text{CuPc}} = 6.1$ nm) (Figure 3.4b). The PTCBI crystallites on top of the CuPc layer cause a slight increase of the surface roughness to 7.4 nm (Figure 3.4c), while the deposited Alq₃ decreases the surface roughness to 6.8 nm (Figure 3.4d). The AFM image of the top metal film (not shown) in the multilayer system evidences again a rough Ag surface ($\sigma_{\text{Ag}} = 8.0$ nm).

In addition to the AFM measurements, SEM images were used to assess the morphology of each layer in the multilayer stack. The Au layer evidences again the island growth (Figure 3.5a), while the CuPc layer on top of the Au layer exhibits a closed layer with rather big crystallites. SEM images reveal worm-like islands of the PTCBI crystallites (Rim *et al.* 2007) (Figure 3.5c), which are hardly visible by AFM investigations. The SEM image shows directly the flattening of the surface after the deposition of Alq₃, however, this worm-like morphology is still visible after the deposition of the Alq₃ layer (Figure 3.5d).

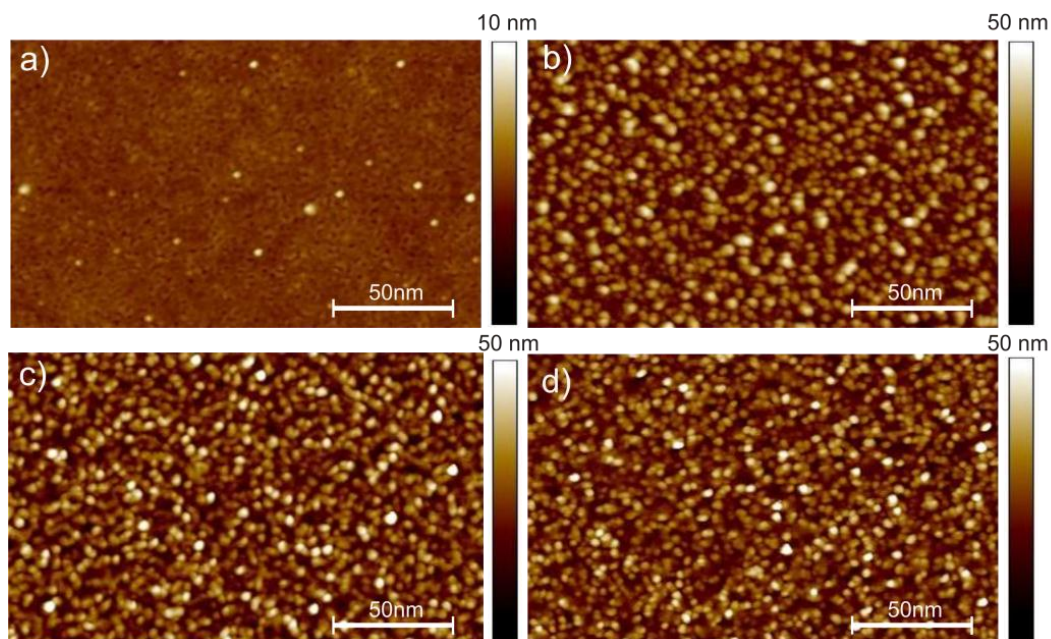


Figure 3.4: Atomic force microscopy images of the multilayer arrangement with different top layers: Au surface (a), CuPc surface (b), PTCBI surface (c) and Alq₃ surface (d).

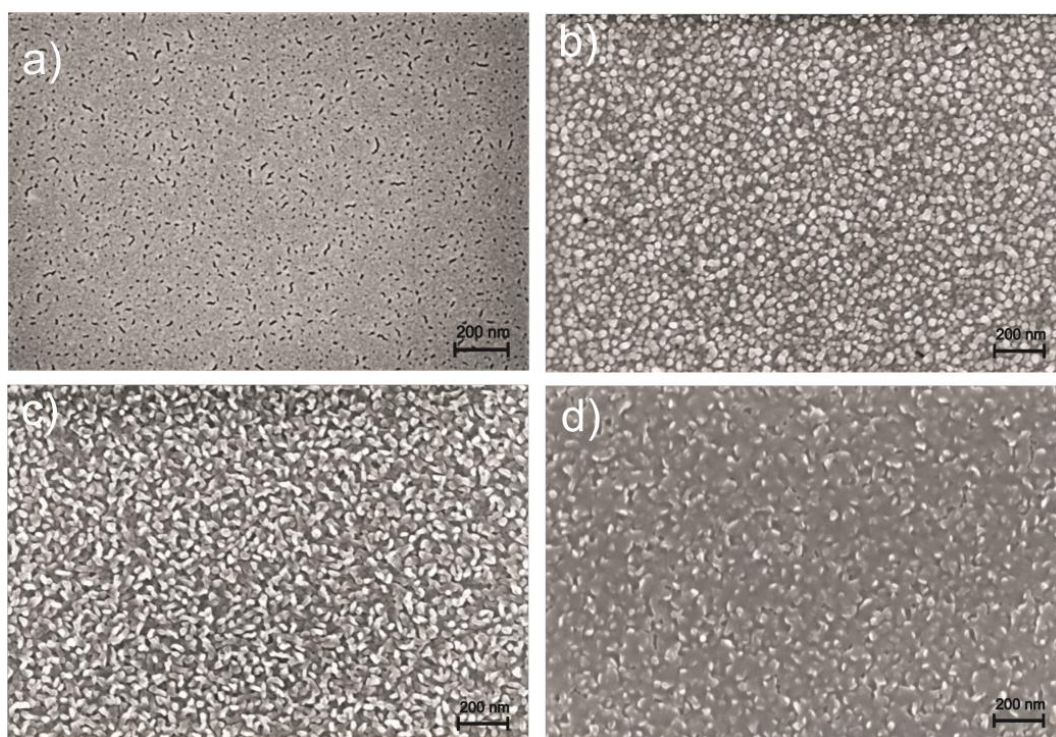


Figure 3.5: Scanning electron microscopy images of the multilayer arrangement with different top layers: Au surface (a), CuPc surface (b), PTCBI surface (c) and Alq₃ surface (d).

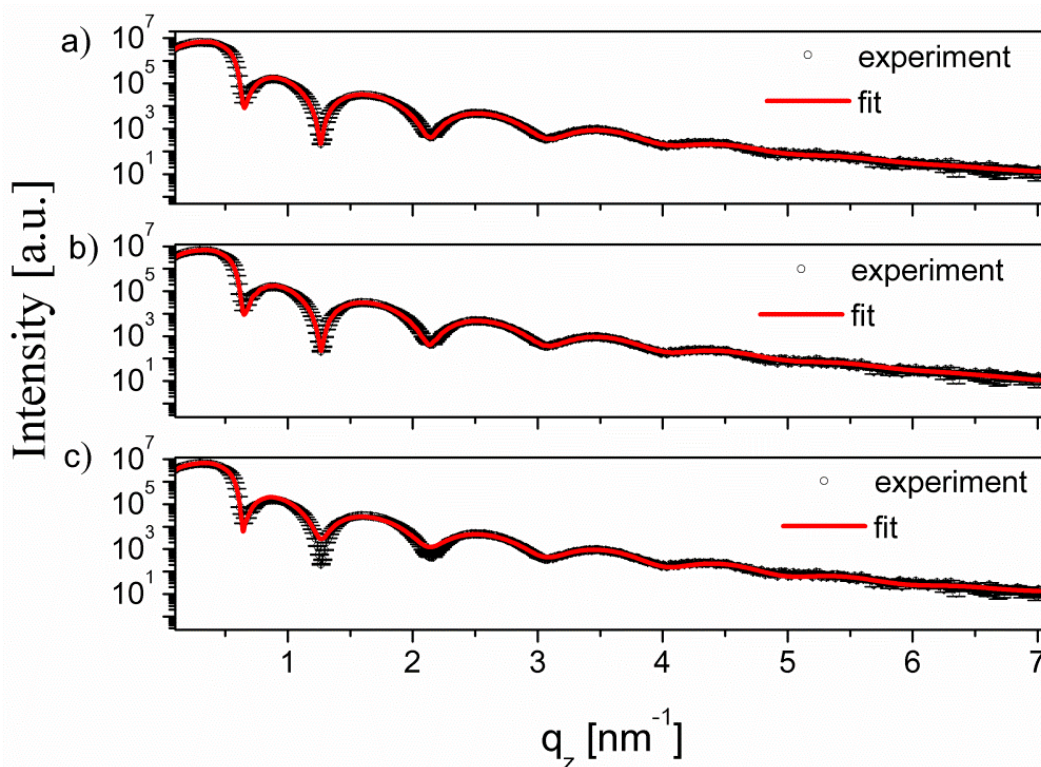


Figure 3.6: (a) Specular x-ray reflectivity intensity of the Si/SiO₂/Au/CuPc/PTCBI/Alq₃/Ag multilayer device as a function of the reciprocal space vector q_z (6-layer system). (b) Same specular x-ray reflectivity graph as in (a) but fitted with one pseudo organic layer between the metal electrodes (4-layer-system) and (c) shows the fit without any organic layers between the metal electrodes (3-layer-system). The experimental result and the fit to the experimental data are given by black symbols and a red solid line, respectively.

X-ray reflectivity results. Figure 3.6 a) comprises the measured multilayer x-ray reflectivity curve of the whole device including the Ag top electrode. The experimental curves are fitted to get layer thicknesses, mean electron densities of the individual layers and surface / interface roughness values. A proper choice of starting parameters is essential to get reliable results of the fitting procedure. The input parameters for layer thicknesses and roughnesses are taken from single layer investigations on Si/SiO₂ substrates as well as from multilayer arrangements of the organic materials on Si/SiO₂ substrates (see chapter 0). The electron densities of the individual layers are taken from their single crystal structures. The fitted experimental quantities and the goodness of fit values are given in Table 3.1.

Since gold as well as silver have an electron density which is one order of magnitude larger than organic materials, the XRR curve is dominated by these two metals. Therefore the experimental data has been fitted by three different models: the whole inorganic / organic multilayer stack (6 – layer system), a model where the three organic layers were treated as

one (4 – layer system) and a model without any organic layer between the metal electrodes (3 – layer system). The scattering contribution from the organic materials is hardly visible in Figure 3.6 a) (6 – layer model). However, an omission of the organic layers between the gold and the silver layer leads to a worse fit (3 – layer system, Figure 3.6 c)) and additionally to unrealistic values for the involved electron densities of the gold and silicon oxide layer (3-layer-system, Table 3.1). In both cases, the obtained values are larger than the value determined from the crystal structure. The differences between the experimental curve and the fitted data are clearly visible at the minima of the Kiessig fringes (Kiessig 1931). The quality of the fit increases by in-cooperation of one single organic layer between the two metal electrodes (Figure 3.6 b), 4-layer-system) and gives the best goodness of fit value from the simulation. However, the fit reveals an electron density value far-off from a physical plausible value of the used organic materials as well as of gold (compare Table 3.1). Therefore, the 6 – layer system, with the worse goodness of fit value, comprises the physical relevant information.

The fit including all layers (6 – layer system) yields the following values: The SiO₂ layer shows a thickness of 101.5±5.1 nm followed by the 6.2±0.1 nm thick gold layer measured by XRR. These two layers are very smooth with a roughness of 0.2±0.1 nm and 0.5±0.1 nm, respectively. The thermally deposited organic layers grow with a thickness of 30.9±3.1 nm, 36.0±3.8 nm and 19.7±0.9 nm for the CuPc, PTCBI and Alq₃ layer, respectively. Large roughness values are obtained at the CuPc / PTCBI as well as at the PTCBI / Alq₃ interfaces, while the interface between Alq₃ and Ag is considerably smoother. The top silver electrode has a thickness of 53.5±1.5 nm and a roughness of 6.8±0.7 nm. The interface roughness of the organic layers from the fit increased significantly from the Au layer to the CuPc layer ($\sigma = 5.5 \pm 0.6$ nm) and the PTCBI layer ($\sigma = 6.4 \pm 0.7$ nm). This can be attributed to the high ability for crystallisation of these two materials which is connected with rapid islanding of the organic layer during the deposition process (Petráček 1995). The Alq₃ layer smoothed the interface ($\sigma = 5.8 \pm 0.4$ nm) in the multilayer arrangement, probably due to the formation of an amorphous arrangement of the molecules. Perlich et al. show the tendency of the roughness progress in a multilayer stack using grazing incidence small angle x-ray scattering (GISAXS), however no surface roughness values from the out-of-plane line scans have been specified (Perlich *et al.* 2009). In Table 3.1, a comparison of the AFM surface roughness and the XRR interface roughness for this multilayer stack system is depicted. An excellent agreement of the described roughness progress in the device

arrangement is obtained. In addition, the expected electron density ρ_{crystal} of each material is comparable to the calculated electron density ρ_{XRR} from the XRR data of the real multilayer stack. The Au layer shows a lower electron density compared to the expected value derived from the single crystal structure. Interestingly, the same electron density is obtained by the single layer fit of Au on the Si/SiO₂ substrate ($\rho_{\text{el}} = 4.36 \text{ \AA}^{-3}$) which is shown in the Supplementary Information. Even in case of CuPc the observed electron density is slightly smaller than the expected one. Probably in both cases the islanding or cluster formation during the film formation leads to a reduced average electron density of the layer (Venables, Spiller, & Hanbücken 1984).

Table 3.1: Structural parameters of the individual layers stacked within the organic multilayer stack determined by different experimental methods. The fits were performed for the complete 6-layer system, a 4-layer system where a single organic layer were introduced between the Au layer and the Ag layer and a 3-layer system considering only the involved inorganic layers (SiO₂, Au, Ag).^a

layer	d_{XRR} (nm)	σ_{XRR} (nm)	σ_{AFM} (nm)	$\rho_{\text{crystal}}(1/\text{\AA}^{-3})$	$\rho_{\text{XRR}}(1/\text{\AA}^{-3})$
6-layer system	(goodness of fit value = 83.3)				
SiO ₂	101.5±5.1	0.2±0.1	-	0.67	0.67±0.01
Au	6.2±0.1	0.5±0.1	0.3	4.42	4.36±0.09
CuPc	30.9±3.1	5.5±0.6	6.1	0.80	0.79 ±0.04
PTCBI	36.0±3.8	6.4±0.7	7.4	0.50	0.45±0.04
Alq ₃	19.7±0.9	5.8±0.4	6.8	0.45	0.43±0.02
Ag	53.5±1.5	6.8±0.7	8.0	2.76	2.70±0.03
4-layer system	(goodness of fit value = 75.4)				
SiO ₂	101.5±5.1	0.2±0.1		0.67	0.80±0.01
Au	6.2±0.1	0.5±0.1		4.42	4.49±0.06
organic layer	87.6±4.1	2.7±0.8		-	1.05±0.02
Ag	54.4±1.1	6.8±0.7		2.76	2.69±0.03
3-layer system	(goodness of fit value = 143.6)				
SiO ₂	101.5±5.1	0.2±0.1		0.67	0.80±0.01
Au	6.3±0.1	0.4±0.1		4.42	4.65±0.10
Ag	48.9±0.8	6.9±0.7		2.76	2.74±0.05

^a The layer thickness (d_{XRR}), the interface roughness (σ_{XRR}) and the total electron density ρ_{XRR} of the layers are determined by the x-ray reflectivity investigation. For comparison the surface roughness obtained from atomic force microscopy (σ_{AFM}) and the electron densities derived from the crystal structures (ρ_{crystal}) are given.

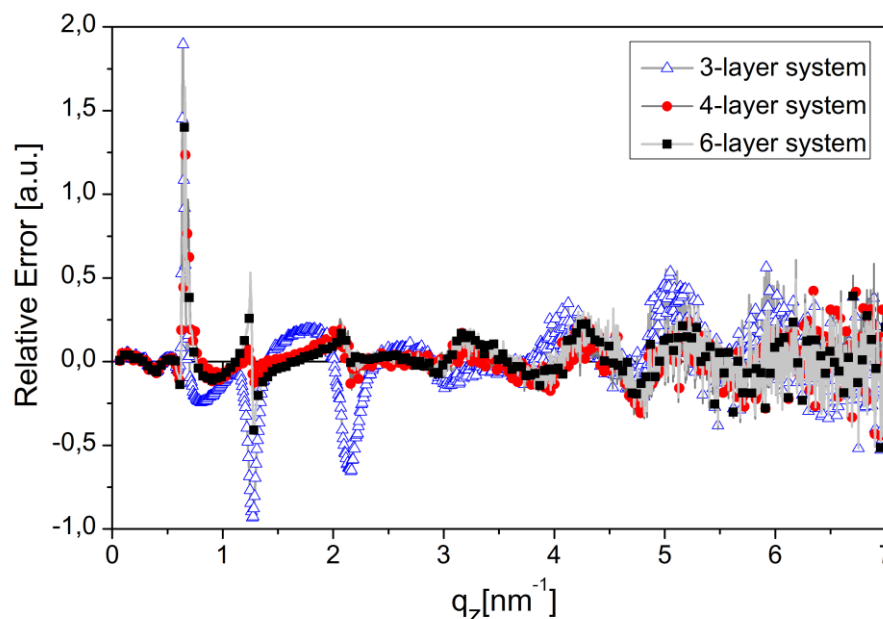


Figure 3.7: Comparison of the relative fit errors of the 3-layer system (full circle), 4-layer system (triangle) and the 6-layer system (full rectangle)

A comparison of the calculated relative errors of the experimental data and the fit of the investigated systems (Figure 3.7) underlines additionally the distinct result. The best realistic fit was accomplished with the 6 – layer system comprising all three deposited organic layers. At small reciprocal space vectors ($q_z = 0.65 \text{ nm}^{-1}$) the relative error of the 3 – layer system shows the highest discrepancy. The deviation of the 3 – layer fit without organic layers increases with increasing q_z , additionally the resulting electron density of the Au layer shows an unrealistic value. The 4 – layer system with just one single organic layer between the two metal layers shows a smaller relative error, however the resulting electron density of the organic layer is far-off an expected electron density value of the used organic materials.

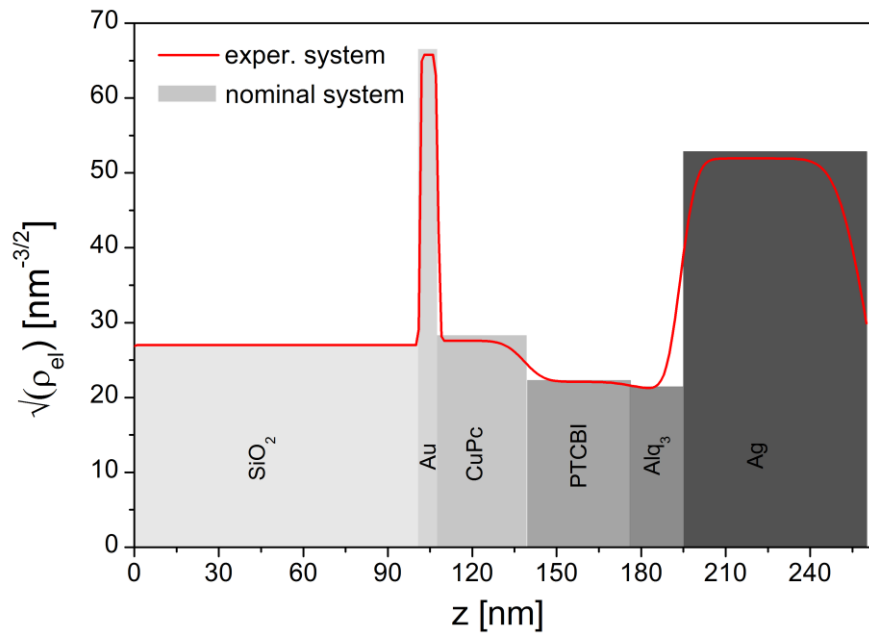


Figure 3.8: Nominal (grey areas) and real (red line) electron density profile of the Si/SiO₂/Au/CuPc/PTCBI/Alq₃/Ag multilayer stack perpendicular to the substrate surface.

Electron density profile: Figure 3.8 shows the variation of the total electron density perpendicular to the sample surface of the multilayer arrangement. The nominal electron density of ideal smooth layers is compared to electron densities of the individual materials taken from single crystal structures. The interface roughness of each individual layer results in smearing along the electron density profile.

The low roughness at the SiO₂ / Au and Au / CuPc interfaces result in a rapid change in the electron density. However, the high interface roughness at the CuPc / PTCBI interface leads to a much weaker change in the electron density which is clearly smeared out. The difference in the electron density at the PTCBI / Alq₃ interface is hardly visible since both materials show a comparable value. However, the electron density at the interface between Alq₃ and Ag is again clearly smeared out, which can be explained by intermixing of these two materials during layer fabrication by thermal evaporation. Two possible reasons can be given for the intermixing: on the one hand the surface roughness of the Alq₃ layer after the deposition together with filling of the surface roughness by Ag during the subsequent deposition process and on the other hand the penetration of Ag into the organic layer. Both processes may occur simultaneously and assist each other. Further investigations will be focused on the top metallic/organic interface, where XRR investigations can be used to simulate metal diffusion into the organic thin film. These interface roughnesses might influence the device performance significantly (Chiesa *et al.* 2005)(Kim *et al.*

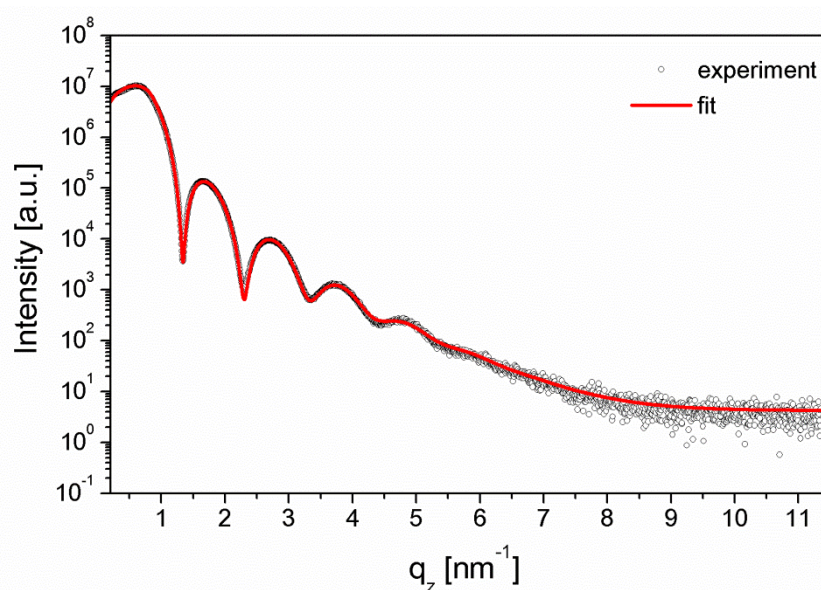
2011)(Blochwitz *et al.* 2001). Exciton diffusion length, exciton separation probability and diffusion possibility of electrons and holes are strongly depending on the interface morphology in the multilayer stack, e.g. a smoother CuPc / PTCBI interface might decrease the exciton separation yield and therefore decreases the external quantum yield of the organic multilayer photodiode. In addition, a smoother PTCBI / Alq₃ interface could reduce the interface traps for the electrons. However, these suggestions strongly depend on the used materials and its functionality within the devices (Peumans, Yakimov, & Forrest 2003)(Waldauf *et al.* 2006).

3.5 Conclusion

An application relevant stack of organic and inorganic layers was characterized by x-ray scattering techniques and microscopy techniques to reveal the crystallographic properties and the internal morphology of the multilayer arrangement. Grazing incidence x-ray diffraction provided some insight into the crystalline properties of the layers: CuPc crystallises in the α -phase as a two-dimensional powder, PTCBI grows with randomly distributed crystallites and Alq₃ forms an amorphous phase. X-ray reflectivity was used to extract the exact layer thicknesses, the interface roughness and information about the electron density of each material in the multilayer stack systems. Although the XRR curve is dominated by the scattering contribution of the Au and Ag layers, the consideration of organic layers is required to get reliable fits of the experimental data. Even an introduction of a single organic layer instead of a stack of three layers does not lead to a reasonable result and proper electron density values. However, good starting parameters are required to fit a multilayer stack consisting of six layers, taken from the XRR investigations of single layers and multilayers. Despite a smooth Au bottom layer a high roughness is observed at the CuPc / PTCBI interface. This can be explained by the strong tendency of crystallisation of CuPc. The interface roughness at the PTCBI / Alq₃ interface does not change much. However, the Alq₃ layer rather smoothens the organic stack system, probably due to the amorphous structure of the material. The evolution of the interface roughness and the morphology of the individual materials on top of each other were cross-checked by atomic force microscopy and scanning electron microscopy. Using all information the electron density profile of the whole device could be determined within the organic multilayer stack system.

3.6 Acknowledgement

The authors thank the Austrian Research Promotion Agency (FFG) for Supplementary this work within the research project cluster “Integrated Organic Sensor and Optoelectronic Technologies” (ISOTEC). We thank Arthur R. Woll for his assistance in using the beamline G2. This work is based upon research conducted at the Cornell High Energy Synchrotron Source (CHESS) which is supported by the National Science Foundation and the National Institutes of Health/National Institute of General Medical Sciences under NSF award DMR-0936384.

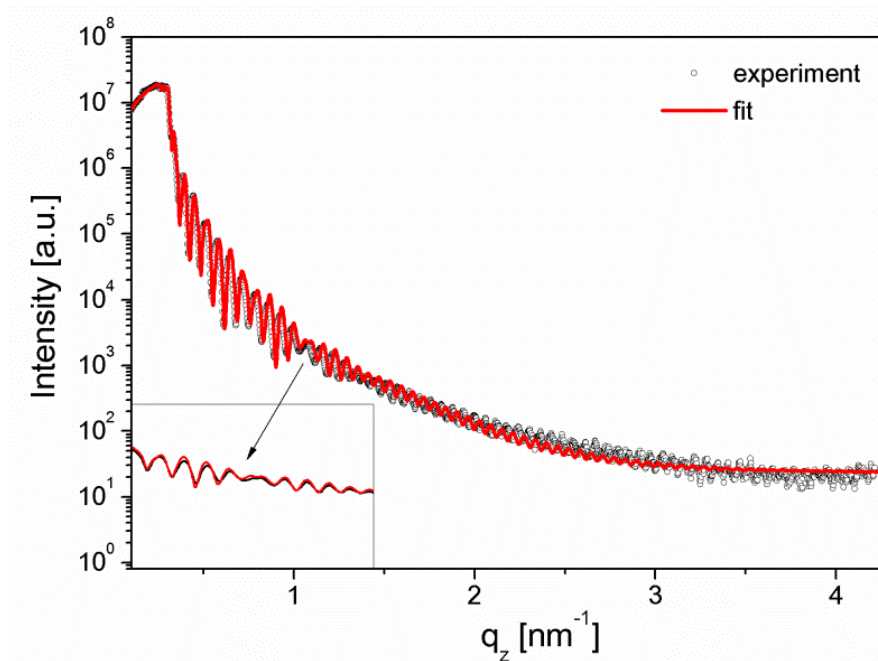


Suppl. Figure 3.1: X-ray reflectivity fit of the Si/SiO₂/Au stack

3.7 Supplementary Information

Additional measurements support the arguments of the main publication and underline the main results.

X-ray Reflectivity Results: The organic materials were deposited individually on several Si/SiO₂ substrates and x-ray reflectivity (XRR) measurements were used to get the trend of layer thickness, surface and interface roughness as well as electron densities of these thin layers in the multilayer arrangement. The extracted information of the individual organic layers was used as the starting parameters of the complete 6 – layer stack fit. Suppl. Figure 3.1 shows the Au layer on the silicon wafer and Suppl. Table 3.1 summarize the corresponding fitting results. In particular the resulting electron density of the Au layer on the silicon wafer gives a trustful value, which is also observed in the multilayer arrangement of the 6 – layer system in the main manuscript.



Suppl. Figure 3.2: X-ray reflectivity fit of the Si/SiO₂/CuPc/PTCBI/Alq₃ stack

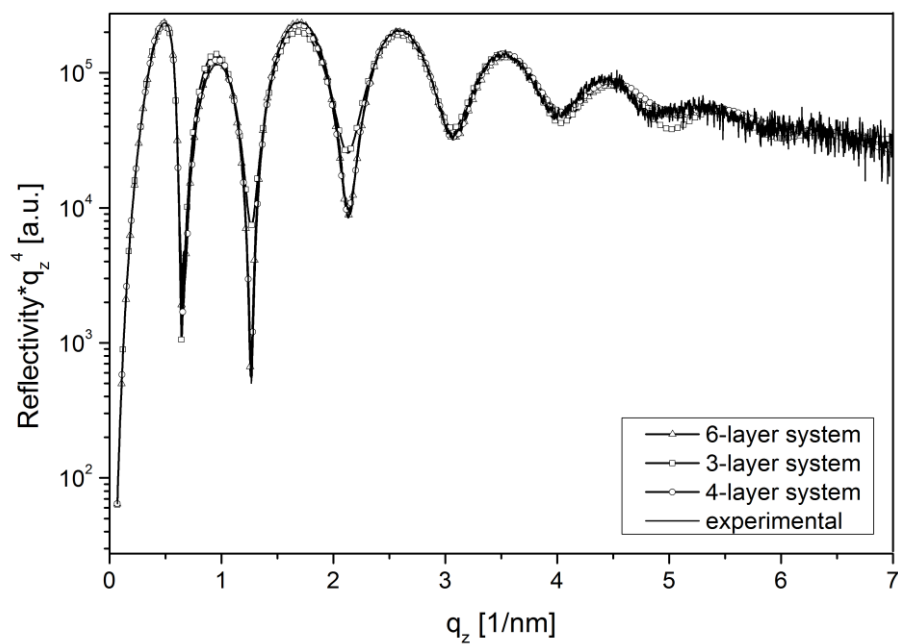
Suppl. Table 3.1: XRR fit parameter of the Au layer on Si/SiO₂. d_{XRR} denotes the measured thicknesses of the layers, σ_{XRR} describes the roughness and ρ_{XRR} denote the electron densities of the individual layers from XRR measurement. Additionally, the electron densities derived from the crystal structures (ρ_{crystal}) are given.

layer	$d_{\text{XRR}}(\text{nm})$	$\sigma_{\text{XRR}}(\text{nm})$	$\rho_{\text{crystal}}(1/\text{\AA}^{-3})$	$\rho_{\text{XRR}}(1/\text{\AA}^{-3})$
SiO ₂	101.5±4.9	0.2±0.1	0.67	0.67±0.01
Au	5.8±0.4	0.5±0.1	4.42	4.36±0.09

Suppl. Figure 3.2 shows the three organic layers (CuPc/PTCBI/Alq₃) on the silicon wafer and the extracted parameters were again used as a first guess for the whole multilayer fit. The fitting parameters of this arrangement are comprised in Suppl. Table 3.2.

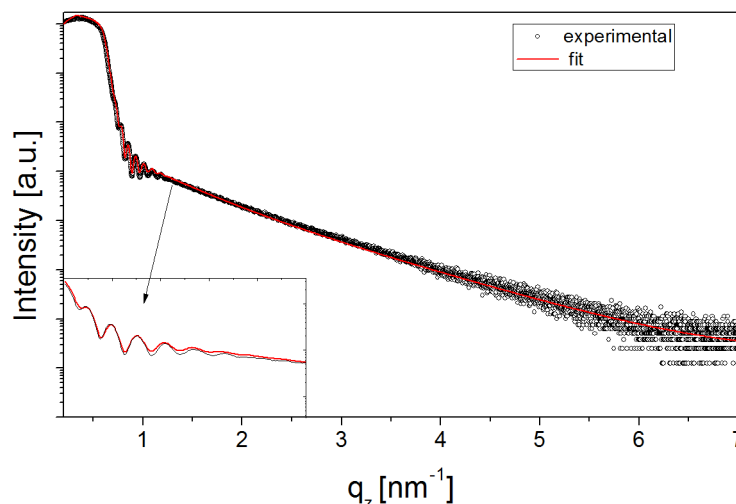
Suppl. Table 3.2: XRR fit parameter of the CuPc/PTCBI/Alq₃ layers on Si/SiO₂. d_{XRR} denotes the measured thicknesses of the layers, σ_{XRR} describes the interface roughness and ρ_{XRR} denote the electron densities of the individual layer from XRR measurement. Additionally, the electron densities derived from the crystal structures (ρ_{crystal}) are given.

layer	$d_{\text{XRR}}(\text{nm})$	$\sigma_{\text{XRR}}(\text{nm})$	$\rho_{\text{crystal}}(1/\text{\AA}^{-3})$	$\rho_{\text{XRR}}(1/\text{\AA}^{-3})$
SiO ₂	100.5±5.1	0.45±0.1	0.67	0.67±0.01
CuPc	29.9 ±0.7	2.5 ±0.2	0.80	0.52±0.25
PTCBI	37.2±0.8	5.6±0.5	0.50	0.45±0.04
Alq ₃	16.8±0.5	1.8±0.2	0.45	0.35±0.08



Suppl. Figure 3.3: X-ray reflectivity comparison of the experimental data with the three used simulation models of the inorganic/organic multilayer stack.

Suppl. Figure 3.3 shows the XRR measurement of the organic/inorganic multilayer stack with the three different simulation models. The intensity of the reflectivity data is now shown in Intensity * q_z^4 to enhance the visibility of the Kiessig fringes and to distinguish between the fitting models.



Suppl. Figure 3.4: X-ray reflectivity fit of the Si/SiO₂/Ag stack

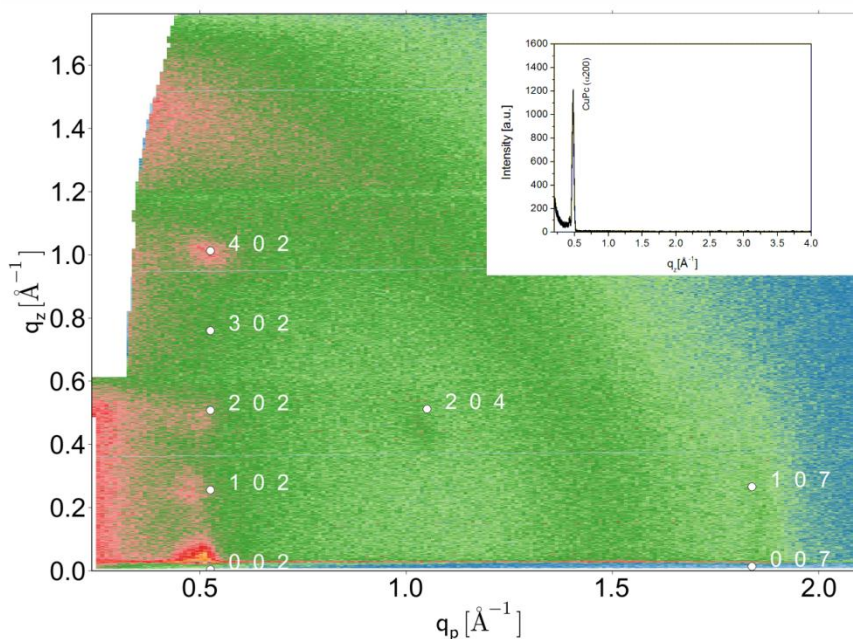
3.7.1 Not Published Information

Suppl. Figure 3.4 shows the top Ag layer on the silicon wafer and the extracted parameters were again used as a first guess for the whole multilayer fit. The fitting parameters of this arrangement are comprised in Suppl. Table 3.3.

Suppl. Table 3.3: XRR fit parameter of the Ag layer on Si/SiO₂. d_{XRR} denotes the measured thicknesses of the layers, σ_{XRR} describes the interface roughness and ρ_{XRR} denote the electron densities of the individual layer from XRR measurement. Additionally, the electron densities derived from the crystal structures (ρ_{crystal}) are given.

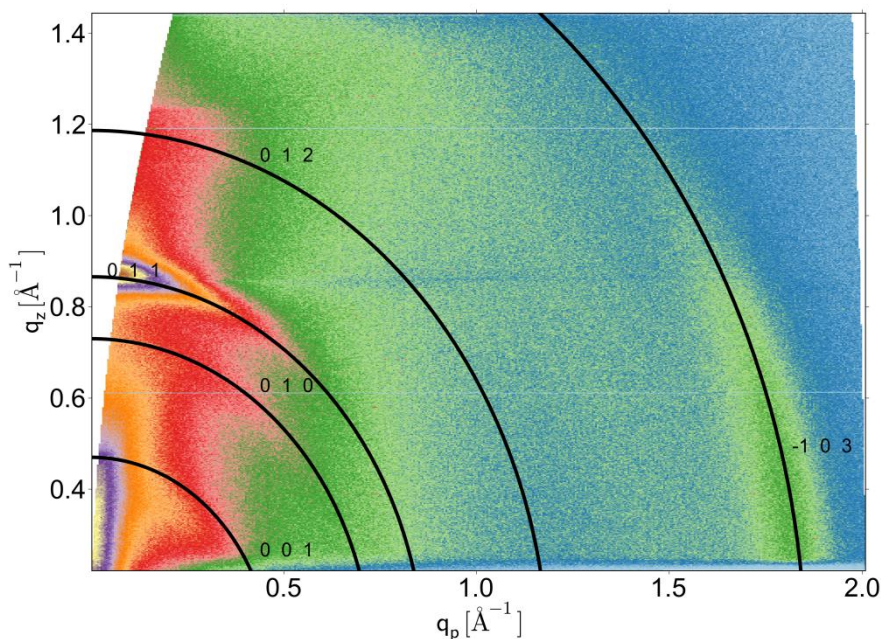
	$d_{\text{XRR}}(\text{nm})$	$\sigma_{\text{XRR}}(\text{nm})$	$\rho_{\text{crystal}}(1/\text{\AA}^{-3})$	$\rho_{\text{XRR}}(1/\text{\AA}^{-3})$
SiO ₂	101.5±2.1	0.25±0.1	0.67	0.67±0.01
Ag	59.5±0.5	2.5±0.4	2.76	2.73±0.03

The individual organic materials were deposited on Si/SiO₂ substrates and GIXD measurements were performed to get an insight into the crystallographic structure of each material. The substrate properties may influence the orientation of the crystallites, however the additional investigation supported the evaluation of the multilayer stack significantly (Moser *et al.* 2012). Each investigated film was deposited with the same deposition condition like in the organic multilayer stack.



Suppl. Figure 3.5: RSM of the CuPc film deposited on the Si/SiO₂ substrate. The inset gives the specular XRD of the film.

The Copper Phthalocyanine (CuPc) thin film was deposited on a silicon substrate and clearly shows a 2 dimensional powder with the crystallographic α -Phase (Suppl. Figure 3.5). The RSM of the thin film clearly shows diffraction features of the {h02} equivalent net planes as well as the 204, 007 and 107 Bragg peaks of CuPc. The inset of Suppl. Figure 3.5 gives the specular XRD data of the thin film, where only the 200 Bragg peak was observable, which clearly shows the crystallites are preferably orientated in the [100] direction on Si/SiO₂ substrate. A crystallite size of ~20 nm in the specular direction was determined by using the Scherrer equation (Scherrer 1918).



Suppl. Figure 3.6: RSM of the PTCBI film deposited on the Si/SiO₂ substrate. The inset gives the specular XRD of the film.

Perylene tetracarboxylic bisbenzimidazole (PTCBI) on the Si/SiO₂ substrate grows as three dimensional powder, which is demonstrated as ring like diffraction features in Suppl. Figure 3.6. The RSM comprises five diffraction rings; 001, 010, 011, 012 and -103 Bragg rings, which were indexed with the crystallographic solution described in chapter 1.4. The specular XRD measurement of the thin PTCBI film showed only one weak 011 diffraction feature, which was also observed along the specular direction in the RSM. Additionally, a crystallite size of ~5 nm was determined.

4 Diffusion of Ag into Organic Semiconducting Materials: A Combined Analytical Study Using Transmission Electron Microscopy and X-ray Reflectivity

Stefanie Fladischer^{1,}, Alfred Neuhold², Elke Kraker³, Thomas Haber¹, Bernhard Lamprecht³, Ingo Salzmann⁴, Roland Resel², and Werner Grogger¹*

1. Institute for Electron Microscopy and Fine Structure Research & Graz Centre for Electron Microscopy, Graz University of Technology, Graz, Austria
2. Institute of Solid State Physics, Graz University of Technology, Graz, Austria
3. Institute for Surface Technologies and Photonics, Joanneum Research Forschungsgesellschaft mbH, Weiz, Austria
4. Department of Physics, Humboldt-Universität zu Berlin, Berlin, Germany

4.1 Motivation

This study is a follow-up project of the previous described work (chapter 3) within ISOTEC cluster project. Here, the interface morphology of an organic/inorganic stack with optionally two structurally different organic semiconducting materials and a top silver layer were investigated. The top metal layer was deposited either by physical vapour deposition with different deposition rates, by electron beam deposition or by ion beam sputtering technique. The aim of this study was to structurally characterize the organic/metal interface by x-ray reflectivity analysis and by transmission electron microscopy and to probe the possible diffusion of metal clusters into the organic material. The contribution to this work was equally divided between Stefanie Fladischer and myself and the content of this manuscript will be submitted to a peer-reviewed journal by Stefanie Fladischer.

ABSTRACT. This study shows that the morphology of organic/metal interfaces strongly depends on process parameters and the involved materials. The interface between organic n-type blocking layer materials and the top Ag cathode within an organic photodiode was investigated. Ag was deposited on either amorphous tris-8-hydroxyquinolino-aluminium (Alq_3) or crystalline 4,7-diphenyl-1,10-phenanthroline (Bphen) using different deposition techniques such as electron beam deposition, ion beam sputtering and vacuum thermal evaporation at various deposition rates. The interfaces were studied by transmission electron microscopy and x-ray reflectivity. It was found that Bphen does not show any Ag diffusion no matter which deposition technique was used, whereas the Ag diffusion into Alq_3 depends on the deposition technique and the deposition rate. The highest amount of Ag diffusion into Alq_3 occurred by using thermal vacuum deposition at low deposition rates.

4.2 Introduction

The performance and efficiency of organic electronic devices depend on several aspects, such as intrinsic material properties and the interfaces between the different materials. Especially, the roughness of organic/metal interfaces and material diffusion distinctly influence the device performance. Furthermore, the influence of organic blocking layers introduced into device structures in combination with different deposition techniques of metal electrodes, e.g. Ag, are of particular importance.

For our present study on organic/metal interfaces an organic photodiode (OPD), which is used as detection unit in a sensor platform, was chosen as test device (Kraker *et al.* 2008; Lamprecht *et al.* 2010, 2011). The setup of this OPD is based on the well-known Tang photodiode (Tang 1986), consisting of stacked layers of copper phthalocyanine (CuPc as p-type material) and perylene tetracarboxylic bisbenzimidazole (PTCBI as n-type material). A thin Au layer was used as semitransparent bottom electrode and an opaque Ag layer was deposited as top electrode. Tris-8-hydroxyquinolino-aluminium (Alq₃, n-type material) and 4,7-diphenyl-1,10-phenanthroline (Bphen, n-type material) were introduced as additional layer between the organic stack and the cathode as such blocking layers are reported to improve the device performance (Song *et al.* 2005; Huang *et al.* 2006). The chemical structures of the respective molecules and the layout of the OPDs are depicted in Figure 4.1 together with a transmission electron microscopy (TEM) image of the cross-section of a representative OPD with Bphen as a blocking layer.

As organic/metal interfaces play an important role for the device performance, numerous studies on metal diffusion into organic layers have been carried out (Hirose *et al.* 1996) within which a variety of experimental techniques have been used including TEM (Faupel, Willecke, & Thran 1998; Dürr *et al.* 2003), x-ray reflectivity (Dürr *et al.* 2003), x-ray photoelectron spectroscopy (Song *et al.* 2001b; Turak *et al.* 2002; Wang *et al.* 2007), secondary ion-mass spectrometry (Song *et al.* 2001a; Grandin *et al.* 2003), radiotracer measurements (Faupel, Willecke, & Thran 1998; Scharnberg *et al.* 2005), and Rutherford backscattering (Faupel, Willecke, & Thran 1998; Dürr *et al.* 2003; Grandin *et al.* 2003). While some data on Ag diffusion into Alq₃ (Song *et al.* 2001a; Turak *et al.* 2002; Grandin *et al.* 2003) was already reported, to our knowledge, no study was carried out on Ag diffusion into Bphen yet. The above mentioned studies report conflicting results on Ag diffusion into Alq₃ including clear evidence that diffusion does occur (Song *et al.* 2001a; b) and the presence of well-defined interfaces without chemical reactions (Turak *et al.* 2002; Grandin *et al.* 2003).

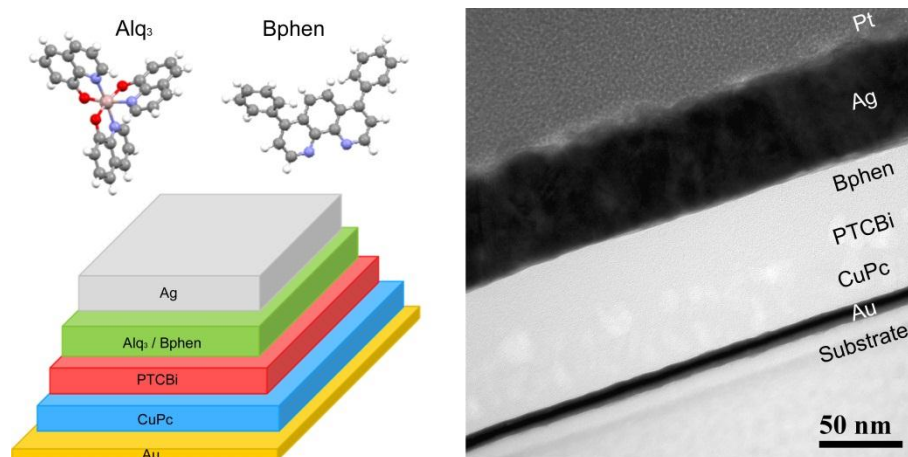


Figure 4.1: Chemical structure of tris-8-hydroxyquinolato-aluminium (Alq₃) and 4,7-diphenyl-1,10-phenanthroline (Bphen), layout and TEM cross-section image of the organic photodiode (Bphen used as a blocking layer, Ag electrode deposited by vacuum thermal evaporation).

In this study, we investigated Ag diffusion into both Alq₃ and Bphen with respect to different Ag deposition techniques such as electron beam deposition (EBD), ion beam sputtering (IBS) and vacuum thermal evaporation (VTE) at various deposition rates. The interfaces were characterized combining transmission electron microscopy (TEM), favoured for its high spatial resolution, and x-ray reflectivity (XRR) as bulk characterization tool, as outlined in chapter 3. Herewith, the dependence of interfacial parameters such as roughness and material diffusion on the fabrication procedure of the top Ag cathode was investigated. Finally, the findings for the interfaces were related to the device performances.

4.3 Experimental Details

Materials. For this study we fabricated OPDs and additional test structures comprising Alq₃ or Bphen layers with top Ag layers only. All samples were produced in a high-vacuum clustertool (Oerlikon Leybold Vacuum GmbH) including a metal deposition chamber (EBD, IBS and VTE) and an organic material deposition chamber (4 effusion cells). A transfer chamber connects the metal and the organic deposition chamber without breaking the vacuum during the whole sample fabrication procedure. All evaporated layers were thus prepared under high vacuum conditions (10^{-6} mbar) at room temperature by rotating the substrate to ensure homogeneous coating. The film thickness was triggered with a quartz thickness gauge.

For the OPDs microscope glass slides were used as substrates. For the semi-transparent anode a 6 nm Au layer was deposited by physical sputtering. The organic layer stack was formed by a 30 nm CuPc film (p-type semiconductor, purchased from Fluka), a 30 nm film of PTCBI (n-type semiconductor, purchased from Sensient Imaging Technologies GmbH) and 37 nm Alq₃ or Bphen (blocking layer, both purchased from Sigma Aldrich). As top-electrode an opaque Ag layer of 80 nm was deposited. Four different deposition techniques were used: electron beam deposition (EBD), ion beam sputtering (IBS) and vacuum thermal evaporation (VTE) with deposition rates of 0.02 nm/s and 0.3 nm/s. To provide reproducibility for the current to voltage characteristic measurements, every OPD configuration differing in the organic material and/or the Ag deposition technique was fabricated 6 times.

Samples for studying the interfaces were deposited on silicon wafers with 150 nm thermally oxidized SiO₂ (from Siegert Consulting e.K.). The organic blocking layer materials Alq₃ and Bphen were deposited with a nominal film thickness of 40 nm. For these samples a 20 nm thin Ag layer was chosen enabling accurate XRR measurements. For each organic/Ag configuration two samples, one for TEM and one for XRR investigations, were produced simultaneously to guarantee their equality. Ag deposition using VTE was performed at different deposition rates, 0.02 nm/s, 0.1 nm/s, 0.5 nm/s and 1 nm/s. The deposition rates for EBD and IBS were 0.03 nm/s and 0.7 nm/s respectively.

Methods. Current to voltage (I-V) characteristics of the OPDs were determined using a 150 W EKE halogen lamp. The light was launched into a fibreoptic cable and led to a single backlight, which had an area of 2'' x 2'' and was positioned under a glass window. The samples were placed on the glass window and contacted from the top with contact needles. The I-V characteristic was measured using an MB1020 parameter analyzer from mb-technologies. Additionally, the measurement desk was equipped with an opaque shield to block ambient light during the measurements.

For TEM investigations cross-section samples were made using a focused ion beam (FIB) instrument. The in situ lift-out technique (Langford & Clinton 2004) was chosen to realize homogeneously thin cross-section lamellas. To protect the surface from beam damage Pt layers were grown in the FIB by electron-beam induced deposition followed by ion-beam assisted deposition. To avoid artificial ion beam induced Ag diffusion into the organic materials upside down milling was used. To prevent Ag from degradation in ambient air TEM investigations were done immediately after preparing the lamella. For the TEM

investigations an FEI Tecnai F20 (S)TEM with a Schottky field emission gun (FEG) operated at 200 kV equipped with a high resolution Gatan Imaging Filter (GIF) and a Sapphire Si(Li) detector for energy dispersive x-ray spectrometry was used. To elucidate the interfaces TEM bright field (BF) and high angle annular dark field (HAADF) imaging techniques were chosen.

XRR measurements were performed on a Panalytical Empyrean Reflectometer setup with a $1/32^\circ$ primary slit (vertical limitation), a 10 mm beam mask (horizontal limitation) and a multilayer mirror on the primary side using Cu-K α radiation ($\lambda = 0.154$ nm). A small receiving slit of 0.1 mm and a PANalytical PIXCEL^{3D} detector were used at the secondary side. The X'Pert Reflectivity 1.3 software package was used to simulate the experimental data, which uses the Parratt formalism (Parratt 1954). In addition, this software package comprises a genetic fitting algorithm (Dane *et al.* 1998), which finds the vicinity of the global optimum of the fit and uses the Marquardt-Levenberg algorithm to finally optimize the parameters according to the local minimum. The surface roughness and the interface roughness were determined using the Névot and Croce approach (Croce & Névot 1976). The results of the XRR measurements are presented using the out-of-plane (q_z) component of the scattering vector \mathbf{q} as the abscissa.

Grazing incidence x-ray diffraction (GIXD) was measured to probe the crystallographic structure of the organic layers. The measurements were performed at the beamline W1 of the synchrotron radiation source HASYLAB (DESY, Hamburg, Germany) using a wavelength of 0.118 nm. The incidence angle of the x-ray beam was set to $\alpha_i = 0.15^\circ$ and the diffracted beam was measured with a one-dimensional MYTHEN II detector. The results are presented as integrated intensities of the reciprocal space map as a function of the in-plane component q_p of the scattering vector \mathbf{q} .

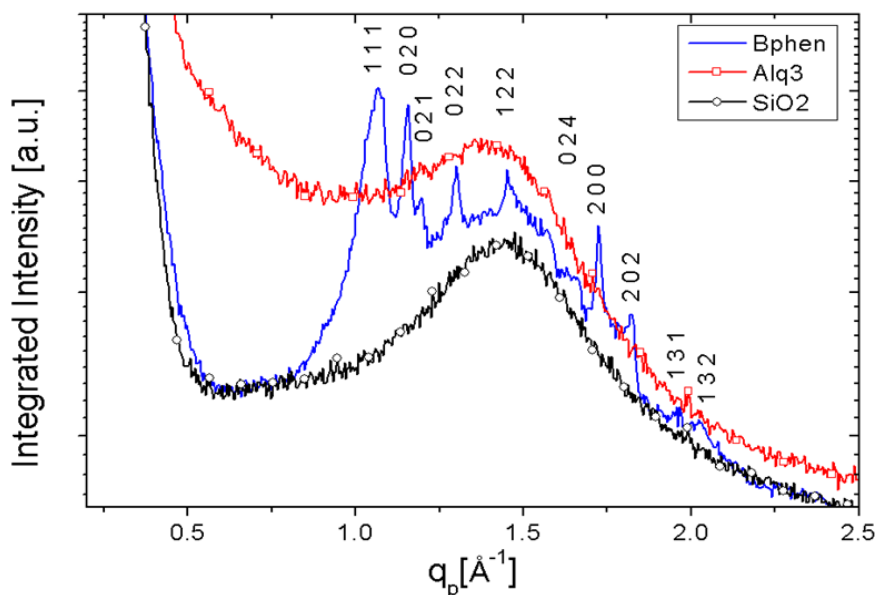


Figure 4.2: Intensity of the reciprocal space map (integrated along q_z) as a function of the in-plane component of the scattering vector (q_p) from GIXD. Black curve: amorphous SiO_2 substrate; red curve: amorphous Alq_3 layer; blue curve: crystalline Bphen layer with the corresponding Miller indexes.

4.4 Results and Discussion

The OPDs were characterized by I-V measurements to gain insight into the electrical behaviour and the performance of the devices, TEM and XRR investigations were performed to structurally characterize the organic/metal interfaces, and GIXD was carried out on the Alq_3 and Bphen blocking layers to determine their crystallographic structure. Figure 4.2 depicts linescans extracted from individual reciprocal space maps integrated up to 0.65 \AA^{-1} along the out-of-plane component of the scattering vector (q_z) of the pristine SiO_2 substrate (black curve), the Alq_3 layer (red curve) and the Bphen layer (blue curve) as a function of the in-plane component of the scattering vector (q_p). SiO_2 was used as substrate for both organic materials due to its low surface roughness ideal for GIXD. Our data clearly evidence amorphous growth of Alq_3 on the amorphous SiO_2 substrate and, in contrast, crystalline growth of Bphen. The Bphen diffraction peaks were indexed by the unit cell parameters published recently by Li et al. (Li, Brédas, & Lennartz 2007).

The investigated organic photodiodes are used as detection unit in opto-chemical sensor applications. Such integrated sensor OPDs are used to quantify changes of light corresponding to different kinds of gas concentrations as described in (Lamprecht *et al.* 2011). Note that a high ON/OFF ratio (ON: photodiode current under illumination, OFF: dark current) of the corresponding OPDs is essential to reach a high

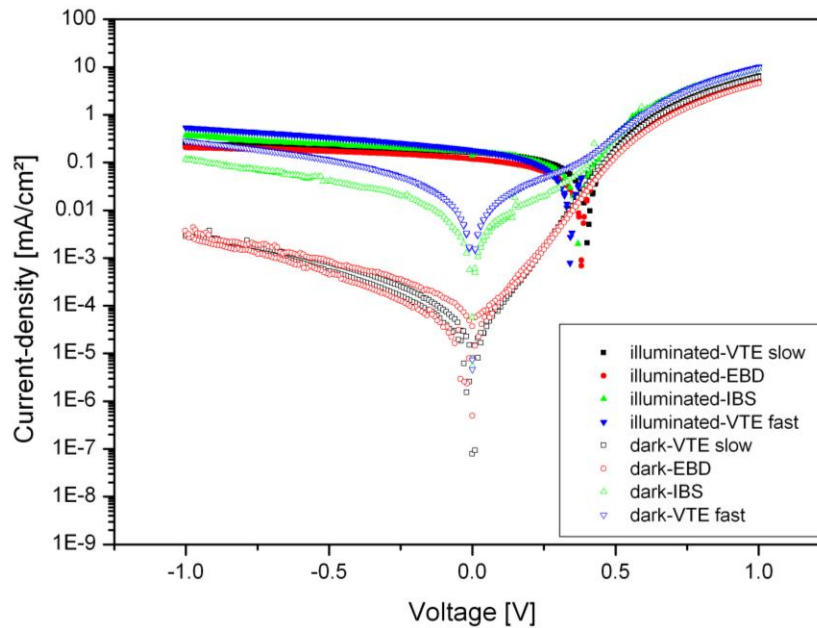


Figure 4.3: Current-density vs. voltage characteristics of organic photodiodes using Bphen as blocking layer under illumination (10 mW/cm^2) and in dark. The Ag electrodes were produced by vacuum thermal evaporation (VTE), electron beam deposition (EBD), and ion beam sputtering (IBS).

resolution of the sensor. ON/OFF ratios (measured at 0 V) of more than 10^3 are necessary for reliable sensor performance.

The I-V characteristics of the investigated OPDs showed (i), that the two organic blocking layer materials lead to different device performances and, (ii), that the different Ag deposition techniques significantly impact the I-V characteristics. Figure 4.3 depicts representative I-V characteristics in dark and under white light illumination for the OPDs using Bphen as blocking layer.

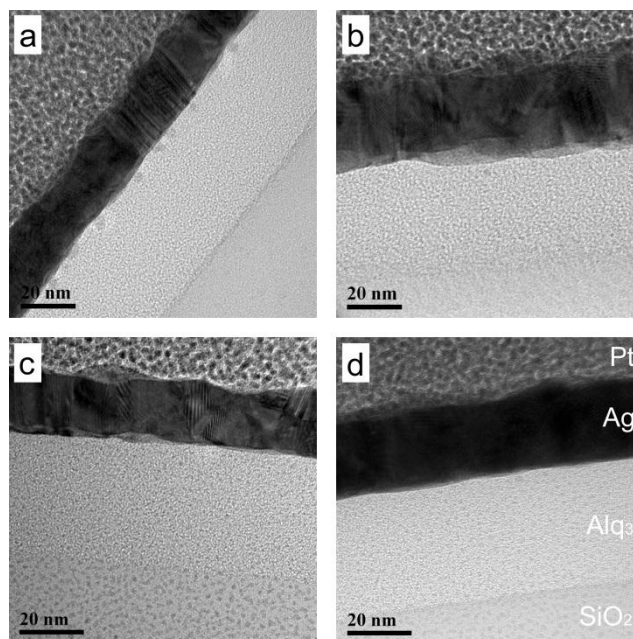


Figure 4.4: TEM cross-section images of the SiO₂/Alq₃/Ag stack with an additional Pt protection layer. The Ag layers were deposited on Alq₃ by (a) vacuum thermal evaporation with a deposition rate of 0.02 nm/s and (b) 1 nm/s, by (c) electron beam deposition and (d) ion beam sputtering.

OPDs with Ag deposited slowly by VTE (Figure 4.3, black lines) reached the highest ON/OFF ratios of 10^5 , followed by EBD (red lines) yielding an ON/OFF ratio of 10^4 , while devices fabricated by IBS (green lines) and fast VTE (blue lines) only reached 10^2 .

For the TEM characterization of the present organic/metal interfaces BF imaging was performed to get spatially resolved information about the morphology of the different materials and their interfaces. Additionally, HAADF imaging was used to gain contrast between the organic materials and the Ag layer due to the dependence of electron scattering on the atomic number. For each specimen the interfaces were investigated over a range of 5 μm (i.e. width of lamella) and the presented images are representative for the whole lamella. In Figure 4.4 TEM cross-section images of the Alq₃/Ag stacks on Si/SiO₂ substrates using different Ag deposition techniques are shown. In all images the lowest layer is the SiO₂ substrate followed by Alq₃, Ag and the Pt protection layer. Figure 4.4 a) represents a specimen where Ag was deposited by VTE with the lowest investigated deposition rate of 0.02 nm/s. There, Ag diffusion into Alq₃ can clearly be observed by means of small Ag particles at the interface penetrating into the organic layer over a range of approximately 6 nm. Additional EDXS measurements proved these particles to be Ag.

Similar Ag diffusion to a smaller extent was detected for the samples where Ag was deposited by VTE with the highest investigated deposition rate of 1 nm/s (Figure 4.4 b).

Interestingly, the diffusion depth is essentially identical, whereas the amount of diffused Ag particles is significantly reduced. This clearly indicates that Ag deposition on Alq₃ using VTE induces Ag diffusion into the organic layer. Moreover, depending on the deposition rate Ag diffusion occurs to a varying extent: the lower the deposition rate the more Ag diffuses into Alq₃. Figure 4.4 c) and d) display the specimens with Ag top layers deposited by EBD and IBS, respectively. In both cases no Ag particles penetrating into Alq₃ were observed. Therefore, obviously, Ag diffusion into Alq₃ can be minimized by choosing EBD or IBS as Ag deposition technique. Figure 4.5 shows TEM cross-section images of the Bphen/Ag stacks on Si/SiO₂ substrates using different Ag deposition techniques. The images show the same assembly as shown in Figure 4.4 for Alq₃ with Bphen instead. Figure 4.5 a) and b) show Ag deposited by VTE at deposition rates of 0.02nm/s and 1nm/s, respectively. Figure 4.5 c) displays Ag deposited by EBD and d) shows IBS deposited Ag. In the case of Bphen no Ag diffusion was observed, irrespective of both deposition technique and rate. Furthermore, comparing the interfaces of the two organic materials to Ag it is evident that, the interface of Bphen to Ag is significantly more defined than that of Alq₃.

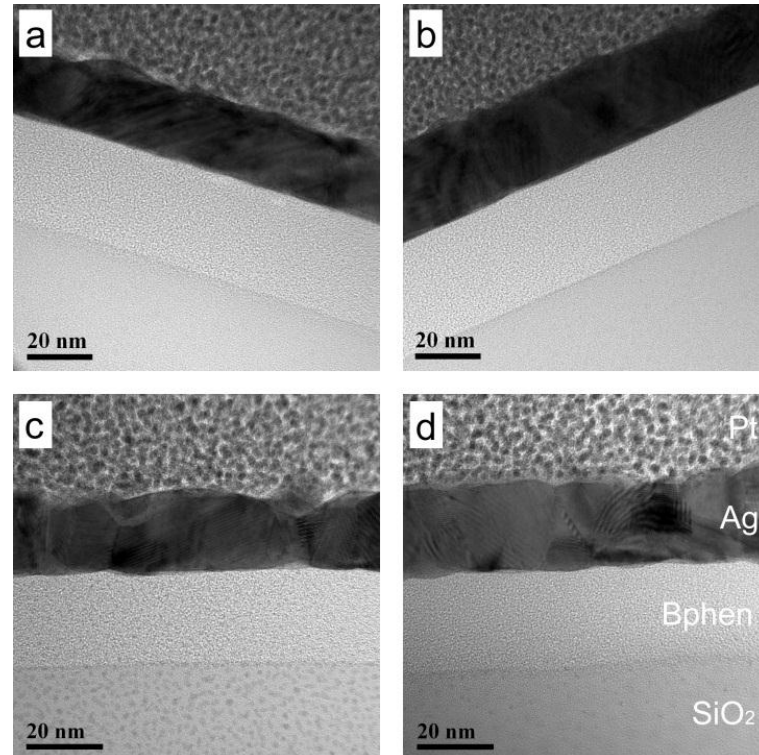


Figure 4.5: TEM cross-section images of the SiO₂/Bphen/Ag stack with an additional Pt protection layer. The Ag layers were deposited on Bphen by (a) vacuum thermal evaporation with a deposition rate of 0.02 nm/s and (b) 1 nm/s, by (c) electron beam deposition and (d) ion beam sputtering.

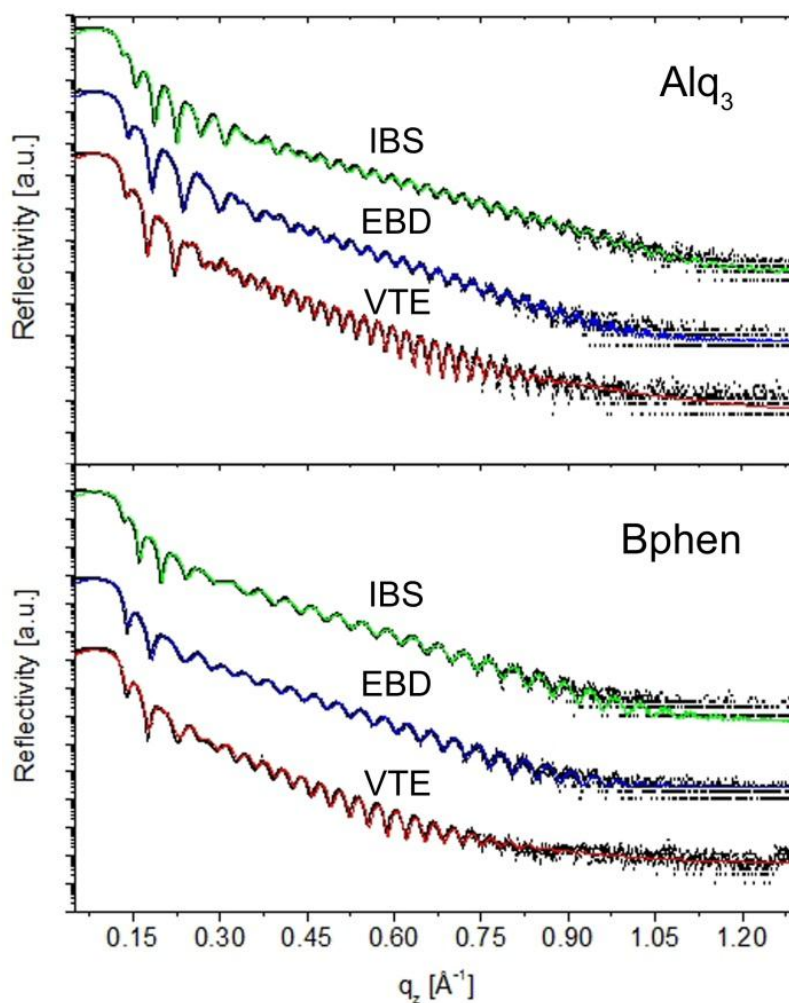


Figure 4.6: XRR measurements (black dots) and simulated data (full lines) of the Si/SiO₂/Alq₃/Ag and the Si/SiO₂/Bphen/Ag stacks. The figures compare samples with Ag layers deposited by ion beam sputtering (IBS, green line), electron beam deposition (EBD, blue line) and vacuum thermal evaporation (VTE, red line, deposition rate 0.02 nm/s).

XRR measurements were performed to obtain information on layer thickness, interface roughness and electron density of the respective layers. Figure 4.6 depicts the experimental XRR data (black dots) of the Si/SiO₂/Alq₃/Ag and Si/SiO₂/Bphen/Ag samples for different deposition techniques of the top Ag layer together with the corresponding simulations (lines). Note that in the case of Alq₃ the experimental data were simulated with an additional layer between Alq₃ and Ag to improve the quality of the fit, as without this layer, the minima of the Kiessig fringes could not be reasonably reproduced (Kiessig 1931). The parameters of this additional layer depend on the deposition technique as well as the deposition conditions. In Figure 4.7 the thickness and electron density of this additional layer are depicted. The rather thin additional layers (0.5 – 2.3 nm) exhibit increased electron densities compared to that of pure Alq₃ (0.42 Å⁻³). Its thickness in

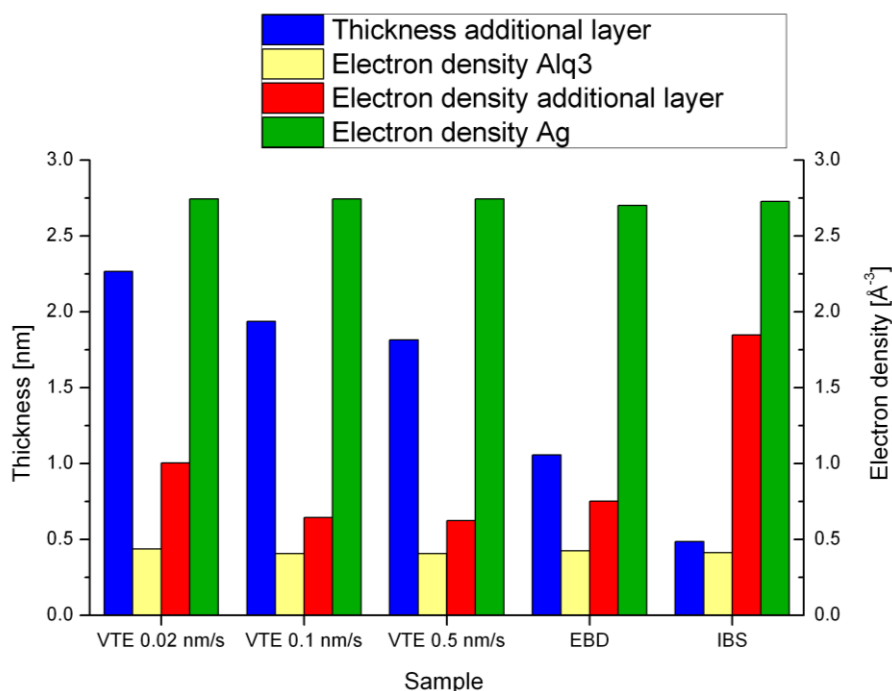


Figure 4.7: XRR fit results for the additional layer (diffusion layer) introduced between Alq₃ and Ag in the simulation. Its thickness and electron density are depicted together with the electron densities of Alq₃ and Ag for the different samples, where Ag is deposited by vacuum thermal evaporation (VTE) at various deposition rates (0.02 nm/s, 0.1 nm/s, 0.5 nm/s), electron beam deposition (EBD) and ion beam sputtering (IBS).

combination with its electron density can be interpreted in terms of diffusion depth and amount of diffused metal. The thickness of the diffusion layer is largest when the deposition rate is lowest and, therefore, decreases with increasing deposition rate, which is fully in-line with our TEM results. For EBD and IBS, where no Ag diffusion could be detected by TEM, the thickness of the additional layer, proposed for the XRR fit, is significantly lower (0.5 – 1 nm), which is in the range of the interface roughness (0.5 nm). In contrast to the Alq₃ multilayer stack, the simulations for Bphen could be properly performed without any diffusion layers, which points to a well-defined Bphen/Ag interface and no Ag diffusion into the subjacent organic material, which is, again, in good agreement with our TEM results. Note that, in comparison to Alq₃, Bphen possesses a smaller electron density (0.37 Å⁻³). Overall, the results of our TEM and XRR investigations are both qualitatively and quantitatively in good agreement and, hence, corroborate each other. From these results it becomes clear that Ag diffusion essentially depends on the nature of subjacent organic material. We attribute the different Ag diffusion behaviour into the two different organic materials to the degree of order within the organic layers: severe diffusion into amorphous Alq₃ and a well-defined organic/metal interface in case of crystalline

Bphen. Furthermore, the deposition technique has a substantial impact on the diffusion behavior and the interface morphology, which all is confirmed by the I-V characteristics.

4.5 Conclusion

First, this work shows that the combination of TEM and XRR represents a powerful nanoanalytical toolset perfectly suited for the characterization of organic electronic devices. The diffusion behaviour of Ag could be substantially elucidated: No Ag diffusion could be detected in the case of crystalline Bphen, whereas Ag diffusion of tuneable extent was observed for amorphous Alq₃. The extent of Ag diffusion into Alq₃ was evidenced to depend on both the deposition technique and the deposition rate. Ag deposited on Alq₃ using VTE induces Ag diffusion: the lower the deposition rate the more Ag diffuses into Alq₃. In contrast, no Ag diffusion was detected for Ag deposited by EBD and IBS. This Ag diffusion behaviour therefore seems to be dependent on the crystallinity of the organic materials (amorphous Alq₃, crystalline Bphen). Additionally, I-V characteristics confirm this material and deposition technique dependence. Clearly, to optimize the device performance, an appropriate deposition parameter set needs to be found for each individual material stack. In the present case, the most reliable production strategy consists of using Bphen in combination with Ag deposited by VTE with the lowest deposition rate for OPDs.

In summary, we demonstrated that Ag diffusion essentially depends on the structural properties of the subjacent organic material and that diffusion, in turn, can be minimized by choosing appropriate materials, deposition techniques, and preparation parameters. Both, the deposition technique used for the metallic layer and the nature of the organic blocking layer material significantly impact the performance of organic semiconducting devices.

4.6 Acknowledgement

Financial support by the “Austrian NANO Initiative” is kindly acknowledged (ISOTEC national cooperative RTD project 819718). We thank W. Caliebe (HASYLAB, DESY) for experimental support.

5 X-ray based tools for the investigation of buried interfaces in organic electronic devices

Alfred Neuhold[†], Hannes Brandner[†], Simon J. Ausserlechner[†], Stefan Lorbek[§], Markus Neuschitzer[†], Egbert Zojer[†], Christian Teichert[§], and Roland Resel[†]*

[†] Institute of Solid State Physics, Graz University of Technology, Petersgasse 16, 8010

Graz, Austria

[§] Institute of Physics, Montan University Leoben, 8700 Leoben

5.1 Motivation

This chapter shows a study on buried interfaces in an orthogonal soluble polymer stack involved into a bottom gate top contact thin film transistor arrangement. The organic semiconducting material was optionally dissolved in two different non-polar solvents, either toluene or chloroform and spin cast onto a water soluble polymer film. The aim of this study was to investigate the polymer/polymer interface morphology by x-ray reflectivity and show possible intermixing of the orthogonal soluble materials. The obtained XRR roughness parameters were crosschecked by atomic force microscopy investigations. In addition, in-house grazing incidence x-ray diffraction experiments were performed to probe the crystal structure of the multilayer stack. Finally the device performance of the thin film transistors was measured and related to the interface morphology of the multilayer device. This work will be submitted to the peer-reviewed journal *Organic Electronics*.

Abstract:

In this contribution we show that x-ray reflectivity combined with grazing incidence diffraction is a valuable tool for investigating organic multilayer structures that can be used in devices. We focus on a bilayer stack consisting of two materials (poly-(3-hexylthiophene) (P3HT) and poly-(4-styrenesulfonic acid) (PSSA)) spin cast from orthogonal solvents (water in the case of PSSA and chloroform or toluene for P3HT). X-ray reflectivity is used to determine the thickness of all involved layers as well as the roughness of the organic-organic hetero-interface and the P3HT surface. The latter is found to be consistent with the results of atomic force microscopy measurements. For the roughness of P3HT/ PSSA interface, we observe a strong dependence of the solvent used for P3HT deposition. The solvent also strongly impacts the texturing of the P3HT crystallites as revealed by grazing incidence diffraction. When applying the various PSSA/P3HT multilayers in organic thin-film transistors, we find an excellent correlation between the determined interface morphology and structure and the device performance.

5.2 Introduction

Knowledge about the interface morphology of an organic multilayer arrangement is crucial when intending to use such structures in electronic devices. This is because structural as well as morphological properties of interfaces can significantly impact the device performance. For instance, in organic solar cells, a rough interface between the semiconducting materials is preferable due to the improved probability of electron – hole separation at the donor/acceptor interface. In this context, Yan *et al.* used the resonant soft x-ray reflectivity technique to probe a polymer-polymer interface and subsequently correlated the morphology to the device performance of the solar cell (Yan *et al.* 2010). Also in organic light emitting diodes controlling the interface morphology is of relevance for improving the outcoupling efficiency and the internal quantum efficiency (Riedel *et al.* 2010).

In organic thin film transistors (OTFTs) a smooth dielectric/semiconductor interface is beneficial, as there the charge transport occurs mostly in the first few monolayers of the semiconducting material close to the dielectric (Yoon *et al.* 2006; Shao *et al.* 2011). Previous studies demonstrated a device performance enhancement by insertion of an additional modification layer or passivation layer into the device architecture (Salleo *et al.* 2002; Wu, Liu, & Ong 2006). This modification layer creates a threshold voltage shifts or enhances the charge carrier mobility, which was concluded to modifications of the interface morphology and the crystallographic order within the semiconducting materials (Pacher *et al.* 2008; Possanner *et al.* 2009; Marchl *et al.* 2010; Gholamrezaie *et al.* 2012)

One possible way to realize multilayer structures is the deposition of polymer layers on top of each other from orthogonal solvents. This approach has been used in the literature to improve the recombination efficiency in organic light-emitting devices (You *et al.* 2009; Sax *et al.* 2010; Yook & Lee 2011). Here a large variety of structures can be envisioned, e.g., by ink-jet printing of orthogonally soluble polymers on top of each other (Huang *et al.* 2008; Zhong *et al.* 2011; Baeg 2011).

Such multilayer stacks naturally contain buried interfaces, whose non-destructive characterisation is difficult. Here x-ray reflectivity (XRR) (Gibaud & Hazra 2000) can become a highly useful tool, as besides providing information on the average thickness of the various layers, it also allows a characterization of the surface and, most importantly, the buried organic/organic and organic/inorganic hetero-interfaces (Hammer *et al.* 2010; Neuhold *et al.* 2011; Fladischer *et al.* 2012). Combining XRR with grazing incidence x-ray

diffraction (GIXD) (Vineyard 1982) additionally allows simultaneously studying the often interface-induced thin-film structure and texturing (Wedl *et al.* 2012; Moser *et al.* 2012).

To demonstrate the potential of the combination of those techniques, we have investigated double-layer structures consisting of the water-soluble poly (4-styrenesulfonic acid) (PSSA) onto which poly-(3-hexylthiophene) (P3HT) is spin-cast either from chloroform (CHCl_3) or toluene (C_7H_8). The choice of the latter is motivated by it being a classical organic semiconductor material used in solar cells and OTFTs. Its measured charge-carrier mobility is reasonably large (typically between $0.01 - 0.1 \text{ cm}^2/\text{Vs}$), and massively impacted by the morphology and the crystallographic properties of the P3HT film (Joshi *et al.* 2008; Salleo *et al.* 2010; Brinkmann 2011). The latter is by molecular weight of the polymer chains (Kline *et al.* 2003; Zen *et al.* 2006; Yang *et al.* 2007), the deposition technique of the film (Salleo *et al.* 2002; Yang *et al.* 2007), the used P3HT solvent (Yang *et al.* 2007; Huang *et al.* 2008; Cheng, Lin, & Wu 2009; Zhong *et al.* 2011) or the annealing temperature of P3HT (Kanai *et al.* 2009). PSSA is primarily employed, as it can be spin-cast from water.

To benchmark the XRR results, the surface morphology of the top P3HT layer is additionally investigated by atomic force microscopy (AFM) and to correlated interface morphology and P3HT texturing with charge transport properties, PSSA/P3HT bilayers are also included into bottom-gate top contact OTFT structures.

5.3 Experimental Section

5.3.1 Materials and Thin Film Preparation

Poly (4-styrenesulfonic acid) (PSSA) was purchased from Sigma Aldrich (CAS: 28210-41-5) and dissolved in deionized water with a concentration of 3.6 g/l. Regioregular-poly-(3-hexylthiophene) (P3HT) was purchased from BASF (Sepiolid P200 manufactured by BASF, CAS: 156074-98-5). According to the manufacturer it shows a head-to-tail regioregularity higher than 98% and a molecular weight of $\sim 30.000 \text{ g/mol}$. Both materials were used without further purification. For thin film preparation, the P3HT was dissolved either in the low boiling point solvent chloroform (short: P3HT (chloroform), $T_b = 61^\circ\text{C}$) with a concentration of 6 g/l or in the high boiling point solvent toluene (short P3HT (toluene), $T_b = 111^\circ\text{C}$) with a concentration

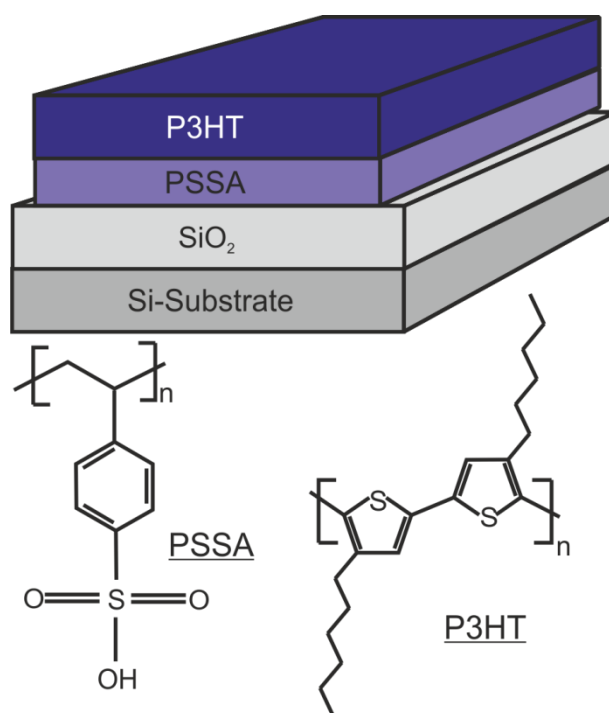


Figure 5.1: Multilayer structure of the investigated polymer stack on the Si/SiO₂ substrate together with the chemical structure of poly-(3-hexylthiophene) (P3HT) and poly(4-styrenesulfonic acid) (PSSA).

of 10 g/l. The different concentrations were chosen to realize a P3HT layer thickness of ~40 nm on top of the 8 nm thick PSSA layer. As substrates, doped Si – wafers (size: 20 mm x 20 mm), with a 150 nm thermally oxidized SiO₂ layer on top with a surface roughness of ~0.5 nm (as measured by XRR) were obtained from Siegart Consulting e.K. (Aachen, Germany). The substrate was chemically cleaned by RF O₂-plasma etching for 30 s immediately before deposition of the first layer. PSSA was then spin cast at 200 rpm for 15 s followed by 3500 rpm for 40 s onto the substrate under ambient conditions. The PSSA layer was further annealed at 80°C in high-vacuum for 2h to reduce residual water in the PSSA layer. The subsequent spin casting of P3HT was done in Argon atmosphere using a home-built spin-coater at ~1500 rpm for 40 s. Then the sample was annealed in Ar for 5 min at 80°C (i.e., above the glass transition temperature of P3HT at T_g=12.1°C (Zhao *et al.* 2009)) to avoid solvent residuals in the thin film (Werzer *et al.* 2007). Besides the multilayer stack also single polymer thin films were characterized in terms of their crystallographic properties and layer morphology (layer thickness, layer roughness and electron densities). Figure 5.1 shows the investigated polymer arrangement on the substrate with the chemical structure of the two polymer materials.

5.3.2 Structural Investigations

Specular x-ray reflectivity measurements were performed on a Panalytical Empyrean Reflectometer equipped with an multilayer mirror and a $1/32^\circ$ slit on the primary side using Cu K_α radiation ($\lambda = 0.154$ nm). A small receiving slit of 0.1 mm and a PANalytical PIXCEL^{3D} detector (used as a point detector) were used on the secondary side. The experimental data were simulated with the X'Pert Reflectivity 1.3 software (PANalytical) (Dane *et al.* 1998), which uses the Parratt formalism to simulate the data (Parratt 1954). The errors are from statistical origin and are related to the numerical error of the fitting parameters (Press *et al.* 2007). The surface roughness and the interface roughness of the specimen were determined using the Croce and Névot approach (Croce & Névot 1976).

Grazing incidence x-ray diffraction (GIXD) measurements were performed with a commercial four-circle Bruker D8 Discover diffractometer upgraded with the Bruker Ultra GID add-on and a sealed copper tube ($\lambda = 0.154$ nm). The incidence angle ($\alpha_i=0.17^\circ$) of the primary beam was optimized to maximize the scattering intensity from the sample and the beam height finally was set by a 0.6 mm slit (Neuschitzer *et al.* 2012). The results of in-plane GIXD measurements are presented in the form of integrated intensities along the q_z direction ($q_z = 0.2 - 3$ nm⁻¹) with respect to the in-plane component q_p of the scattering vector q extracted from reciprocal space maps (Moser *et al.* 2009).

The atomic force microscopy (AFM) measurements were performed with a MFP 3D system of Asylum Research in tapping mode under ambient conditions. As probes, NSG30 cantilevers from NT-MDT with a force constant of about 40 N/m, a resonance frequency of about 300 kHz, a tip radius of around 10 nm and an opening angle at the apex of about 10° were used. The images were processed afterwards with the free data analysis software Gwyddion (Nečas & Klapetek 2012). For the characterization of the surface roughness, the one dimensional height-height correlation function (HHCF) was calculated along the fast scan axis, x , of the images and then averaged over all scan lines. Because of the self-affinity of the surfaces, the HHCF was fitted with (Zhao, Wang, & Lu 2001b),

$$C(x) = \sigma^2 e^{-\left(\frac{x}{\xi}\right)^{2\alpha}} \quad (5.1)$$

to obtain the three main roughness parameters, that are (i) the root mean square (r.m.s.) roughness σ , (ii) the lateral correlation length ξ , and (iii) the Hurst parameter α . The latter parameter describes how jagged the layer surface is formed (Zhao, Wang, & Lu 2001).

5.3.3 Device Fabrication

For device characterization, ~50-nm-thick gold source and drain electrodes were deposited on top of the polymer stack by a shadow mask in a high-vacuum set-up operated inside an Ar glove-box. The resulting channel length and width were 25 μm and 7 μm , respectively. The devices were characterized in the glove box with a Keithley KE2623A and the data was evaluated with a home-made software package. The mobility of the investigated polymer transistors were extracted in the saturation regime neglecting the impact of the contacts and the dependence of the mobility on the gate-voltage. Due to that and the often considerable hysteresis (vide infra), we will in the future always refer to effective mobilities. The device characteristics were measured for two simultaneously prepared sets of samples, each of which contained 4 working bottom gate-top contact transistors, yielding consistent results.

5.4 Results and Discussion

5.4.1 XRR and AFM Results

Individual organic layers on Si/SiO₂: In order to investigate a complex multilayer system by XRR analysis, it is beneficial to first characterize the individual layers on a substrate. Hence, each organic material was dissolved in the desired solvent and spin cast onto the silicon oxide substrate. The preparation condition was maintained for all following test samples as well as for the devices. Figure 5.2 shows the reflectivity data (left) of the PSSA(water) layer on the substrate and the corresponding AFM image (right) of the same sample. The variations of the reflectivity with the large period originate from the PSSA layer. The thickness of that layer is extracted from the XRR fit (red line) to be 8.9 ± 0.1 nm. The superimposed rapid oscillations are due to the SiO₂ layer, whose thickness is determined to be 147.2 ± 3.5 nm thick SiO₂ layer. The fitted surface roughness of the PSSA layer is 0.3 ± 0.1 nm and the PSSA layer comprises an electron density of 414 ± 31 nm⁻³. From the fit the roughness of the SiO₂/PSSA interface is determined to be 0.4 ± 0.1 nm. The AFM surface morphology investigations on the same sample confirm the assessment from the XRR data that the PSSA surface is very smooth. The extracted r.m.s. surface roughness of 0.12 ± 0.02 nm is in reasonable agreement with the XRR data with a lateral correlation length of 99 ± 34 nm and a Hurst parameter of 0.6 ± 0.1 .

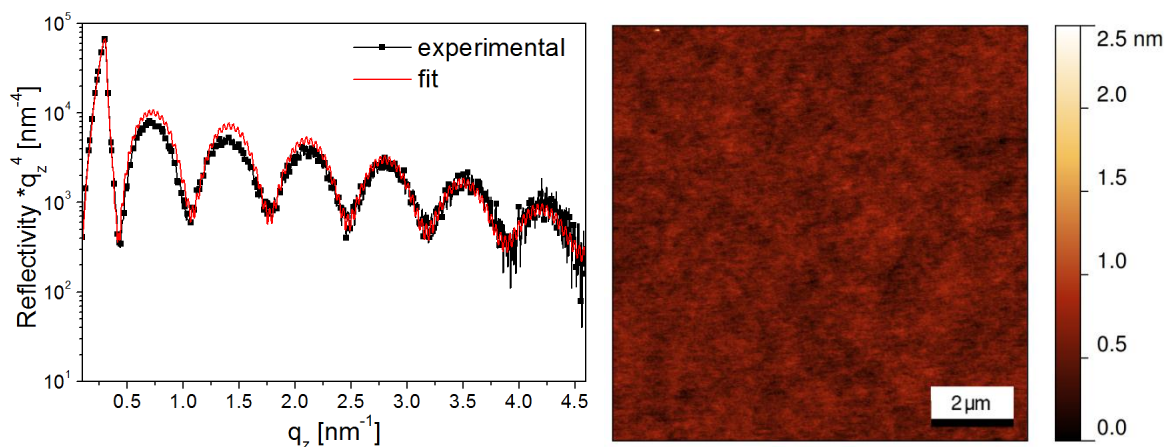


Figure 5.2: The left graph shows the x-ray reflectivity (square) of the Si/SiO₂/PSSA-stack as a function of the scattering vector q_z . The red lines is the corresponding XRR fit. The right AFM image shows the morphology of the PSSA layer on top of the silicon oxide

Furthermore, single layer investigations on P3HT layers spin-cast from two different solvents were performed. The top XRR graph in Figure 5.3 shows the result for the P3HT layer prepared from toluene and the bottom XRR graph for that spin-cast from chloroform. Here, the rapid oscillations again correspond to the silicon oxide layer of the substrate. Interestingly, the graphs show completely different behaviour concerning the oscillations originating from the P3HT layers. The top curve for P3HT(toluene) comprises only few oscillations descending, while the bottom curve for the P3HT(chloroform) sample shows many well pronounced interference fringes. This is not a consequence of different layer thicknesses, as the XRR fits (red lines) reveal essentially the same layer thicknesses for both samples (cf., Table 5.1). Instead the extracted surface roughnesses are significantly different, where the three times larger surface roughness for the film cast from toluene (cf., Table 5.1) causes the slow reflectivity variations to vanish at large q . Both XRR simulations additionally comprise the interface roughness between SiO₂ and P3HT with a roughness value of 0.4 ± 0.1 nm. AFM morphology investigations on the same samples show a similar relative increase of the surface roughness compared to the PSSA layer and also confirm the clearly larger surface roughness for the P3HT film cast from the high boiling-point solvent toluene (Table 5.1 and top AFM image of Figure 5.3). The AFM image of the P3HT film cast from chloroform comprises a serrated superlattice with a roughness of 6.37 ± 1.64 nm ($\xi = 163 \pm 26$ nm, $\alpha = 0.8 \pm 0.1$) (bottom AFM image of Figure 5.3). Neglecting these isolated spikes, the r.m.s. roughness gets significantly smaller to 1.3 nm on a laterally shorter correlation length of 72 ± 2 nm, which then gives comparable results to the XRR investigations (Table 5.1).

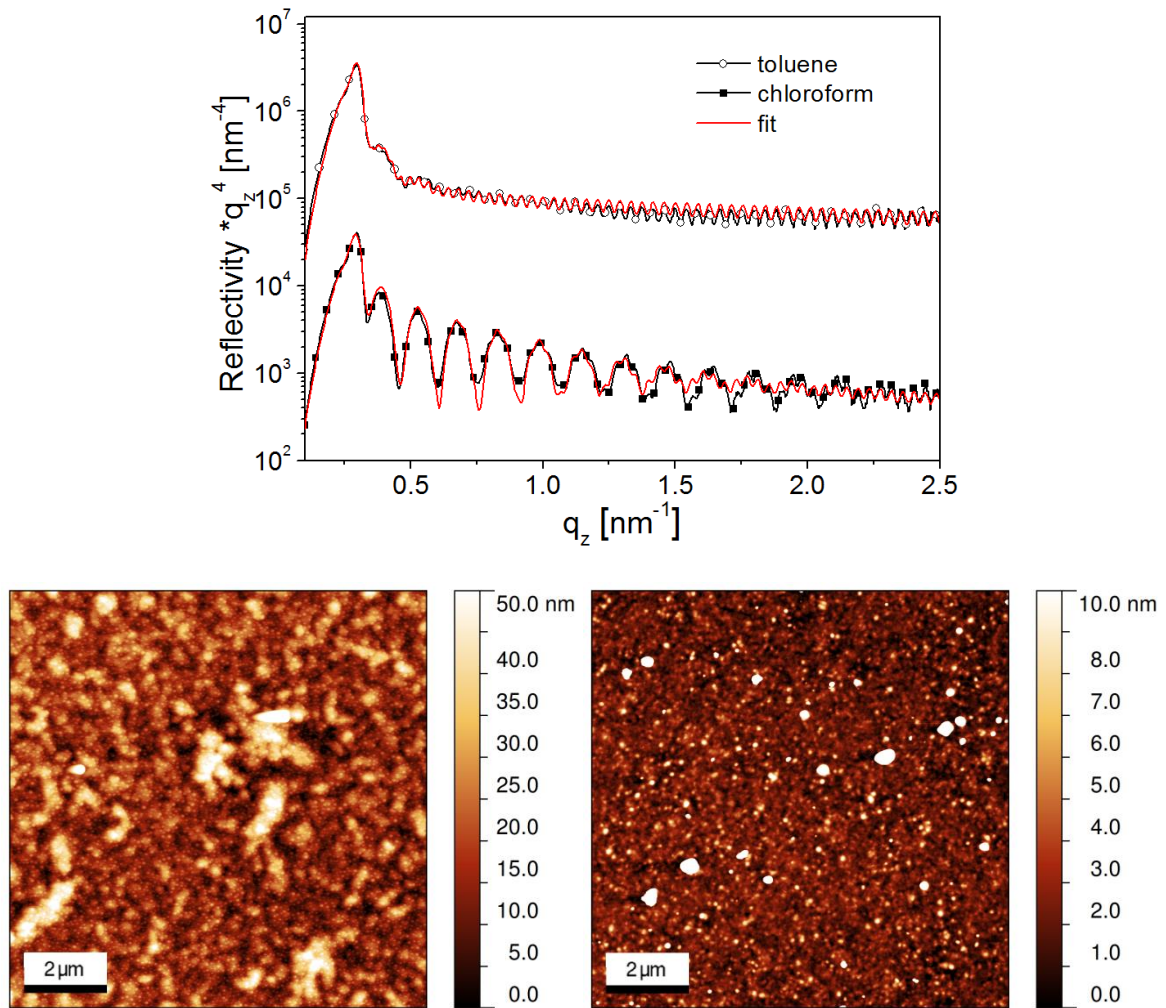


Figure 5.3: The top plot shows the x-ray reflectivity for the Si/SiO₂/P3HT-stacks as a function of the scattering vector q_z . The upper line illustrates the stack with the P3HT layer prepared from toluene (open circles) and the lower curve the P3HT layer prepared from chloroform (filled squares). The red lines are the corresponding fits. The data for P3HT toluene are shifted by 10^3 nm^{-4} for the sake of clarity; only every tenth data point is designated by a circle/square. The left AFM image shows the P3HT(toluene) morphology and the right AFM image that for P3HT (chloroform).

Table 5.1: Layer thickness d , r.m.s. roughness σ and total electron density ρ of the investigated multilayer stacks extracted from the XRR data shown in Figure 5.3 (top) and surface roughness σ , lateral correlation length ξ and Hurst parameter α obtained from AFM

Sample	XRR			AFM		
	d [nm]	σ_{surface} [nm]	ρ [nm^{-3}]	σ_{surface} [nm]	ξ [nm]	α
SiO ₂ /P3HT(C ₇ H ₈)	38.5 ± 0.5	5.3 ± 0.5	376 ± 21	10.4 ± 2.0	224 ± 38	0.8 ± 0.1
SiO ₂ /P3HT(CHCl ₃)	39.0 ± 0.1	1.6 ± 0.4	357 ± 21	1.3 ± 0.1	72 ± 2	0.9 ± 0.1

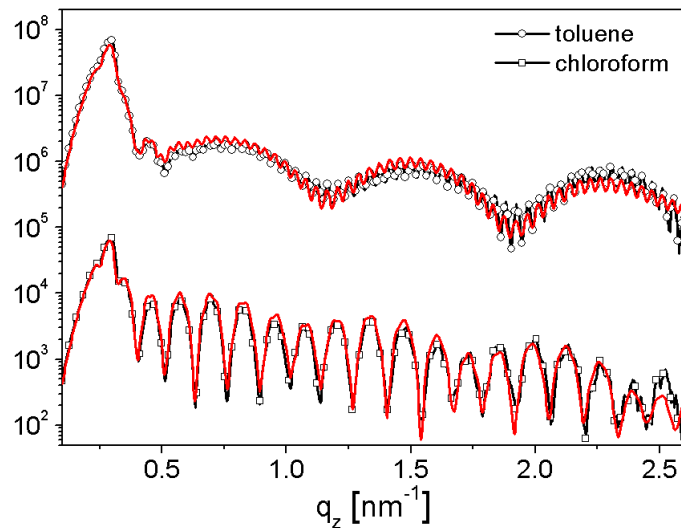


Figure 5.4: X-ray reflectivity of the SiO₂/PSSA/P3HT-stacks as a function of the scattering vector q_z . The upper line illustrates the stack with P3HT prepared from toluene (open circles) and the lower curve is for P3HT dissolved in chloroform (filled squares). The red lines are the corresponding fits. The data for P3HT (toluene) were shifted by 10^3 nm^{-4} for the sake of clarity; only every tenth data point is designated by a circle/square.

Table 5.2: Layer thickness d , r.m.s. roughness σ and total electron density ρ of the investigated multilayer stacks extracted from the XRR data shown in Figure 5.4. The corresponding materials – PSSA and P3HT – are given as subscripts

Sample	d_{PSSA} [nm]	$\sigma_{\text{Interface}}$ [nm]	ρ_{PSSA} [nm ⁻³]	d_{P3HT} [nm]	σ_{surface} [nm]	ρ_{P3HT} [nm ⁻³]
PSSA (water)/P3HT(C ₇ H ₈)	8.1±0.5	0.2±0.1	410±10	39.9±0.5	4.7±0.5	375±017
PSSA(water)/P3HT(CHCl ₃)	8.5±0.5	1.2±0.3	414±12	39.1±0.9	0.9±0.2	367±19

Multilayer stacks: With the properties of the individual layers known, next the morphological properties of the multilayer stacks shall be discussed. These consist of the water soluble PSSA layer on top of the Si/SiO₂ substrate onto which P3HT is spin-cast either from toluene or from chloroform. The corresponding XRR data together with the fits are shown in Figure 5.4 and the parameters extracted from the fits are summarized in Table 5.2. The fast oscillations in both characteristics again originate from interference at the SiO₂. The other oscillations in the XRR fits arise from the 39.9±0.5 nm thick P3HT (toluene) layer on top of the 8.1±0.5 nm thick PSSA layer of the first investigated specimen and a 39.1±0.9 nm thick P3HT (chloroform) layer on top of an 8.5±0.5 nm thick PSSA layer in the second investigated multilayer system. The individual layer thicknesses agree well with the thicknesses of single layer investigations.

Again the oscillations due to the P3HT layer decay rapidly with q for the sample cast from toluene. This is fully consistent with the larger surface roughness of the P3HT(toluene) film extracted from the fits ($\sigma_{\text{rms}} = 4.7 \pm 0.5$ nm for P3HT(toluene) vs. $\sigma_{\text{rms}} = 0.9 \pm 0.2$ nm for P3HT(chloroform)). In that sample, however, the oscillations due to interference at the PSSA layer are much better preserved at large q than for the film cast from chloroform. Also this observation has to be related to an interface roughness, but in this case to the roughness of the interface between the PSSA and the P3HT layer as the latter determines the interference at the PSSA film. Indeed, as expected, the fits reveals a significantly larger roughness of the buried PSSA/P3HT interface for the P3HT(chloroform) sample ($\sigma_{\text{rms}} = 1.2 \pm 0.3$ nm) than for the stack containing the P3HT(toluene) stack ($\sigma_{\text{rms}} = 0.2 \pm 0.1$ nm). I.e., when using the high boiling point solvent toluene a larger surface but smaller interface roughness is obtained than when using chloroform. This can be explained by the significantly longer time it takes for toluene layer to dry allowing for significant rearrangements of the P3HT chains at the surface. The more polar chloroform, on the other hand, can be expected to at least swell the PSSA layer when spin-casting P3HT resulting in a larger roughness of the buried PSSA/P3HT interface.

To obtain an independent second set of results for the surface roughness, in Figure 5.5, AFM images of the samples are compiled with their HHCFs. For better statistics, independent $10 \times 10 \mu\text{m}^2$ AFM images of each sample were analysed. Table 5.3 shows the resulting average values and the standard deviations of the extracted roughness parameters. The AFM investigation showed that the r.m.s. roughness increased by a factor of 5 for the P3HT, dissolved in chloroform, on top of the PSSA layer, and by a factor of 70 for the pure PSSA film. The large lateral feature size in the P3HT(toluene) sample is reflected by an increased lateral correlation length to about 200 nm.

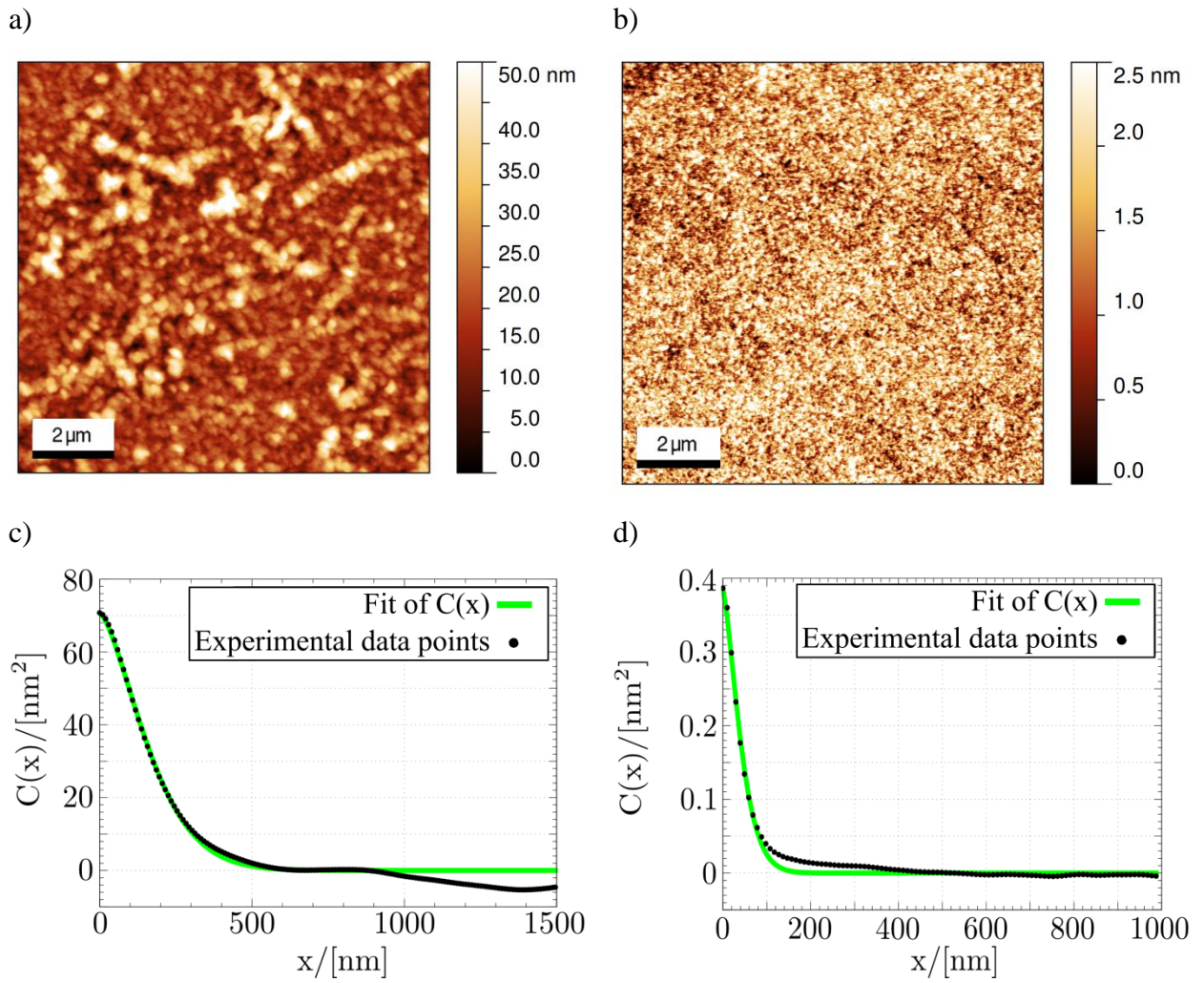


Figure 5.5: (a,b) $10 \times 10 \mu\text{m}^2$ AFM micrographs of Si/SiO₂/PSSA(water)/P3HT(toluene) and Si/SiO₂/PSSA(water)/P3HT(chloroform) samples. (c) is the height-height correlation function corresponding to the data from (a), and (d) that for the data from (b). The black dots reveal the experimental data and the full line is the fit using eq.(1).

Table 5.3: Mean values of the surface parameters (rms roughness σ , lateral correlation length ξ , Hurst parameter α , statistically calculated from a certain number of AFM images for each sample.

Sample	σ_{surface} [nm]	ξ [nm]	α
Si/SiO ₂ /PSSA(water)/P3HT(C ₇ H ₈)	8.4 ± 0.4	200 ± 4	0.8 ± 0.1
Si/SiO ₂ /PSSA(water)/P3HT(CHCl ₃)	0.6 ± 0.1	61 ± 15	0.7 ± 0.1

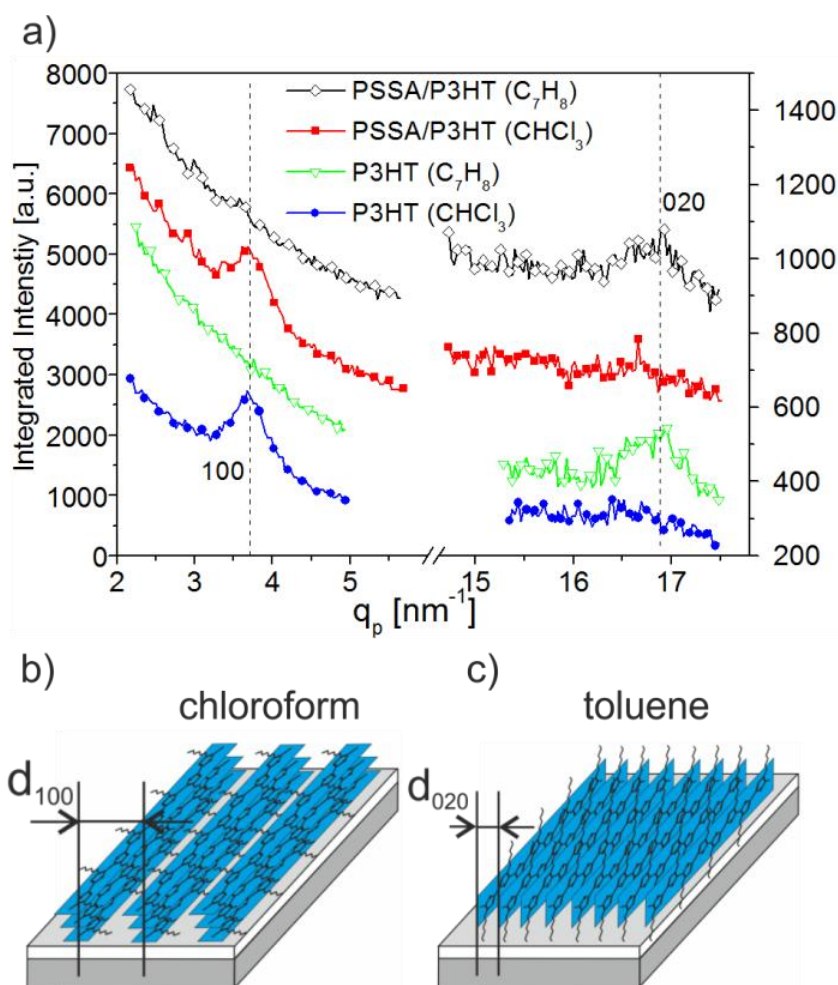


Figure 5.6: a) Integrated intensities along the q_z -direction of the investigated single layer P3HT and PSSA/P3HT multilayer samples with respect to the in-plane direction q_p of the scattering vector ($q_z = 0.2 - 3 \text{ nm}^{-1}$); b) sketch of the face-on alignment of the P3HT molecules prepared from chloroform solution and c) sketch of the edge-on alignment of the P3HT molecules prepared from toluene solution.

5.4.2 Grazing incidence X-ray diffraction results

Grazing incidence x-ray diffraction experiments were performed to get an insight to the preferred orientation of the molecules within the multilayer stacks. Figure 5.6 a) shows the integrated intensities as a function of the in-plane component of the scattering vector, q_p , extracted from the measured reciprocal space maps integrated over the out of plane component, q_z . Only diffraction features from P3HT were observed. Also single layer investigations reveal no crystallographic order of PSSA. For P3HT spin-cast on Si/SiO₂ from chloroform, only an onset of a ring-like diffraction feature at $q_p = 3.7 \text{ nm}^{-1}$ was observed (blue circles in Figure 5.6 a)). This feature corresponds to the d_{100} spacing of P3HT crystallites (Brinkmann 2011). Since the second frequently observed diffraction

feature at $q_p = 16.8 \text{ nm}^{-1}$ is missing (d_{020} spacing of P3HT crystallites), we conclude that the crystalline parts of P3HT consist mainly of crystallites with [010] orientation parallel to the sample surface. Figure 5.6 b) illustrates this alignment of the P3HT molecules on the sample, which is frequently denoted as face-on alignment. Interestingly, the arrangement of the P3HT crystallites in the thin film does not change for the P3HT layer deposited from chloroform onto the PSSA film (red rectangles in Figure 5.6 a)). In the GIXD measurements of the P3HT toluene layer deposited either onto the SiO_2 surface (green triangle) and onto the PSSA layer (black diamond) no diffraction feature from the (100) planes of the P3HT crystallites is observed. Instead, the second expected diffraction feature of P3HT at $q_p = 16.8 \text{ nm}^{-1}$ appears. This suggests a dominating [100] orientation of the P3HT crystallites also known as edge-on alignment (Figure 5.6 c)). This is consistent with the results of Chang et al., who demonstrated a preferred edge-on alignment of P3HT molecules dissolved in high boiling point solvents (Chang *et al.* 2004).

When performing specular x-ray diffraction scans of the PSSA/P3HT(toluene) multilayer stack clearly shows the specular 100 Bragg peak of P3HT at $q_z = 3.7 \text{ nm}^{-1}$, which is hardly visible in the multilayer stack prepared from chloroform (not shown). This is consistent with the above described alignment of the crystallites.

5.4.3 Device performance

To obtain a first impression, how the above-described structural and morphological parameters correlate with device performance, we fabricated a series of OTFTs containing the differently spin-cast P3HT layers. Representative transfer characteristics for these devices are shown in Figure 5.7, where the left graph refers to devices in which the P3HT layer has been deposited from toluene and the right graph to devices, where chloroform has been used as a solvent. The open, black squares refer to single layer devices and the filled, red squares to OTFTs containing PSSA/P3HT double layers. The main (effective) device parameters extracted from the transfer characteristics are summarized in Table 5.4.

Table 5.4: Main device parameters extracted from the saturation region of transfer characteristics of P3HT and PSSA/P3HT OTFTs spin-cast either from chloroform or toluene solution and measured at $V_D=-40$ V. The values are averaged over all investigated devices. The larger standard deviations for devices cast from chloroform is a manifestation of the larger scattering in the obtained data.

	$\mu_{\text{sat}} / 10^{-3} \text{ cm}^2/(\text{Vs})$	$V_{T,\text{sat}} / \text{V}$
Si/SiO ₂ /P3HT(toluene)	5.9 ± 0.9	15 ± 2
Si/SiO ₂ /PSSA/P3HT(toluene)	24.0 ± 2.0	1 ± 2
Si/SiO ₂ /P3HT(chloroform)	3.0 ± 2.0	2 ± 4
Si/SiO ₂ /PSSA/P3HT(chloroform)	0.6 ± 0.3	5 ± 5

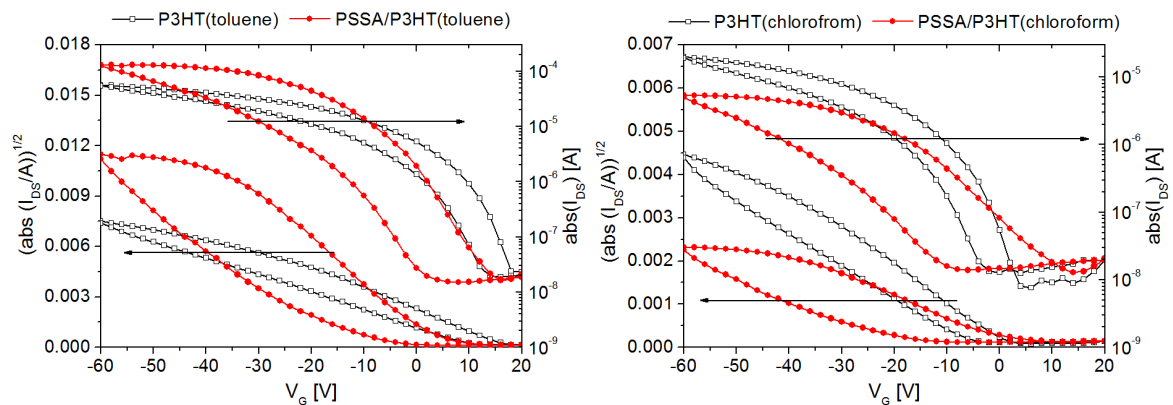


Figure 5.7: Representative transfer characteristics of the thin film transistor devices containing the P3HT films and P3HT/PSSA films spin-cast either from toluene (left panel) or from chloroform (right panel). The drain voltage was set to $V_D=-40$ V.

For the devices with P3HT directly grown on SiO₂ (i.e., devices not containing a PSSA layer) we find somewhat higher effective mobilities for the ones grown from toluene. This is not surprising considering the edge-on alignment of the polymer chains discussed the previous section and the resulting π - π stacking in the direction of charge transport (Salleo *et al.* 2010). The hysteresis is moderate, which we attribute primarily to using the P3HT as received and to trapping at the semiconductor/dielectric interface.

The situation changes dramatically for the devices containing a PSSA/P3HT double-layer. While the effective mobility decreases for P3HT spin-cast from chloroform, it significantly increases (by \sim a factor of 4) when depositing P3HT from toluene. Thus, now the difference in performance between P3HT(toluene) and P3HT(chloroform) devices is strongly increased compared to layers directly deposited on SiO₂. As the GIXD measurements demonstrated that the alignment of P3HT is independent of the subjacent layer, we attribute this pronounced difference between the two different PSSA/P3HT films to the differences in the roughness of the PSSA/P3HT interface (1.2 nm when cast from chloroform and 0.2 nm when cast from toluene) which is located exactly where the conducting channel is formed. This is consistent with several reports from the literature: Steudel *et al.* showed a similar effect with SiO₂ dielectrics and pentacene TFTs; the decrease of the dielectric/semiconducting interface roughness resulted in a mobility improvement in the devices (Steudel *et al.* 2004). A detailed interface roughness vs. mobility investigation was also performed by Jo *et al.* with PS-*b*-PMMA block copolymer as interface layer on SiO₂ substrates, which clearly shows a charge carrier mobility dependence on the interface roughness between pentacene and PS-*b*-PMMA layer. There, in fact, only small changes of the interface roughness improve the charge carrier mobility significantly (Jo *et al.* 2008). Chua *et al.* reports a critical interface roughness of 0.7 nm between bilayers of orthogonal dissolved polymers (determined from AFM power spectra) where the charge carrier mobility drops significantly at the polymer/polymer interface (Chua *et al.* 2004). In passing we note that in all above-mentioned studies, the interface roughness in the multi-layer structures is derived before or after the final layer is deposited, while here we are able to directly investigate the roughness of the buried interface. Interestingly, the surface roughness of the SiO₂ substrate determined to be 0.5 nm is clearly larger than interface roughness the PSSA/P3HT(toluene) sample (i.e., in that case the PSSA layer smoothens the semiconductor/dielectric interface) (Okamura & Hahn 2010). This, in addition to a different interfacial chemical structure and resulting trap distribution and different dielectric constants of the PSSA and SiO₂ layers, appears to be the reason for

the pronounced mobility enhancement due to the introduction of the PSSA layer in the devices with P3HT spin-cast from toluene (Veres *et al.* 2003).

Another aspect worth mentioning is that the XRR measurements reveal a higher P3HT surface roughness with toluene as solvent. This results in a rougher P3HT(toluene)/Au interface in the region of the source and drain contacts, which can be expected to facilitate carrier injection due to local field enhancements and a larger injecting area. This results in higher current values in the PSSA/P3HT(toluene) devices and, thus, also in a larger extracted effective mobility (Pan & Sun 2009; Wang, Yan, & Tsukagoshi 2010). A detrimental effect of the inclusion of the PSSA layer is the increased hysteresis, which we attribute to residual water molecules present in the PSSA layer also after the annealing process; This hysteresis is also insofar problematic, as it makes a reliable determination of the effective mobility values difficult (all reported values have been observed for the sweep from positive to negative voltages, which is the first sweep in the measurement procedure). Nevertheless, the general mobility trends discussed above are clearly reflected in the actual evolutions of I_{DS} as a function of $V_G - V_T$ especially for small gate voltages. The more gradual increase of I_{DS} at large negative V_G in the downward sweep could be associated with a reduced mobility of carriers close to the P3HT/PSSA interface (i.e., mobility degradation (van Langevelde & Klaassen 1997; Mottaghi & Horowitz 2006)), which would also be consistent with the more pronounced effect for the more rough interface when spin-casting P3HT from chloroform. Such an interpretation is, however, inconsistent with the lack of any effect reminiscent of mobility degradation in the upward sweeps.

5.5 Conclusion

We show that a combination of x-ray reflectivity investigations with grazing incidence x-ray diffraction provides a valuable and non-invasive tool for simultaneously determining the interfacial morphology and preferred texturing in polymeric thin-film stacks spin-cast from orthogonal solvents. A particular strength of the approach is that XRR is capable of also analysing buried interfaces. This is shown here explicitly for a stack consisting of Si/SiO₂ as a substrate, a water soluble PSSA layer as a modification layer, and the semiconducting P3HT deposited from different solvents. The surface of the P3HT layer is studied also by AFM to compare the obtained trends to the XRR results. The choice of the solvent when spin-casting P3HT determines not only the alignment of the P3HT

crystallites (edge on when using toluene vs. face on for chloroform, as determined from the GIXD measurements), but also the roughness of the P3HT surface and the P3HT/PSSA interface. Interestingly, the observed trends for surface and interface roughness are opposite: Dissolving P3HT in chloroform decreases the P3HT surface roughness and increases the PSSA/P3HT interface roughness compared to using toluene as a solvent. This different roughness of the various interfaces is also suggested as the primary reason for strong variations in the hole mobilities observed in OTFTs containing the above described multi-layer stacks.

5.5.1 Acknowledgements

Financial support by the Austrian Science Fund (FWF): [21094] and P20972-N20 are gratefully acknowledged.

6 X-ray radiation damage of organic semiconductor thin films during grazing incidence diffraction experiments

6.1 Motivation

X-ray diffraction analysis with grazing incidence beam angle frequently are known as very material - sensitive investigation technique, especially in the field of soft matter studies (Sanyal *et al.* 1996; Yoon *et al.* 2007). During our x-ray investigations on soft matter material some unexpected diffraction feature behaviours were observed. Hence, a systematic radiation damage study on the polymer poly(3-hexylthiophene) and the small molecules sexithiophene and pentacene were performed, which clarified the unexpected measurement behaviours of the investigated systems. The work is peer reviewed and published as conference proceeding of the E-MRS 2011, held in Nice, France. A copy of the head of the paper is presented in Figure 6.1 containing the abstract and all contributed authors.



Contents lists available at SciVerse ScienceDirect

Nuclear Instruments and Methods in Physics Research B

journal homepage: www.elsevier.com/locate/nimb

X-ray radiation damage of organic semiconductor thin films during grazing incidence diffraction experiments

A. Neuhold^{a,*}, J. Novák^a, H.-G. Flesch^a, A. Moser^a, T. Djuric^a, L. Grodd^b, S. Grigorian^b, U. Pietsch^b, R. Resel^a

^aInstitute of Solid State Physics, Graz University of Technology, Graz, Austria

^bInstitute of Physics, University Siegen, Germany

ARTICLE INFO

Article history:

Received 5 May 2011

Received in revised form 4 July 2011

Available online 10 August 2011

Keywords:

Radiation damage

Organic semiconductor

Grazing incidence X-ray diffraction

Fluence

ABSTRACT

Since modern synchrotrons with highly intense X-ray beams are in use to investigate organic materials, the stability of soft matter materials during beam exposure is a crucial issue. Grazing incidence X-ray diffraction and specular X-ray reflectivity measurements were performed on thin films of organic semiconducting materials, like poly(3-hexylthiophene) (P3HT), sexithiophene and pentacene. These films were irradiated with an average flux density between 10^{15} and 10^{16} photons/(s mm²) and evidenced a different stability in synchrotron X-ray radiation. The semi-crystalline P3HT showed a clear intensity decrease of the 1 0 0 Bragg peak and 0 2 0 Bragg peak compared to the rather stable diffraction features of the molecular crystals sexithiophene and pentacene. The difference in synchrotron X-ray radiation stability is explained by the interaction of the X-ray beam with the individual chemical components in the molecules as well as by the different crystallinities of the materials. Furthermore, the semi-crystalline P3HT film exhibited an increase of film thickness after irradiation and the surface roughness slightly decreased. To summarize, this study shows a strong influence of synchrotron X-ray radiation to specific organic thin films like e.g. P3HT, while others like pentacene and sexithiophene are observed as quite stable.

© 2011 Elsevier B.V. All rights reserved.

Figure 6.1: Copy of the head of the publication

6.2 Introduction

Due to high beam intensity as well as highly collimated beam geometry, x-ray radiation of 3rd generation synchrotrons has become increasingly interesting for crystallographic characterization of organic thin films. Therefore several investigation techniques like scanning transmission x-ray microscopy or x-ray diffraction analysis, using synchrotron radiation are facilitated to examine crystal structures of organic molecules within thin films (Saito *et al.* 1995)(Moulin *et al.* 2006)(Gudat 1978)(Kowarik *et al.* 2010). In addition, the highly focused x-ray beam from a synchrotron facility is used to evidence the electronic structures of organic semiconducting materials (DeMasi *et al.* 2008)(Liu *et al.* 2002). These investigation techniques in combination with x-ray synchrotron radiation are often used without consideration of radiation induced damage of the investigated materials. Nevertheless, depending on the material and the x-ray energy, synchrotron radiation can cause damage to organic materials observed in crystallography of polymers or protein crystals (Müller *et al.* 2002)(Briskman 2007)(Homer, Cooper, & Gonzalez 2011). Radiation damage on self-assembled monolayers of alkanethiols are observed very frequently (Laibinis *et al.* 1991)(Heister *et al.* 2001), while P. Feulner *et al.* showed a reduction of x-ray induced damage at lower temperatures (Feulner *et al.* 2004).

One possible mechanism for radiation damage is the x-ray beam induced production of photoelectrons in the investigated materials. The large beam radiation intensity creates a huge amount of photoelectrons in the organic material as well as a valuable amount of photoelectrons in the substrate. Due to the large amount of beam-induced photoelectrons, reactive artifacts are formed in the organic materials which can cause damage in the molecular structure (Juers & Weik 2011)(O'Neill, Stevens, & Garman 2002). In addition, oxygen reacts easily with these artifacts, which results in oxidative degradation (Abdou & Holdcroft 1993). Therefore, material investigations with synchrotron x-ray radiation should be performed under exclusion of air.

In this work we present the results of a systematic study of the effect regarding synchrotron radiation damage on the crystallographic structure of semiconducting materials during grazing incidence diffraction experiments with x-ray energy of 8keV. As material of choice, the molecules pentacene (Fritz *et al.* 2004)(Minakata *et al.* 1992) and sexithiophene (Servet *et al.* 1994)(Servet *et al.* 1993) as well as the polymer poly(3-hexylthiophene) (Bao, Dodabalapur, & Lovinger 1996)[21](Kline *et al.* 2003)(Joshi, Grigorian, & Pietsch 2008) were used since they are frequently investigated materials in

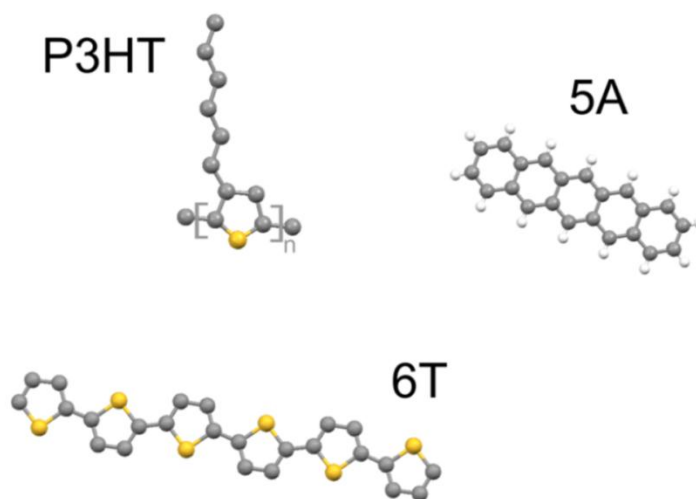


Figure 6.2: Molecular structure of poly(3-hexylthiophene) (P3HT), pentacene (5A) and sexithiophene (6T)

terms of structure-properties relationship for organic semiconducting devices. Up to now, x-ray radiation induced damage during diffraction experiments on these organic semiconducting materials has been assumed but not fully studied.

6.3 Materials and Methods

Film preparation: Poly(3-hexyl thiophene) (P3HT) with a low molecular weight ($M_w=20.4$ kDa) was solved in toluene ($c=6$ g/l) and spin coated on a silicon wafer covered by a 150nm thick thermally grown silicon oxide (sample size 20x20 mm). After annealing ($T=110^\circ\text{C}$) under vacuum conditions ($p=10^{-6}$ mbar) a 32 nm thick film was formed. 50 nm of pentacene (5A) and 60nm of sexithiophene (6T) were deposited on a silicon oxide substrate by physical vapor deposition (PVD) under high vacuum conditions ($p\sim 10^{-7}$ mbar). Figure 6.2 shows the molecular structures of P3HT ($[\text{C}_{10}\text{H}_{18}\text{S}]_n$), pentacene ($\text{C}_{22}\text{H}_{14}$) and sexithiophene ($\text{C}_{24}\text{H}_{14}\text{S}_6$). It is well known that spin casted P3HT with low molecular weight forms a semi-crystalline film with rather few oriented crystals, while 5A and 6T are highly crystalline (Joseph Kline, McGehee, & Toney 2006).

X-ray diffraction: Grazing incidence x-ray diffraction (GIXD) measurements were performed at the ID10B beamline at the European Synchrotron Radiation Facility (Grenoble, France). A diamond (111) double crystal monochromator was used to set the wavelength to a value of 1.53 Å. GIXD measurements were carried out with a one

dimensional gas filled linear detector (GABRIEL/EMBL), the scattered x-rays were collimated in the inplane direction with Soller slits on the secondary side mounted directly in front of the detector. The beam profile was set to 0.1mm x 0.5mm (vertical x horizontal) by the primary slit optic. During GIXD measurements the angle of incidence of the beam was set to $\alpha_i = 0.2^\circ$, which is slightly above the critical angle of the organic semiconducting material and therefore the total x-ray beam was striking the sample surface. The samples were placed inside the measurement chamber DHS1100 (Anton Paar), covered by a PEEK dome (Resel 2007)(Resel *et al.* 2003). The chamber was flushed with a continuous flow of helium to avoid the formation of highly reactive ozone close to the organic thin film surface and to prevent any oxidation of the organic film. The nominal beam flux was $\Phi_0 = 2.31 \times 10^{11}$ photons/ (s 100mA) (Zontone, Madsen, & Konovalov 2010). The P3HT samples and the 5A samples were investigated with an average flux density of 1.08×10^{15} photons/(s cm²) and an average flux of 6.79×10^{16} photons/(s cm²) on the specimen, respectively. The average flux density on the 6T specimen was 1.11×10^{16} photons/(s cm²). The different flux values are explained by the use of different attenuators. The investigated samples were illuminated for approximately 2 hours, which is a realistic exposure time for GIXD measurements of organic thin films. Using the linear detector two dimensional reciprocal space maps (RSM) as function of the in-plane (q_p) and out of plane (q_z) components of the momentum transfer have been measured ($q = \sqrt{q_p^2 + q_z^2} = 4\pi/\lambda \sin\Theta$). For further analysis the data of appropriate regions has been reduced to one dimension ($f(q_p)$) by integrating the intensity along the q_z direction. Specular X-ray reflectivity (XRR) measurements were performed using a scintillation counter (CYBERSTAR) with slit optics in front of the detector. The measured XRR data were simulated with the software package WinGixa (Leenaers & de Boer 1997), which determines the layer thickness by fitting the data with Parratt's recursive formalism (Parratt 1954). The surface roughness and the interface roughness of the specimen were determined using the Nevot and Croce approach (Gibaud & Hazra 2000).

6.4 Results

To systematically observe the x-ray stability of the organic thin film during GIXD measurement, performed with the intense and highly collimated synchrotron radiation, thin films of three different organic compounds were used: 5A, 6T and P3HT. First, the impact of the radiation on a 50 nm thick 5A film deposited on a silicon oxide substrate

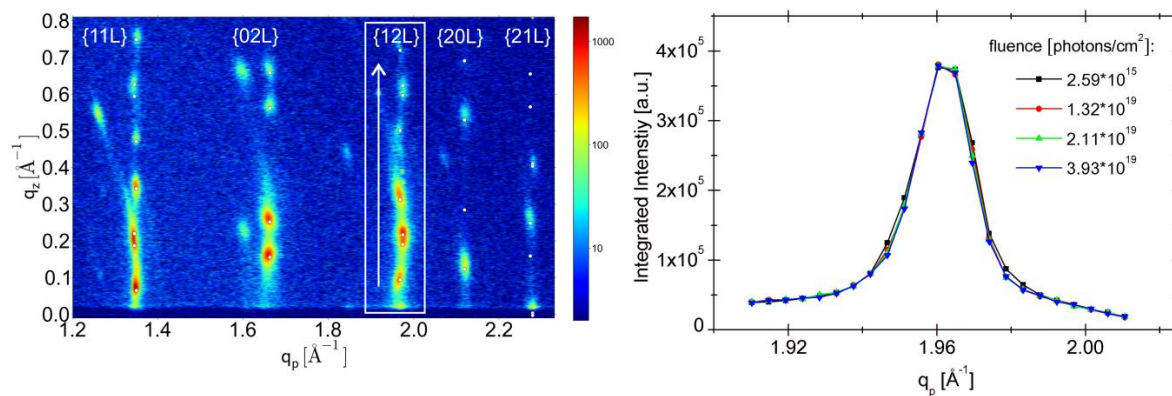


Figure 6.3: A representative reciprocal space map of the 5A sample (left): the white box indicates the integration range used to obtain the integrated intensity of the 12L rod. The intensity was integrated along the q_z direction, as indicated by an arrow in the left figure. The right image gives the obtained, absolute integrated intensity of the 12L rod as a function of the inplane component q_p of the scattering vector with increasing fluence striking the pentacene sample.

was investigated. Figure 6.3 (left) illustrate a representative RSM with the diffraction features of the 5A sample, where the five series of Bragg peaks (rod) of 5A are assigned. The white box indicates the integration range of the 12L rod. The right image of Figure 6.3 shows the integrated intensity of 12L series of Bragg peaks of pentacene along the inplane direction of the scattering angle. The estimated intensity range in q_z direction was 0.8 \AA^{-1} . Several measurement cycles were performed and therefore an ongoing number of photons reached the sample, however the pattern shows no detectable decrease of the diffraction intensity. A similar stable behaviour was found for the 11L, 02L, 20L and the 21L rod of pentacene.

The second system which was investigated, spin casted P3HT film on a silicon oxide substrate. Figure 6.4 exhibits the integrated intensity of the 100 Bragg peak (top) and of the 020 Bragg peak (bottom) with increasing x-ray radiation exposure. The integrated intensity was calculated within a q_z -range of 0.3 \AA^{-1} . Here, a strong decrease of the peak intensity was observed. The decrease of intensity regarding the 100 peak occurs faster compared to the 020 peak. Additionally a shift of the 020 peak to smaller q_p values (from 1.65 \AA^{-1} to 1.63 \AA^{-1}) is observable during the beam exposure which points to an increase of the interplanar spacing.

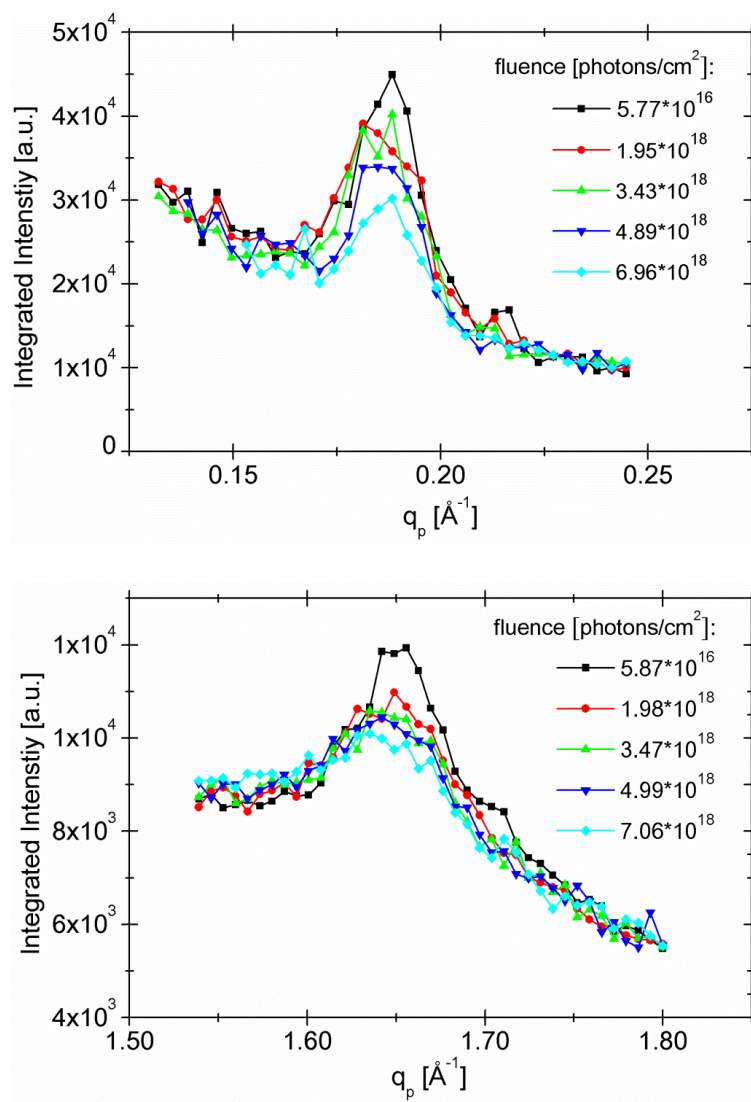


Figure 6.4: Absolute integrated intensity of the 100 Bragg peak (top) and of the 020 Bragg peak (bottom) as a function of the inplane component q_p of the scattering vector with increasing fluence at the P3HT sample

The lower curve in Figure 6.5 gives the XRR measurement of the pristine P3HT film and the upper curve shows the reflectivity data at the same illumination site on the specimen at a fluence of 9.64×10^{16} photons/cm². The fits of the experimental data are shown as the continuous lines and the insert shows the layer model of the samples.

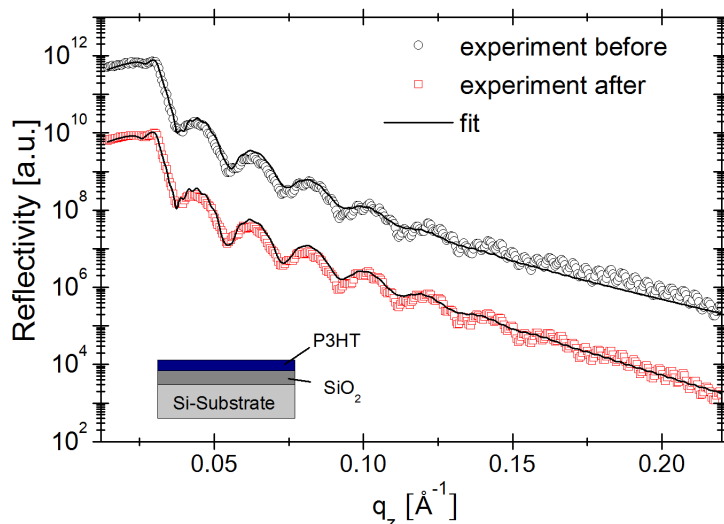


Figure 6.5: Specular x-ray reflectivity curves of the P3HT films on SiO₂/Si substrate (model of the layer stack given as inset). The lower curve gives the XRR data before x-ray exposure (rectangles) and the upper curve gives the XRR data after the beam exposure (circles). The fits are evinced by the black lines, respectively.

For clarity, the upper curve was manually vertical shifted. Both curves show the high frequent oscillations of the silicon oxide layer superposed with the low frequent oscillation of the P3HT film. The shorter period of the Kiessig fringes (Kiessig 1931) of P3HT after the GIXD measurements indicates an increase of the layer thickness. XRR measurements reveal a slight increase of the layer thickness of the P3HT film from 31.6 ± 0.2 nm to 32.1 ± 0.2 nm and a decrease of film roughness from 0.3 to 0.2 nm. In addition the thickness of the subjacent SiO₂ layer on Si was determined to 143 ± 5 nm and the layer roughness was 0.3 ± 0.1 nm.

The third investigated organic material was the molecule 6T. Figure 6.7 evidences the integrated intensities of the 11L series of Bragg peaks (rod) of 6T after highly intense beam exposure. The diffraction pattern of this 6T rod shows no decrease of intensity and no significant shift in the in-plane direction of the scattering vector. A similar stable behaviour was measured for the 20L rod and the 21L rod in the 6T film. The q_z -range for the integrated intensity was 0.6 \AA^{-1} .

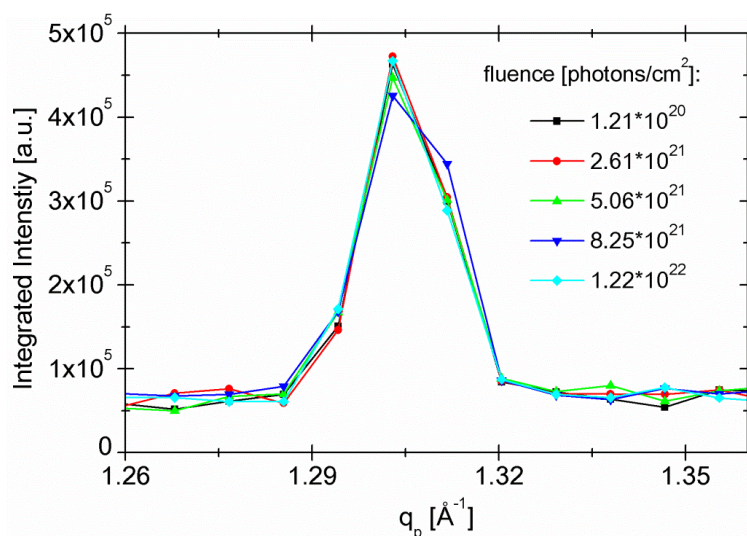


Figure 6.6: Absolute integrated intensity of 11L rod as a function of the inplane component q_p of the scattering vector with increasing fluence at the sexithiophene sample.

6.5 Discussion

The systematic x-ray exposure study of the three semiconducting organic materials showed a distinct difference in the stability of the diffraction peaks of the individual materials. No decrease regarding the diffraction intensities of 5A and 6T rods were observed. However, the decreases of intensity of the two P3HT Bragg peaks were clearly evidenced and are associated to beam degradation. Figure 6.7 gives a comparison of the normalized areas beneath the integrated diffraction peaks of the three investigated organic materials as a function of the fluence. The two diffraction peaks of P3HT show a strong decrease of intensity with respect to the quantity of received photons but the diffraction features of 5A and 6T are unaffected by the intense x-ray radiation. It is known that molecules consisting exclusively of aromatic hydrocarbons, like pentacene are more resisting to radiation damage due to the absence of elements with high electron affinity (Chapiro 1988). Furthermore, molecular structures formed by aromatic hydrocarbon rings will dissipate the incorporated radiation energy to the C-H rings and these molecules will be less affected by x-ray illumination. In addition, pentacene crystallizes in a well-known structure (Schiefer *et al.* 2007)(Yoshida, Inaba, & Sato 2007) arranging in the rather densely packed crystalline structure (Nabok *et al.* 2007).

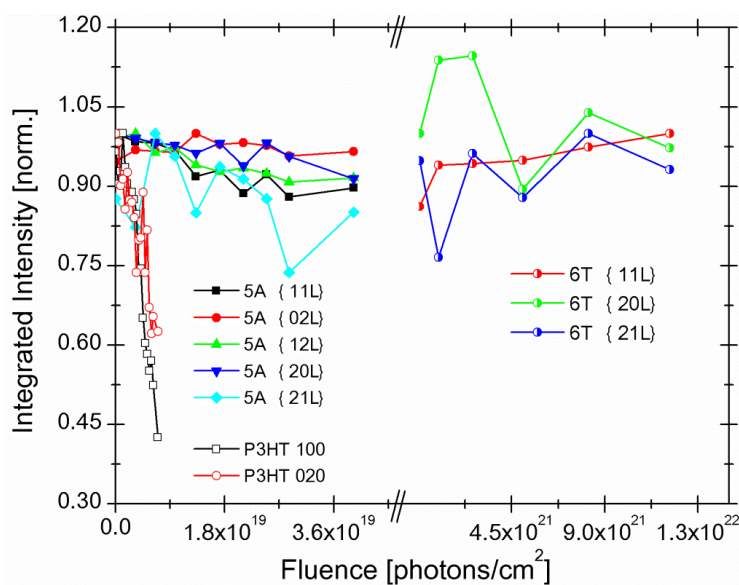


Figure 6.7: Comparison of the normalized diffraction intensities of the investigated organic semiconducting materials with respect to fluence.

In comparison to the stable behavior of pentacene, P3HT thin films are rather sensitive due to synchrotron x-ray beam irradiation. In contrast to the 5A molecule, the polymer P3HT consists of side chains and a sulfur atom is contained within in the aromatic ring, which has a high electron affinity. The photoelectrons created during x-ray radiation lead to a formation of free radicals like $S^{\bullet-}$, $CS^{\bullet-}$, $CHS^{\bullet-}$ etc. (Alfassi 1999). The chemical modification of the molecules will change the chemical structure (Soukupová, Sassi, & Jerábek 2010). The formation of non-saturated fragments depends on the molecular shape as well as the composition of the molecule. In addition, the long alkyl side chains of P3HT are highly affected by x-ray radiation (Chapiro 1988)(Zharnikov & Grunze 2002). Very intense x-ray illumination results in side chain cleavages of P3HT giving an additional reason for the instable intensity in the diffraction pattern. The irreversible change of d-spacing of the 020 Bragg peak of the P3HT film (Figure 6.4 bottom) results from the high radiation dose, which was also observed in other organic materials e. g. protein crystals (Weik *et al.* 2000)(Weik *et al.* 2001)(Burmeister 2000). The increase of the organic film thickness (Figure 6.5) due to x-ray irradiation was already observed in polystyrene and was related to possible radiation induced cross-linking within the films (Bhatta *et al.* 2009)(Richter *et al.* 2006).

Interestingly, no decrease of diffraction peak intensities could be observed in the 6T film, which also contains sulfur atoms. Physical vapor deposited 6T films are highly

crystalline and show a defined crystal structure (Horowitz *et al.* 1995) with a dense crystalline molecular packing compared to the loose packing in the semi-crystalline P3HT films with a large amorphous part. This close molecular packing in 6T films is supposed to inhibit the influence of free radicals (Briskman 2007). Moreover, the small molecule 6T does not have any long side chains, which avoid the formation of free radicals from side chain scission. The high crystallinity together with the dense molecular packing result in a more stable behavior upon synchrotron x-ray beam irradiation.

6.6 Conclusion

In this work the most prominent materials of organic electronics are studied in terms of structural stability of thin films during synchrotron x-ray diffraction experiments. The diffraction features of the spin-coated polymer P3HT decrease markedly faster compared to the diffraction features of sexithiophene or pentacene. This decrease can be explained by the possible formation of reactive artifacts from electron affine components in the molecule during beam exposure and side chain cleavage due to x-ray irradiation combined with the low crystallinity of P3HT films. The missing side chains in the small molecule 6T and the absence of electron affine elements in the small molecule 5A, results in higher x-ray illumination stability of these closely packed and highly crystalline materials. Pentacene and sexithiophene show a stable diffraction pattern during a fluence in a range up to 10^{22} photons/cm². This work shows clearly that organic semiconducting materials have different stability to synchrotron radiation. Therefore one has to be careful with structure analysis when using synchrotron radiation and degradation checks are required to get trustful results from x-ray scattering experiments.

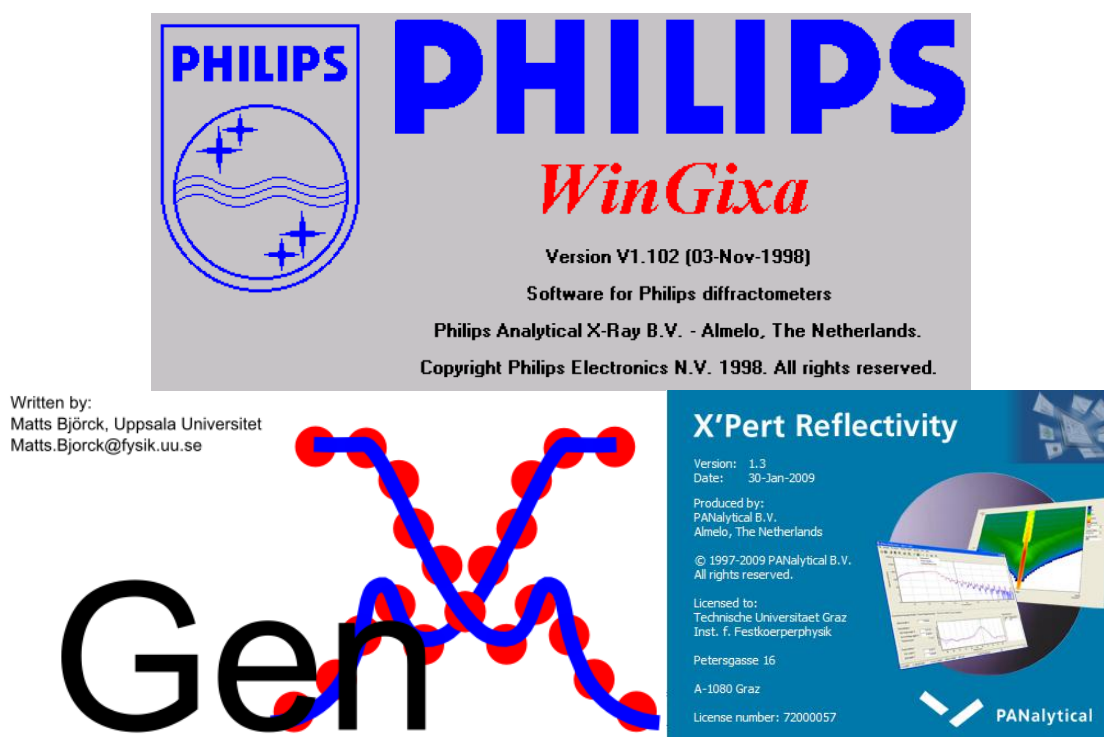
6.7 Acknowledgements

We acknowledge the European Synchrotron Radiation Facility (Grenoble, France) for provision of synchrotron radiation facilities and we thank F. Zontane and O. Konovalov for assistance in using beamline ID10B. This work was financially supported by the Austrian Research Promotion Agency (FFG) within the research project cluster ISOTEC.

III. APPENDIX A: XRR Software Comparison

A.1 Introduction

This appendix should compare the x-ray reflectivity fit softwares, which were used within this study. Three different fit programs are introduced and the experimental data of a single Alq₃ layer on a SiO₂/Si substrate was simulated and was compared by these software packages. Starting with the oldest software WinGixa from PHILIPS (Almelo 1997), which uses a simulated annealing algorithm, followed by the freeware GenX (Björck & Andersson 2007) using a differential evolution algorithm and finally the X'Pert Reflectivity 1.3 software from PANalytical (Dane *et al.* 1998), which uses a genetic fitting algorithm (see App. Figure 1). Here, the advantages and disadvantages of each program are quickly expressed and visualized by a simple example, where the same x-ray reference data was fitted by the different simulation packages. The study was started by Dr. Jíri Novák and the following chapter comprises a comparison of the used XRR software.



App. Figure 1: Image of the WinGixa software intro (top), the GenX program intro (bottom left) and the X'Pert PANalytical intro (bottom right)

cumbersome data input and the rather complicated handling of the data after simulation. The package does not have any material database and no help menu (see App. Figure 2).

The second XRR simulation software was the freeware *GenX* (GenX), which is based on a python algorithm using a well-organized graphical user interface (GUI) (Björck & Andersson 2007). The GUI comprises a python script (App. Figure 3), a parameter window (App. Figure 4) and the plot section (App. Figure 5). One can set parameter limits for each parameter in the parameter window (App. Figure 4), which is the main benefit of this software. Two other big advantages are the error estimation on each fitting parameter and the online user manual. The sample arrangements can be easily implemented to the software, following the introductions in the manual. However the diffractometer parameters, which have to be set in the python script, are rather enigmatically implemented and there exists no material database in the package. Therefore, basic knowledge about python language will definitely help to use this software package. The optical constants of the used materials have to be estimated by using the Henke tables (Henke, Gullikson, & Davis 1993) and the dispersion and the absorption coefficients have to be implemented into the python script (see App. Figure 3). This package can be used to simulate simple layer stacks, but the algorithm gets horrible slow if the sample arrangement contains more than three layers.

```

# Give n for rho=1 reldens is than density in g/cm^3 directly
# calculat decrements in Matlab like:
# [chir,chiij]=gchi0(0.040,'Si1',1); (chir-chii*j)/2.
nL2=1.-3.3344e-006 +9.1643e-009J; rhoL2=1.424; # AlQ3 = Al1C27H18N3O3
nL1=1.-3.2435e-006 +4.1848e-008J; rhoL1=2.64; # SiO2
nSub=1.-3.2632e-006 +7.4144e-008J; rhoSub=2.329; # Si
# layer thicknesses
dL2=400;
dL1=1000;
# roughness
SigL2=5;
SigL1=5;
SigSub=3;
MyVar.newVar('Back',5) # background
MyVar.newVar('l0',2.029e7) # sample length
ws0=0.05; # Beam width = width of slit 0
ls=20; # sample length
beamDiverg=.025;

solver.setFomfunc(Log2Fom)
#solver.setFomfunc(Chi2Fom)
#solver.setFomfunc(Chi2BarsFom)

La2=Layer(n=nL2,d=dL2,sigmar=SigL2, \
reldens=rhoL2)
La1=Layer(n=nL1,d=dL1,sigmar=SigL1, \
reldens=rhoL1)
sub=Layer(n=nSub,sigmar=SigSub,reldens=rhoSub)

```

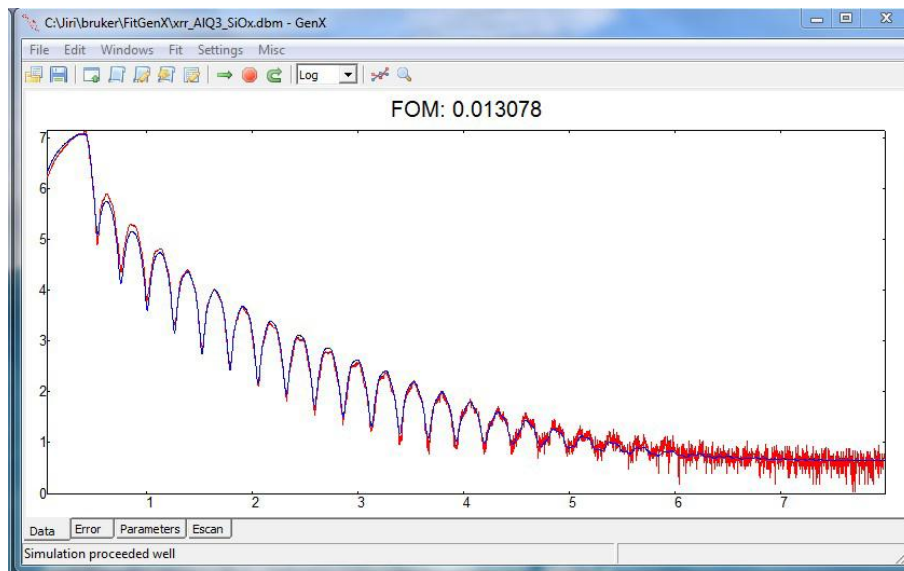
App. Figure 3: Script window of the GenX software package (Novák 2010)

GenX - Parameters

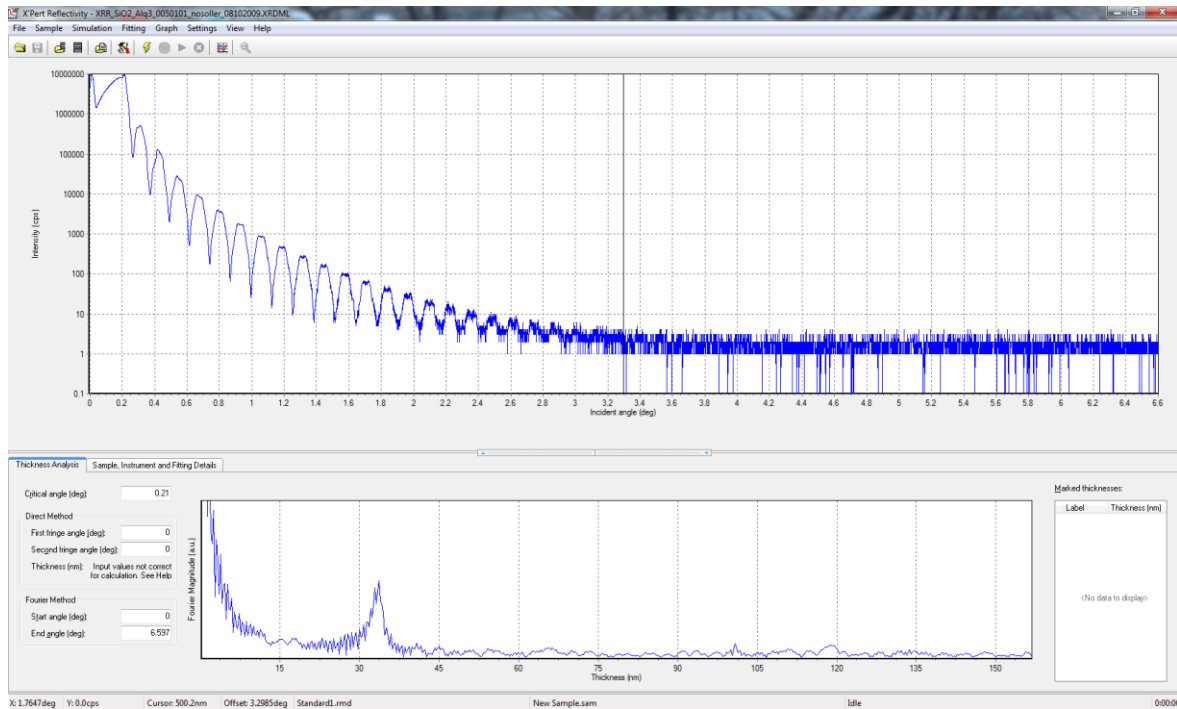
	Parameter	Value	Fit	Min	Max	Error
0	MyVar.setI0	124875.795415	<input checked="" type="checkbox"/>	1.000000	100000000.000000	(-5.45e+003,8.36e+003)
1	MyVar.setBack	4.291668	<input checked="" type="checkbox"/>	3.500000	6.500000	(-0.381,0.271)
-	inst.setBeaw	0.171482	<input type="checkbox"/>	0.030000	0.300000	(-0.0644,0.075)
2	inst.setRes	0.018000	<input checked="" type="checkbox"/>	0.000000	0.200000	(-0.00129,0.000638)
-	inst.setSamlen	16.330678	<input type="checkbox"/>	0.000000	200.000000	(-1.34,2.29)
-	inst.setResinrange	2.000000	<input type="checkbox"/>	0.000000	10.000000	None
3	La2.setD	326.690050	<input checked="" type="checkbox"/>	310.000000	340.000000	(-0.313,0.262)
-	La2.setReldens	1.292948	<input type="checkbox"/>	1.000000	1.600000	(-0.0572,0.013)
4	La2.setSigmar	5.806203	<input checked="" type="checkbox"/>	2.000000	10.000000	(-0.15,0.155)
5	La1.setD	1007.495841	<input checked="" type="checkbox"/>	800.000000	1100.000000	(-3.05,3.65)
-	La1.setReldens	2.315768	<input type="checkbox"/>	2.100000	3.000000	(-0.0232,0.0234)
6	La1.setSigmar	3.424320	<input checked="" type="checkbox"/>	2.000000	8.000000	(-0.18,0.18)
-	sub.setReldens	2.329000	<input type="checkbox"/>	1.630300	3.027700	None
7	sub.setSigmar	1.000001	<input checked="" type="checkbox"/>	1.000000	6.000000	(-1.34e-006,4.98)
-		0.000000	<input type="checkbox"/>	0.000000	0.000000	

Simulate Escan Eproject

App. Figure 4: Parameter window of the GenX software package (Novák 2010)



App. Figure 5: Plot window of the GenX software package (Novák 2010)



App. Figure 6: X'Pert Reflectivity software with the direct determination of the thickness via the Fourier method (bottom window).

The third XRR simulation package introduced in this chapter is the *X'Pert Reflectivity 1.3* program, provided from PANalytical. This software package is perfectly suited for XRR simulations of single layers and multilayer stacks and therefore the most frequently used simulation program in this work. It contains all the advantages of the latter two software packages, like convergence speed, parameter limits, error estimation, comfortable data import and export and a well explained GUI with a sufficient help menu. Furthermore, the package contains an additional thickness estimation function, which is realized by a Fourier Method and one can directly take the layer thickness from the GUI, without simulation (see bottom window in App. Figure 6). In addition the software comprises a material database, where new materials can be easily implemented.

The software packages use the dispersion coefficient δ and the absorption coefficient β to calculate the density parameters of the investigated layers. The two parameters are taken from the Henke table (Henke, Gullikson, & Davis 1993), which requires the composition of the material, the mass density and the wavelength in nm (or Energy in eV). One can then estimate the electron density ρ_e of the materials in the following way:

$$\rho_e = \frac{\Re(SLD)}{r_e} \text{ in } [\text{L}^{-3}] \quad (\text{A.1})$$

where r_e denotes the classical electron radius and the scattering length density (SLD) is calculated by dispersion coefficient δ and the absorption coefficient β and the wavelength of the radiation λ

$$SLD = \frac{(\delta - i\beta)2\pi}{\lambda^2}. \quad (\text{A.2})$$

The mass density in g/cm^3 [M L^{-3}] is then calculated

$$\rho_m = \frac{m}{V}, \quad (\text{A.3})$$

Where m is the mass and V is the volume of the unit cell, which can be only calculated if the crystal structure of the material is known. Without knowledge of the crystal structure of the material, one has to know the composition of the material, its atomic mass and how many atoms can be arranged per cm^3 . The mass density can be calculated from the electron density of the material by

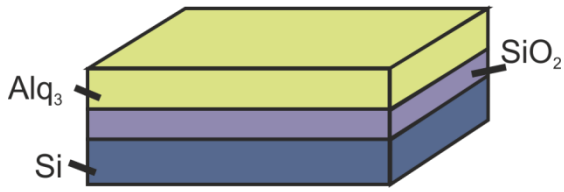
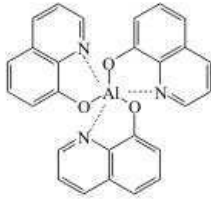
$$\rho_m = \rho_e [\text{cm}^{-3}] \frac{m_A u}{\#electrons}, \quad (\text{A.4})$$

where m_A is the atomic mass of the material composition and u is the atomic mass unit $u = 1.660538921 \times 10^{-24}$ g.

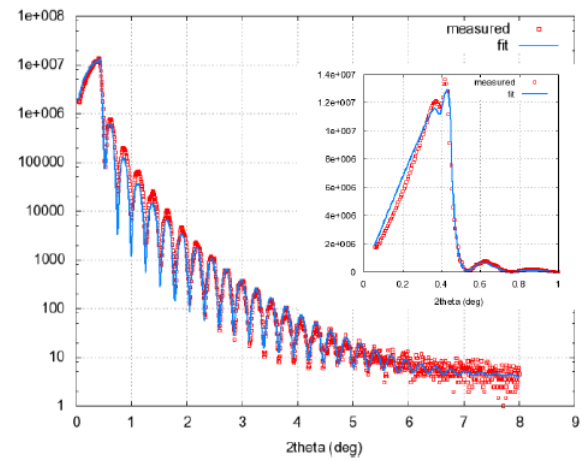
A.3 Software Comparison

For this comparison a nominal 40 nm thick Alq_3 layer deposited on a 100 nm thick thermally oxidized silicon oxide was analysed. As substrate a 1 mm thick silicon wafer was used (see App. Figure 7 a)). The sample was measured with the Bruker D8 in reflectivity geometry (chapter 3.3). App. Figure illustrates the experimental data together with the WinGixa fit (App. Figure 7 b)), the GenX fit (App. Figure 7 c)) and the X'Pert Reflectivity fit (App. Figure 7 d)) The simulations were performed without any further knowledge about the layer properties (material, layer thickness, roughness), while the beam geometry and sample geometry were considered in the simulations.

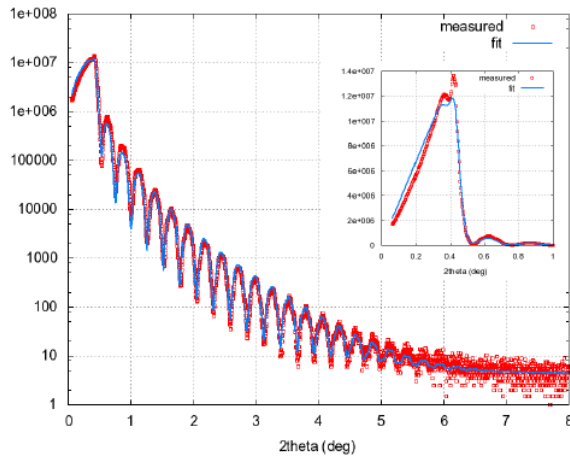
a)

Alq₃ structure:

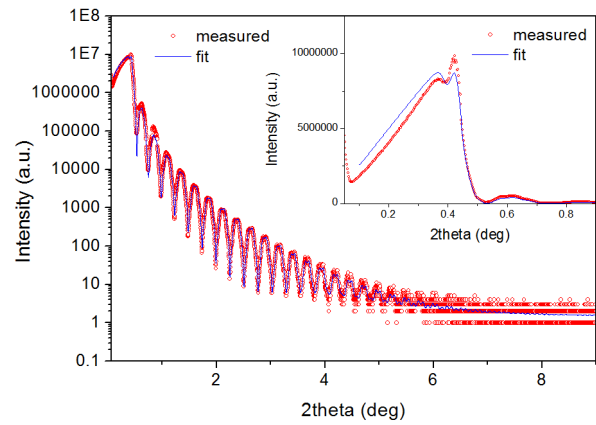
b)



c)



d)



App. Figure 7: a) Alq₃/SiO₂/Si sample arrangement and the Alq₃ structure, b), c) and d) reveal the same experimental data (red circle) simulated with WinGixa, GenX and X'Pert Reflectivity (blue line), respectively. The inset in the graphs shows the linear view of the critical angle regime.

App. Table 1: Comparison of the extracted parameters from the used software packages, WinGixa, GenX and X'Pert Reflectivity. The simulated values are the thickness d , the surface and interface roughness σ and the mass density ρ of the individual layers in the stack.

layer	WinGixa				GenX				X'Pert Reflectivity			
	d (nm)	σ (nm)	ρ_m (g/cm ³)	ρ_e (cm ⁻³)	d (nm)	σ (nm)	ρ_m (g/cm ³)	ρ_e (cm ⁻³)	d (nm)	σ (nm)	ρ_m (g/cm ³)	ρ_e (cm ⁻³)
Alq ₃	32.6	0.32	1.30	407	32.76 ±0.03	0.58 ±0.02	1.29 ±0.05	404 ±16	33.8 ±0.1	0.62 ±0.03	1.31 ±0.14	410 ±3
SiO ₂	100.7	0.37	2.28	696	100.7 ±0.4	0.34 ±0.02	2.31 ±0.02	699 ±10	100.7 ±4.5	0.23 ±0.04	2.25 ±0.03	689 ±15
Si	--	0.33	2.33	712	--	0.1 ±0.4	2.33	712	--	0.22	2.33	712

App. Table 1 shows a comparison of the extracted fit parameters of each individual layer in the sample. All three software packages give a rather similar thickness value of the SiO₂ layer. The Alq₃ layer thicknesses from WinGixa and GenX are very close to each other, while the X'Pert Reflectivity gives a slightly thicker value (deviation ~3.3%). In contrast, the Alq₃ surface roughness of the GenX package is in the same range as the X'Pert Reflectivity package, while the WinGixa package gives just the half magnitude of the surface roughness (deviation ~51%). The simulated mass densities of all three simulation packages in App. Table 1 show comparable values, which can also be found in literature, e.g. for Alq₃ in (Farahzadi et al. 2010).

A.4 Conclusion

Summing up the working experience with the three software packages clearly highlights some advantages and disadvantages of each simulation program. The main drawback of WinGixa is the complicated data processing of the experimental and simulated data before and after the simulation procedure and the missing error estimation of the fit parameters. In comparison the X'Pert Reflectivity software is a perfectly suited improvement of the old WinGixa software with error estimation, parameter limits, and comfortable data processing and additionally comprises a well-organized help menu. In contrast to the latter two commercial software packages, the free GenX software is a well-suited alternative and also comprises the important fitting features like parameter limits and error evaluation. The drawback of GenX is only the expensive fitting time if the sample arrangement contains more than three layers.

IV. BIBLIOGRAPHY

- Abdou, M.S.A. & Holdcroft, S. (1993) Mechanisms of photodegradation of poly(3-alkylthiophenes) in solution. *Macromolecules*, **26**, 2954–2962.
- Abelès, F. (1950) Recherches sur la propagation des ondes électromagnétiques sinusoïdales dans les milieux stratifiés. Application aux couches minces. *Ann. Phys. (Paris)*, **5**, 596–640.
- Alfassi, Z. (1999) *S-centered Radicals (The Chemistry Of Free Radicals)*. 1st ed., John Wiley & Sons Ltd, Chichester, New York.
- Almelo. (1997) *Win – Gixa Software and User Manual, Philips Analytical X-Ray*. The Netherlands.
- Als-Nielsen, J. & McMorrow, D. (2001) *Elements of modern X-ray physics*. Wiley, New York.
- Baeg, K.-J. (2011) Polymer Dielectrics and Orthogonal Solvent Effects for High-Performance Inkjet-Printed Top-Gated P-Channel Polymer Field-Effect Transistors. *ETRI Journal*, **33**, 887–896.
- Baldo, M.A., Kozlov, V.G., Burrows, P.E., Forrest, S.R., Ban, V.S., Koene, B. & Thompson, M.E. (1997) Low pressure organic vapor phase deposition of small molecular weight organic light emitting device structures. *Applied Physics Letters*, **71**, 3033–3035.
- Bao, Z., Dodabalapur, A. & Lovinger, A.J. (1996) Soluble and processable regioregular poly(3-hexylthiophene) for thin film field-effect transistor applications with high mobility. *Applied Physics Letters*, **69**, 4108–4110.
- Bhatta, U.M., Ghatak, J., Mukhopadhyay, M., Wang, J., Narayanan, S. & Satyam, P.V. (2009) Synchrotron X-ray induced damage in polymer (PS) thin films. *Nuclear Instruments and Methods in Physics Research Section B: Beam Interactions with Materials and Atoms*, **267**, 1807–1810.
- Birkholz, M. (2006) *Thin Film Analysis by X-ray Scattering*. WILEY-VCH Verlag GmbH & Co, Weinheim.
- Björck, M. & Andersson, G. (2007) GenX: an extensible X-ray reflectivity refinement program utilizing differential evolution. *Journal of Applied Crystallography*, **40**, 1174–1178.
- Blochowitz, J., Fritz, T., Pfeiffer, M., Leo, K., Alloway, D.M., Lee, P.A. & Armstrong, N.R. (2001) Interface electronic structure of organic semiconductors with controlled doping levels. *Organic Electronics*, **2**, 97–104.
- de Boer, R.W.I., Iosad, N.N., Stassen, A.F., Klapwijk, T.M. & Morpurgo, A.F. (2005) Influence of the gate leakage current on the stability of organic single-crystal field-effect transistors. *Applied Physics Letters*, **86**, 032103.

- de Boer, D.K., Leenaers, A.J., van der Wielen, M.W., Cohen Stuart, M., Fler, G., Nieuwhof, R., Marcelis, A.T. & Sudhölter, E.J. (1998) Specular and non-specular X-ray reflection from inorganic and organic multilayers. *Physica B: Condensed Matter*, **248**, 274–279.
- Born, M., Wolf, E. & Bhatia, A.B. (1999) *Principles of Optics: Electromagnetic Theory of Propagation, Interference and Diffraction of Light*. Cambridge University Press.
- Brinkmann, M. (2011) Structure and morphology control in thin films of regioregular poly(3-hexylthiophene). *Journal of Polymer Science Part B: Polymer Physics*, **49**, 1218–1233.
- Briskman, B. (2007) Be careful when using X-ray exposure analysis for polymers. *Nuclear Instruments and Methods in Physics Research Section B: Beam Interactions with Materials and Atoms*, **265**, 276–280.
- Burmeister, W.P. (2000) Structural changes in a cryo-cooled protein crystal owing to radiation damage. *Acta Crystallographica Section D Biological Crystallography*, **56**, 328–341.
- Burroughes, J.H., Bradley, D.D.C., Brown, A.R., Marks, R.N., Mackay, K., Friend, R.H., Burns, P.L. & Holmes, A.B. (1990) Light-emitting diodes based on conjugated polymers. *Nature*, **347**, 539–541.
- Chang, J.-F., Sun, B., Breiby, D.W., Nielsen, M.M., Sölling, T.I., Giles, M., McCulloch, I. & Sirringhaus, H. (2004) Enhanced Mobility of Poly(3-hexylthiophene) Transistors by Spin-Coating from High-Boiling-Point Solvents. *Chemistry of Materials*, **16**, 4772–4776.
- Chapiro, A. (1988) Chemical modifications in irradiated polymers. *Nuclear Instruments and Methods in Physics Research Section B: Beam Interactions with Materials and Atoms*, **32**, 111–114.
- Cheng, H.-L., Lin, W.-Q. & Wu, F.-C. (2009) Effects of solvents and vacancies on the electrical hysteresis characteristics in regioregular poly(3-hexylthiophene) organic thin-film transistors. *Applied Physics Letters*, **94**, 223302.
- Chiesa, M., Bürgi, L., Kim, J.-S., Shikler, R., Friend, R.H. & Sirringhaus, H. (2005) Correlation between Surface Photovoltage and Blend Morphology in Polyfluorene-Based Photodiodes. *Nano Letters*, **5**, 559–563.
- Chua, L. -L., Ho, P.K.H., Sirringhaus, H. & Friend, R.H. (2004) Observation of Field-Effect Transistor Behavior at Self-Organized Interfaces. *Advanced Materials*, **16**, 1609–1615.
- Croce, P. & Nénot, L. (1976) Étude des couches minces et des surfaces par réflexion rasante, spéculaire ou diffuse, de rayons X. *Revue de Physique Appliquée*, **11**, 113–125.
- Daillant, J. & Gibaud, A. (eds). (2009) *X-ray and Neutron Reflectivity Principles and Applications*. Springer-Verlag Berlin Heidelberg.

- Dane, A.D., Veldhuis, A., Boer, D.K.G. de, Leenaers, A.J.G. & Buydens, L.M.C. (1998) Application of genetic algorithms for characterization of thin layered materials by glancing incidence X-ray reflectometry. *Physica B: Condensed Matter*, **253**, 254–268.
- DeMasi, A., Piper, L.F.J., Zhang, Y., Reid, I., Wang, S., Smith, K.E., Downes, J.E., Peltekis, N., McGuinness, C. & Matsuura, A. (2008) Electronic structure of the organic semiconductor Alq₃ (aluminum tris-8-hydroxyquinoline) from soft x-ray spectroscopies and density functional theory calculations. *The Journal of Chemical Physics*, **129**, 224705.
- Dhagat, P., Haverinen, H.M., Kline, R.J., Jung, Y., Fischer, D.A., DeLongchamp, D.M. & Jabbour, G.E. (2009) Influence of Dielectric Surface Chemistry on the Microstructure and Carrier Mobility of an n-Type Organic Semiconductor. *Advanced Functional Materials*, **19**, 2365–2372.
- Dosch, H. (1992) *Critical Phenomena at Surfaces and Interfaces*. Springer Tracts in Modern Physics.
- Dürr, A.C., Schreiber, F., Kelsch, M., Carstanjen, H.D., Dosch, H. & Seeck, O.H. (2003) Morphology and interdiffusion behavior of evaporated metal films on crystalline diindenoperylene thin films. *Journal of Applied Physics*, **93**, 5201–5209.
- Farahzadi, A., Beigmohamadi, M., Niyamakom, P., Kremers, S., Meyer, N., Heuken, M. & Wuttig, M. (2010) Characterization of amorphous organic thin films, determination of precise model for spectroscopic ellipsometry measurements. *Applied Surface Science*, **256**, 6612–6617.
- Faupel, F., Willecke, R. & Thran, A. (1998) Diffusion of metals in polymers. *Materials Science and Engineering: R: Reports*, **22**, 1–55.
- Feulner, P., Niedermayer, T., Eberle, K., Schneider, R., Menzel, D., Baumer, A., Schmich, E., Shaporenko, A., Tai, Y. & Zharnikov, M. (2004) Strong Temperature Dependence of Irradiation Effects in Organic Layers. *Physical Review Letters*, **93**, 178302.
- Fladischer, S., Neuhold, A., Kraker, E., Haber, T., Lamprecht, B., Salzmann, I., Resel, R. & Grogger, W. (2012) Diffusion of Ag into Organic Semiconducting Materials: A Combined Analytical Study Using Transmission Electron Microscopy and X-ray Reflectivity. , submitted.
- Floreato, L., Cossaro, A., Gotter, R., Verdini, A., Bavdek, G., Evangelista, F., Ruocco, A., Morgante, A. & Cvetko, D. (2008) Periodic Arrays of Cu-Phthalocyanine Chains on Au(110). *Journal of Physical Chemistry C*, **112**, 10794–10802.
- Fritz, S.E., Martin, S.M., Frisbie, C.D., Ward, M.D. & Toney, M.F. (2004) Structural Characterization of a Pentacene Monolayer on an Amorphous SiO₂ Substrate with Grazing Incidence X-ray Diffraction. *Journal of the American Chemical Society*, **126**, 4084–4085.
- GenX. (<http://genx.sourceforge.net/>).

- Gholamrezaie, F., Andringa, A.-M., Roelofs, W.S.C., Neuhold, A., Kemerink, M., Blom, P.W.M. & de Leeuw, D.M. (2012) Charge Trapping by Self-Assembled Monolayers as the Origin of the Threshold Voltage Shift in Organic Field-Effect Transistors. *Small*, **8**, 241–245.
- Gibaud, A. & Hazra, S. (2000) X-ray reflectivity and diffuse scattering. *Current Science*, **78**, 1467–1478.
- Gibaud, A., Vignaud, G. & Sinha, S.K. (1993) The correction of geometrical factors in the analysis of X-ray reflectivity. *Acta Crystallographica Section A*, **49**, 642–648.
- Grandin, H.M., Tadayyon, S.M., Lennard, W.N., Griffiths, K., Coatsworth, L.L., Norton, P.R., Popovic, Z.D., Aziz, H. & Hu, N.X. (2003) Rutherford backscattering and secondary ion mass spectrometry investigation of Mg:Ag-tris(8-hydroxy quinoline) aluminum interfaces. *Organic Electronics*, **4**, 9–14.
- Gudat, W. (1978) Soft X-ray microscopy and lithography with synchrotron radiation. *Nuclear Instruments and Methods*, **152**, 279–288.
- Hammer, M.S., Deibel, C., Pflaum, J. & Dyakonov, V. (2010) Effect of doping of zinc oxide on the hole mobility of poly(3-hexylthiophene) in hybrid transistors. *Organic Electronics*, **11**, 1569–1577.
- Heister, K., Zharnikov, M., Grunze, M., Johansson, L.S.O. & Ulman, A. (2001) Characterization of X-ray Induced Damage in Alkanethiolate Monolayers by High-Resolution Photoelectron Spectroscopy. *Langmuir*, **17**, 8–11.
- Henke, B., Gullikson, E. & Davis, J. (1993) X-Ray Interactions: Photoabsorption, Scattering, Transmission, and Reflection at $E = 50\text{--}30,000$ eV, $Z = 1\text{--}92$. henke.lbl.gov/optical_constants/. *Atomic Data and Nuclear Data Tables*, **54**, 181–342.
- Hirose, Y., Kahn, A., Aristov, V., Soukiassian, P., Bulovic, V. & Forrest, S.R. (1996) Chemistry and electronic properties of metal-organic semiconductor interfaces: Al, Ti, In, Sn, Ag, and Au on PTCDA. *Physical Review B*, **54**, 13748–13758.
- Holý, V. & Baumbach, T. (1994) Nonspecular x-ray reflection from rough multilayers. *Physical Review B*, **49**, 10668–10676.
- Holý, V., Kuběna, J., Ohlídal, I., Lischka, K. & Plotz, W. (1993) X-ray reflection from rough layered systems. *Physical Review B*, **47**, 15896–15903.
- Homer, C., Cooper, L. & Gonzalez, A. (2011) Energy dependence of site-specific radiation damage in protein crystals. *Journal of Synchrotron Radiation*, **18**, 338–345.
- Horowitz, G., Bachet, B., Yassar, A., Lang, P., Demanze, F., Fave, J.-L. & Garnier, F. (1995) Growth and Characterization of Sexithiophene Single Crystals. *Chemistry of Materials*, **7**, 1337–1341.
- Huang, F., Cheng, Y.-J., Zhang, Y., Liu, M.S. & Jen, A.K.-Y. (2008) Crosslinkable hole-transporting materials for solution processed polymer light-emitting diodes. *Journal of Materials Chemistry*, **18**, 4495–4509.

- Huang, Q., Walzer, K., Pfeiffer, M., Leo, K., Hofmann, M. & Stübinger, T. (2006) Performance improvement of top-emitting organic light-emitting diodes by an organic capping layer: An experimental study. *Journal of Applied Physics*, **100**, 064507.
- James, R.W. (1982) *The optical principles of the diffraction of x-rays*. Ox Bow Press, Woodbridge, Conn.
- Jo, P.S., Sung, J., Park, C., Kim, E., Ryu, D.Y., Pyo, S., Kim, H.-C. & Hong, J.M. (2008) Controlled Topology of Block Copolymer Gate Insulators by Selective Etching of Cylindrical Microdomains in Pentacene Organic Thin Film Transistors. *Advanced Functional Materials*, **18**, 1202–1211.
- Joseph Kline, R., McGehee, M.D. & Toney, M.F. (2006) Highly oriented crystals at the buried interface in polythiophene thin-film transistors. *Nature Materials*, **5**, 222–228.
- Joshi, S., Grigorian, S. & Pietsch, U. (2008) X-ray structural and crystallinity studies of low and high molecular weight poly(3-hexylthiophene). *physica status solidi (a)*, **205**, 488–496.
- Joshi, S., Grigorian, S., Pietsch, U., Pingel, P., Zen, A., Neher, D. & Scherf, U. (2008) Thickness Dependence of the Crystalline Structure and Hole Mobility in Thin Films of Low Molecular Weight Poly(3-hexylthiophene). *Macromolecules*, **41**, 6800–6808.
- Juers, D.H. & Weik, M. (2011) Similarities and differences in radiation damage at 100 K versus 160 K in a crystal of thermolysin. *Journal of Synchrotron Radiation*, **18**, 329–337.
- Kanai, K., Miyazaki, T., Suzuki, H., Inaba, M., Ouchi, Y. & Seki, K. (2009) Effect of annealing on the electronic structure of poly(3-hexylthiophene) thin film. *Phys. Chem. Chem. Phys.*, **12**, 273–282.
- Kaune, G., Ruderer, M.A., Metwalli, E., Wang, W., Couet, S., Schlage, K., Röhlberger, R., Roth, S.V. & Müller-Buschbaum, P. (2009) In Situ GISAXS Study of Gold Film Growth on Conducting Polymer Films. *ACS Applied Materials & Interfaces*, **1**, 353–360.
- Khazins, D.M., Becker, B.L., Diawara, Y., Durst, R.D., He, B.B., Medved, S.A., Sedov, V. & Thorson, T.A. (2004) A parallel-plate resistive-anode gaseous detector for X-ray imaging. *IEEE Transactions on Nuclear Science*, **51**, 943 – 947.
- Kiessig, H. (1931) Interferenz von Röntgenstrahlen an dünnen Schichten. *Annalen der Physik*, **10**, 769–788.
- Kim, J.B., Guan, Z.-L., Lee, S., Pavlopoulou, E., Toney, M.F., Kahn, A. & Loo, Y.-L. (2011) Modular construction of P3HT/PCBM planar-heterojunction solar cells by lamination allows elucidation of processing-structure-function relationships. *Organic Electronics*, **12**, 1963–1972.

- Kline, R.J., McGehee, M.D., Kadnikova, E.N., Liu, J. & Fréchet, J.M.. (2003) Controlling the Field-Effect Mobility of Regioregular Polythiophene by Changing the Molecular Weight. *Advanced Materials*, **15**, 1519–1522.
- Kowarik, S., Broch, K., Hinderhofer, A., Schwartzberg, A., Ossó, J.O., Kilcoyne, D., Schreiber, F. & Leone, S.R. (2010) Crystal Grain Orientation in Organic Homo- and Heteroepitaxy of Pentacene and Perfluoropentacene Studied with X-ray Spectromicroscopy. *The Journal of Physical Chemistry C*, **114**, 13061–13067.
- Kraker, E., Haase, A., Jakopic, G., Krenn, J.R., Köstler, S., Konrad, C., Heusing, S., Oliveira, P.W. & Veith, M. (2009) Organic photodiodes on flexible substrates. *Thin Solid Films*, **518**, 1214–1217.
- Kraker, E., Haase, A., Lamprecht, B., Jakopic, G., Konrad, C. & Köstler, S. (2008) Integrated organic electronic based optochemical sensors using polarization filters. *Applied Physics Letters*, **92**, 033302.
- Laibinis, P.E., Graham, R.L., Biebuyck, H.A. & Whitesides, G.M. (1991) X-ray Damage to CF₃CO₂-Terminated Organic Monolayers on Si/Au: Principal Effect of Electrons. *Science*, **254**, 981–983.
- Lamprecht, B., Abel, T., Kraker, E., Haase, A., Konrad, C., Tscherner, M., Köstler, S., Ditlbacher, H. & Mayr, T. (2010) Integrated fluorescence sensor based on ring-shaped organic photodiodes. *physica status solidi (RRL) – Rapid Research Letters*, **4**, 157–159.
- Lamprecht, B., Kraker, E., Sagmeister, M., Köstler, S., Galler, N., Ditlbacher, H., Ungerböck, B., Abel, T. & Mayr, T. (2011) Integrated waveguide sensor utilizing organic photodiodes. *physica status solidi (RRL) – Rapid Research Letters*, **5**, 344–346.
- van Langevelde, R. & Klaassen, F.M. (1997) Effect of gate-field dependent mobility degradation on distortion analysis in MOSFETs. *IEEE Transactions on Electron Devices*, **44**, 2044–2052.
- Langford, R. & Clinton, C. (2004) In situ lift-out using a FIB-SEM system. *Micron*, **35**, 607–611.
- Leenaers, A.J.G. & de Boer, D.K.G. (1997) Applications of Glancing Incidence X-Ray Analysis. *X-Ray Spectrometry*, **26**, 115–121.
- Li, H., Brédas, J.-L. & Lennartz, C. (2007) First-principles theoretical investigation of the electronic couplings in single crystals of phenanthroline-based organic semiconductors. *The Journal of Chemical Physics*, **126**, 164704.
- Liu, G., Rodriguez, J.A., Dvorak, J., Hrbek, J. & Jirsak, T. (2002) Chemistry of sulfur-containing molecules on Au(111): thiophene, sulfur dioxide, and methanethiol adsorption. *Surface Science*, **505**, 295–307.
- Mäkinen, A., Melnyk, A., Schoemann, S., Headrick, R. & Gao, Y. (1999) Effect of crystalline domain size on the photophysical properties of thin organic molecular films. *Physical Review B*, **60**, 14683–14687.

- Mandelbrot, B.B. (1991) *Die fraktale Geometrie der Natur*. Birkhäuser, Basel.
- Marchl, M., Golubkov, A.W., Edler, M., Griesser, T., Pacher, P., Haase, A., Stadlober, B., Beleggratis, M.R., Trimmel, G. & Zojer, E. (2010) Photochemical control of the carrier mobility in pentacene-based organic thin-film transistors. *Applied Physics Letters*, **96**, 213303.
- Miller, W.H. (1839) *A treatise on crystallography*. J. & J.J. Deighton; J.W. Parker, Cambridge, London.
- Minakata, T., Imai, H., Ozaki, M. & Saco, K. (1992) Structural studies on highly ordered and highly conductive thin films of pentacene. *Journal of Applied Physics*, **72**, 5220.
- Mizuguchi, J. (2005a) Dibenzimidazo[2,1-a:2',1'-a']anthra[2,1,9-def:6,5,10-d'e'f']diisoquinoline-10,21-dione: trans form (I). *Acta Crystallographica Section E Structure Reports Online*, **61**, 1066–1067.
- Mizuguchi, J. (2005b) Dibenzimidazo[2,1-a:1',2'-b']anthra[2,1,9-def:6,5,10-d'e'f']diisoquinoline-6,11-dione: cis form (II). *Acta Crystallographica Section E Structure Reports Online*, **61**, 1064–1065.
- Moser, A. (2012) *Crystal Structure Solution Based on Grazing Incidence X-ray Diffraction*. Dissertation, Graz University of Technology, Graz University of Technology.
- Moser, A., Flesch, H.-G., Neuhold, A., Marchl, M., Ausserlechner, S.J., Edler, M., Griesser, T., Haase, A., Smilgies, D.-M., Jakobovič, J. & Resel, R. (2012) Crystallization of pentacene thin films on polymeric dielectrics. *Synthetic Metals*, **161**, 2598–2602.
- Moser, A., Werzer, O., Flesch, H.-G., Koini, M., Smilgies, D.-M., Nabok, D., Puschnig, P., Ambrosch-Draxl, C., Schiek, M., Rubahn, H.-G. & Resel, R. (2009) Crystal structure determination from two-dimensional powders: A combined experimental and theoretical approach. *The European Physical Journal Special Topics*, **167**, 59–65.
- Mottaghi, M. & Horowitz, G. (2006) Field-induced mobility degradation in pentacene thin-film transistors. *Organic Electronics*, **7**, 528–536.
- Moulin, J.-F., Dinelli, F., Massi, M., Albonetti, C., Kshirsagar, R. & Biscarini, F. (2006) In situ X-ray synchrotron study of organic semiconductor ultra-thin films growth. *Nuclear Instruments and Methods in Physics Research Section B: Beam Interactions with Materials and Atoms*, **246**, 122–126.
- Müller, R., Weckert, E., Zellner, J. & Drakopoulos, M. (2002) Investigation of radiation-dose-induced changes in organic light-atom crystals by accurate d-spacing measurements. *Journal of Synchrotron Radiation*, **9**, 368–374.
- Nabok, D., Puschnig, P., Ambrosch-Draxl, C., Werzer, O., Resel, R. & Smilgies, D.-M. (2007) Crystal and electronic structures of pentacene thin films from grazing-incidence x-ray diffraction and first-principles calculations. *Physical Review B*, **76**, 235322.

- Nečas, D. & Klapetek, P. (2012) Gwyddion: an open-source software for SPM data analysis. *Central European Journal of Physics*, **10**, 181–188.
- Neuhold, A., Fladischer, S., Mitsche, S., Flesch, H.-G., Moser, A., Novak, J., Smilgies, D.M., Kraker, E., Lamprecht, B., Haase, A., Grogger, W. & Resel, R. (2011) Structure and morphology of an organic/inorganic multilayer stack: An x-ray reflectivity study. *Journal of Applied Physics*, **110**, 114911.
- Neuschitzer, M. (2012) *Grazing incidence in-plane X-ray diffraction on ultra-thin organic films using standard laboratory equipment*. Master Thesis, Graz University of Technology, Graz University of Technology.
- Neuschitzer, M., Moser, A., Neuhold, A., Kraxner, J., Stadlober, B., Oehzelt, M., Salzmann, I., Resel, R. & Novák, J. (2012) Grazing-incidence in-plane X-ray diffraction on ultra-thin organic films using standard laboratory equipment. *Journal of Applied Crystallography*, **45**, 367–370.
- Novák, J. (2010) XRR and XRR software comparison.
- O'Neill, P., Stevens, D.L. & Garman, E.F. (2002) Physical and chemical considerations of damage induced in protein crystals by synchrotron radiation: a radiation chemical perspective. *Journal of Synchrotron Radiation*, **9**, 329–332.
- Okamura, K. & Hahn, H. (2010) Carrier transport in nanocrystalline field-effect transistors: Impact of interface roughness and geometrical carrier trap. *Applied Physics Letters*, **97**, 153114.
- Pacher, P., Lex, A., Proschek, V., Etschmaier, H., Tchernychova, E., Sezen, M., Scherf, U., Grogger, W., Trimmel, G., Slugovc, C. & Zojer, E. (2008) Chemical Control of Local Doping in Organic Thin-Film Transistors: From Depletion to Enhancement. *Advanced Materials*, **20**, 3143–3148.
- Pan, L. & Sun, Z. (2009) Solvent and temperature-dependent conductive behavior of poly(3-hexylthiophene). *Journal of Physics and Chemistry of Solids*, **70**, 1113–1116.
- Parratt, L. (1954) Surface Studies of Solids by Total Reflection of X-Rays. *Physical Review*, **95**, 359–369.
- Perlich, J., Memesa, M., Diethert, A., Metwalli, E., Wang, W., Roth, S.V., Timmann, A., Gutmann, J.S. & Müller-Buschbaum, P. (2009) Preservation of the Morphology of a Self-Encapsulated Thin Titania Film in a Functional Multilayer Stack: An X-Ray Scattering Study. *A European Journal of Chemical Physics and Physical Chemistry*, **10**, 799–805.
- Petráček, V. (1995) Observation of Cu-phthalocyanine single molecules and islands deposited on gold and highly-oriented pyrolytic graphite substrates. *International Journal of Electronics*, **78**, 267–272.
- Peumans, P., Yakimov, A. & Forrest, S.R. (2003) Small molecular weight organic thin-film photodetectors and solar cells. *Journal of Applied Physics*, **93**, 3693–3723.

- Pietsch, U., Holy, V. & Baumbach, T. (2004) *High-resolution X-ray Scattering : from Thin Films and Lateral Nanostructures*, 2. ed. Springer, New York.
- Possanner, S.K., Zojer, K., Pacher, P., Zojer, E. & Schürerer, F. (2009) Threshold Voltage Shifts in Organic Thin-Film Transistors Due to Self-Assembled Monolayers at the Dielectric Surface. *Advanced Functional Materials*, **19**, 958–967.
- Press, W.H., Teukolsky, S.A., Vetterling, W.T. & Flannery, B.P., B.P. (2007) *Numerical Recipes: The Art of Scientific Computing*, Third ed. Cambridge University Press.
- Resel, R. (2007) DHS1100: a new high-temperature attachment for materials science in the whole orientation space. *Journal of Applied Crystallography*, **40**, 202.
- Resel, R., Ottmar, M., Hanack, M., Keckes, J. & Leising, G. (1999) Preferred orientation of copper phthalocyanine thin films evaporated on amorphous substrates. *Journal of Materials Research*, **15**, 934-939.
- Resel, R., Tamas, E., Sonderegger, B., Hofbauer, P. & Keckes, J. (2003) A heating stage up to 1173 K for X-ray diffraction studies in the whole orientation space. *Journal of Applied Crystallography*, **36**, 80.
- Richter, A.G., Guico, R., Shull, K. & Wang, J. (2006) Thickness and Interfacial Roughness Changes in Polymer Thin Films during X-Irradiation. *Macromolecules*, **39**, 1545–1553.
- Riedel, B., Kaiser, I., Hauss, J., Lemmer, U. & Gerken, M. (2010) Improving the outcoupling efficiency of indium-tin-oxide-free organic light-emitting diodes via rough internal interfaces. *Optics Express*, **18**, A631–A639.
- Rim, S.-B., Fink, R.F., Schöneboom, J.C., Erk, P. & Peumans, P. (2007) Effect of molecular packing on the exciton diffusion length in organic solar cells. *Applied Physics Letters*, **91**, 173504.
- Saito, M., Kosaka, T., Matsubara, E. & Waseda, Y. (1995) Characterization of oxide film grown on stainless steel by a new in-house grazing incidence X-ray scattering (GIXS) apparatus. *Materials transactions - JIM*, **36**, 1.
- Salleo, A., Chabinyk, M.L., Yang, M.S. & Street, R.A. (2002) Polymer thin-film transistors with chemically modified dielectric interfaces. *Applied Physics Letters*, **81**, 4383–4385.
- Salleo, A., Kline, R.J., DeLongchamp, D.M. & Chabinyk, M.L. (2010) Microstructural Characterization and Charge Transport in Thin Films of Conjugated Polymers. *Advanced Materials*, **22**, 3812–3838.
- Salzmann, I. (2009) *Structural and Energetic Properties of Pentacene Derivatives and Heterostructures*. Dissertation, Humboldt-Universität zu Berlin, Mathematisch-Naturwissenschaftliche Fakultät I, Berlin.
- Sanyal, M.K., Basu, J.K., Datta, A. & Banerjee, S. (1996) Determination of small fluctuations in electron density profiles of thin films: Layer formation in a polystyrene film. *European Physics Letters (EPL)*, **36**, 265–270.

- Sax, S., Rugen-Penkalla, N., Neuhold, A., Schuh, S., Zojer, E., List, E.J.W. & Müllen, K. (2010) Efficient Blue-Light-Emitting Polymer Heterostructure Devices: The Fabrication of Multilayer Structures from Orthogonal Solvents. *Advanced Materials*, **22**, 2087–2091.
- Scharnberg, M., Hu, J., Kanzow, J., Rätzke, K., Adelung, R., Faupel, F., Pannemann, C., Hilleringmann, U., Meyer, S. & Pflaum, J. (2005) Radiotracer measurements as a sensitive tool for the detection of metal penetration in molecular-based organic electronics. *Applied Physics Letters*, **86**, 024104.
- Scherrer, P. (1918) Bestimmung der Größe und inneren Struktur von Kolloidteilchen mittels Röntgenstrahlen. *Nachrichten von der Gesellschaft der Wissenschaften*, **2**, 98–100.
- Schiefer, S., Huth, M., Dobrinevski, A. & Nickel, B. (2007) Determination of the Crystal Structure of Substrate-Induced Pentacene Polymorphs in Fiber Structured Thin Films. *Journal of the American Chemical Society*, **129**, 10316–10317.
- Schlomka, J.-P., Tolan, M., Schwalowsky, L., Seeck, O.H., Stettner, J. & Press, W. (1995) X-ray diffraction from Si/Ge layers: Diffuse scattering in the region of total external reflection. *Physical Review B*, **51**, 2311–2321.
- Schuster, M. & Gobel, H. (1995) Parallel-beam coupling into channel-cut monochromators using curved graded multilayers. *Journal of Physics D Applied Physics*, **28**, A270–A275.
- Servet, B., Horowitz, G., Ries, S., Lagorsse, O., Alnot, P., Yassar, A., Deloffre, F., Srivastava, P. & Hajlaoui, R. (1994) Polymorphism and Charge Transport in Vacuum-Evaporated Sexithiophene Films. *Chemistry of Materials*, **6**, 1809–1815.
- Servet, B., Ries, S., Trotel, M., Alnot, P., Horowitz, G. & Garnier, F. (1993) X-ray determination of the crystal structure and orientation of vacuum evaporated sexithiophene films. *Advanced Materials*, **5**, 461–464.
- Shao, W., Dong, H., Jiang, L. & Hu, W. (2011) Morphology control for high performance organic thin film transistors. *Chemical Science*, **2**, 590–600.
- Sinha, S.K., Sirota, E.B., Garoff, S. & Stanley, H.B. (1988) X-ray and neutron scattering from rough surfaces. *Physical Review B*, **38**, 2297–2311.
- Van Slyke, S.A., Chen, C.H. & Tang, C.W. (1996) Organic electroluminescent devices with improved stability. *Applied Physics Letters*, **69**, 2160–2162.
- Smilgies, D.-M., Blasini, D.R., Hotta, S. & Yanagi, H. (2005) Reciprocal space mapping and single-crystal scattering rods. *Journal of Synchrotron Radiation*, **12**, 807–811.
- Song, W., Li, Z., So, S.K., Qiu, Y., Zhu, Y. & Cao, L. (2001a) Dynamic SIMS characterization of interface structure of Ag/Alq₃/NPB/ITO model devices. *Surface and Interface Analysis*, **32**, 102–105.
- Song, Q.L., Li, F.Y., Yang, H., Wu, H.R., Wang, X.Z., Zhou, W., Zhao, J.M., Ding, X.M., Huang, C.H. & Hou, X.Y. (2005) Small-molecule organic solar cells with improved stability. *Chemical Physics Letters*, **416**, 42–46.

- Song, W., So, S.K., Moulder, J., Qiu, Y., Zhu, Y. & Cao, L. (2001b) Study on the interaction between Ag and tris(8-hydroxyquinoline) aluminum using x-ray photoelectron spectroscopy. *Surface and Interface Analysis*, **32**, 70–73.
- Soukupová, K., Sassi, A. & Jerábek, K. (2010) Modifications in the morphology of poly(styrene-co-divinylbenzenes) induced by gamma-ray irradiation. *Reactive & Functional Polymers*, **70**, 361–365.
- Stepanov, S. (1997) *Simulations of Non-specular X-ray Scattering from Multilayers with Interface Roughness*: http://sergey.gmca.aps.anl.gov/TRDS_sl.html.
- Stettner, J., Schwalowsky, L., Seeck, O.H., Tolan, M., Press, W., Schwarz, C. & vonKanel, H. (1996) Interface structure of MBE-grown CoSi₂/Si/CoSi₂ layers on Si(111): Partially correlated roughness and diffuse x-ray scattering. *Physical Review B*, **53**, 1398–1412.
- Studel, S., De Vusser, S., De Jonge, S., Janssen, D., Verlaak, S., Genoe, J. & Heremans, P. (2004) Influence of the dielectric roughness on the performance of pentacene transistors. *Applied Physics Letters*, **85**, 4400–4402.
- Tang, C.W. (1986) Two-layer organic photovoltaic cell. *Applied Physics Letters*, **48**, 183–185.
- Tang, C.W. & VanSlyke, S.A. (1987) Organic electroluminescent diodes. *Applied Physics Letters*, **51**, 913–915.
- Tang, C.W., VanSlyke, S.A. & Chen, C.H. (1989) Electroluminescence of doped organic thin films. *Journal of Applied Physics*, **65**, 3610–3616.
- Thomson, J.J. (1910) On the scattering of rapidly moving electrified particles. *Proceedings of the Cambridge Philosophical Society*, 15–465.
- Tolan, M. (1999) *X-ray scattering from soft-matter thin films : materials science and basic research*. Springer, Berlin/New York.
- Turak, A., Grozea, D., Feng, X.D., Lu, Z.H., Aziz, H. & Hor, A.M. (2002) Metal/AlQ₃ interface structures. *Applied Physics Letters*, **81**, 766–768.
- Venables, J.A., Spiller, G.D. & Hanbücken, M. (1984) Nucleation and growth of thin films. *Reports on Progress in Physics*, 399–459.
- Veres, J., Ogier, S.D., Leeming, S.W., Cupertino, D.C. & Mohialdin Khaffaf, S. (2003) Low-k Insulators as the Choice of Dielectrics in Organic Field-Effect Transistors. *Advanced Functional Materials*, **13**, 199–204.
- Vineyard, G. (1948) Small-Angle X-Ray Scattering from Amorphous Materials. *Physical Review*, **74**, 1076–1083.
- Vineyard, G. (1982) Grazing-incidence diffraction and the distorted-wave approximation for the study of surfaces. *Physical Review B*, **26**, 4146–4159.

- Waldauf, C., Scharber, M.C., Schilinsky, P., Hauch, J.A. & Brabec, C.J. (2006) Physics of organic bulk heterojunction devices for photovoltaic applications. *Journal of Applied Physics*, **99**, 104503.
- Wang, X.Z., Xie, Z.T., Wang, X.J., Zhou, Y.C., Zhang, W.H., Ding, X.M. & Hou, X.Y. (2007) Blocking of interfacial diffusion at Ag/Alq₃ by LiF. *Applied Surface Science*, **253**, 3930–3932.
- Wang, S.D., Yan, Y. & Tsukagoshi, K. (2010) Understanding contact behavior in organic thin film transistors RID H-2688-2011. *Applied Physics Letters*, **97**, 063307.
- Wedl, B., Resel, R., Leising, G., Kunert, B., Salzmann, I., Oehzelt, M., Koch, N., Vollmer, A., Duhm, S., Werzer, O., Gbabode, G., Sferrazza, M. & Geerts, Y. (2012) Crystallisation kinetics in thin films of dihexyl-terthiophene: the appearance of polymorphic phases. *RSC Advances*, **2**, 4404–4414.
- Weik, M., Ravelli, R.B.G., Kryger, G., McSweeney, S., Raves, M.L., Harel, M., Gros, P., Silman, I., Kroon, J. & Sussman, J.L. (2000) Specific chemical and structural damage to proteins produced by synchrotron radiation. *Proceedings of the National Academy of Sciences*, **97**, 623–628.
- Weik, M., Ravelli, R.B., Silman, I., Sussman, J.L., Gros, P. & Kroon, J. (2001) Specific protein dynamics near the solvent glass transition assayed by radiation-induced structural changes. *Protein Science*, **10**, 1953–1961.
- Weißmantel, C. & Hamann, C. (1995) *Grundlagen der Festkörperphysik*. Barth.
- Werzer, O., Matoy, K., Strohriegl, P. & Resel, R. (2007) Temperature treatment of semiconducting polymers: An X-ray reflectivity study. *Thin Solid Films*, **515**, 5601–5605.
- WinGixa. (2000) www.stanford.edu/group/glam/xlab/PhilipsLit/WinGIXA.pdf.
- Wu, Y., Liu, P. & Ong, B.S. (2006) Organic thin-film transistors with poly(methyl silsesquioxane) modified dielectric interfaces. *Applied Physics Letters*, **89**, 013505.
- Yan, H., Swaraj, S., Wang, C., Hwang, I., Greenham, N.C., Groves, C., Ade, H. & McNeill, C.R. (2010) Influence of Annealing and Interfacial Roughness on the Performance of Bilayer Donor/Acceptor Polymer Photovoltaic Devices. *Advanced Functional Materials*, **20**, 4329–4337.
- Yang, H., LeFevre, S.W., Ryu, C.Y. & Bao, Z. (2007) Solubility-driven thin film structures of regioregular poly(3-hexyl thiophene) using volatile solvents. *Applied Physics Letters*, **90**, 172116.
- Yang, F., Shtein, M. & Forrest, S.R. (2005) Morphology control and material mixing by high-temperature organic vapor-phase deposition and its application to thin-film solar cells. *Journal of Applied Physics*, **98**, 014906.
- Yoneda, Y. (1963) Anomalous Surface Reflection of X Rays. *Physical Review*, **131**, 2010–2013.

- Yook, K.S. & Lee, J.Y. (2011) High efficiency in solution processed blue phosphorescent organic light-emitting diodes using an alcohol soluble emitting layer. *Organic Electronics*, **12**, 1595–1599.
- Yoon, M.-H., Kim, C., Facchetti, A. & Marks, T.J. (2006) Gate Dielectric Chemical Structure–Organic Field-Effect Transistor Performance Correlations for Electron, Hole, and Ambipolar Organic Semiconductors. *J. Am. Chem. Soc.*, **128**, 12851–12869.
- Yoon, J., Yang, S.Y., Lee, B., Joo, W., Heo, K., Kim, J.K. & Ree, M. (2007) Nondestructive quantitative synchrotron grazing incidence X-ray scattering analysis of cylindrical nanostructures in supported thin films. *Journal of Applied Crystallography*, **40**, 305–312.
- Yoshida, H., Inaba, K. & Sato, N. (2007) X-ray diffraction reciprocal space mapping study of the thin film phase of pentacene. *Applied Physics Letters*, **90**, 181930.
- You, J.-D., Tseng, S.-R., Meng, H.-F., Yen, F.-W., Lin, I.-F. & Horng, S.-F. (2009) All-solution-processed blue small molecular organic light-emitting diodes with multilayer device structure. *Organic Electronics*, **10**, 1610–1614.
- Zen, A., Saphiannikova, M., Neher, D., Grenzer, J., Grigorian, S., Pietsch, U., Asawapirom, U., Janietz, S., Scherf, U., Lieberwirth, I. & Wegner, G. (2006) Effect of Molecular Weight on the Structure and Crystallinity of Poly(3-hexylthiophene). *Macromolecules*, **39**, 2162–2171.
- Zhao, J., Swinnen, A., Van Assche, G., Manca, J., Vanderzande, D. & Mele, B.V. (2009) Phase Diagram of P3HT/PCBM Blends and Its Implication for the Stability of Morphology. *Journal of Physical Chemistry B*, **113**, 1587–1591.
- Zhao, Y., Wang, G.-C. & Lu, T.-M. (2001a) *Characterization of Amorphous and Crystalline Rough Surface: Principles and Applications*. Academic Press.
- Zhao, Y., Wang, G.-C. & Lu, T.-M. (2001b) *Characterization of Amorphous and Crystalline Rough Surface: Principles and Applications*. Academic Press.
- Zharnikov, M. & Grunze, M. (2002) Modification of thiol-derived self-assembling monolayers by electron and x-ray irradiation: Scientific and lithographic aspects. *Journal of Vacuum Science & Technology B: Microelectronics and Nanometer Structures*, **20**, 1793–1807.
- Zhong, C., Duan, C., Huang, F., Wu, H. & Cao, Y. (2011) Materials and Devices toward Fully Solution Processable Organic Light-Emitting Diodes. *Chemistry of Materials*, **23**, 326–340.
- Zontone, F., Madsen, A. & Konovalov, O. (2010) Measuring the source brilliance at an undulator beamline. *AIP Conference Proceedings* pp. 603–606.

V. PUBLICATIONS

2012:

Simbrunner, C.; Hernandez-Sosa, G. .; Quochi, F. .; Schwabegger, G.; Botta, C. .; Oehzelt, M.; Salzmann, I.; Djuric, T.; Neuhold, A.; Resel, R.; Saba, M. M.; Mura, A.; Bongiovanni, G. .; Vollmer, A.; Sitter, H.: **Color Tuning of Nanofibers by Periodic OrganicOrganic Hetero-Epitaxy.**: ACS NANO, 6, (2012), p. 4629 - 4638

Moser, A.; Flesch, H.-G.; Neuhold, A.; Marchl, M.; Außerlechner, S. J.; Edler, M.; Griebler, T.; Anja, H.; Smilgies, D.-M.; Jan, J.; Resel, R.: **Crystallization of pentacene thin films on polymeric dielectrics.**: Synthetic Metals, 161, (2012), p. 2598 - 2602

Neuschitzer, M.; Moser, A.; Neuhold, A.; Kraxner, J.; Stadlober, B.; Oehzelt, M. .; Salzmann, I.; Resel, R.; Novak, J.: **Grazing-incidence in-plane X-ray diffraction on ultra-thin organic films using standard laboratory equipment.**: Journal of Applied Crystallography, 45, (2012), p. 1 - 4

Defaux, M.; Gholamrezaie, F.; Wang, J.; Kreyes, A.; Ziener, U.; Anokhin, D. V.; Ivanov, D. A.; Moser, A.; Neuhold, A.; Resel, R.; de Leeuw, D. M.; Meskers, S. C.; Moeller, M.; Mourran, A.: **Solution-Processable Septithiophene Monolayer Transistor.**: Advanced Materials, 24, (2012), p. 973 - 978

Neuhold, A.; Novak, J.; Flesch, H.-G.; Moser, A.; Djuric, T.; Grodd, L.; Grigorian, S.; Pietsch, U.; Resel, R.: **X-ray radiation damage of organic semiconductor thin films during grazing incidence diffraction experiments.**: Nuclear Instruments & Methods in Physics Research B, 284, (2012), p. 64 - 68

2011:

Gholamrezaie, F.; Andringa, A.-M.; Neuhold, A.; Roelofs, W. S.; Kemerink, M.; Blom, P. W.; de Leeuw, D. M.: **Charge Trapping by Self-Assembled Monolayers as the Origin of the Threshold Voltage Shift in Organic Field-Effect Transistors.**: small, 8, (2011), p. 241 - 245

Flesch, H.-G.; Mathijssen, S. G.; Gholamrezaie, F.; Moser, A.; Neuhold, A.; Novak, J.; Ponomarenko, S. A.; Shen, Q.; Teichert, C.; Hlawacek, G.; Puschnig, P.; Ambrosch-Draxl, C.; Resel, R.; de Leeuw, D. M.: **Microstructure and Phase Behavior of a Quinquethiophene-Based Self-Assembled Monolayer as a Function of Temperature.**: The Journal of Physical Chemistry C, 115, (2011), 46, p. 22925 - 22930

Neuhold, A.; Fladischer, S.; Mitsche, S.; Flesch, H.-G.; Moser, A.; Novak, J.; Smilgies, D. M.; Kraker, E.; Lamprecht, B.; Haase, A.; Grogger, W.; Resel, R.: **Structure and morphology of an organic/inorganic multilayer stack: An x-ray reflectivity study.**: Journal of Applied Physics, 110, (2011), 114911, p. 1 - 7

2010:

Sax, S.; Rugen-Penkalla, N.; Neuhold, A.; Schuh, S.; Zojer, E.; List, E.; Müllen, K.: **Efficient Blue-Light-Emitting Polymer Heterostructure Devices: The Fabrication of Multilayer Structures from Orthogonal Solvents.**: Advanced Materials, 22, (2010), 18, p. 2087 - 2091

2009:

Sax, S.; Neuhold, A.; List, E.: **Novel concepts for organic optical oxygen sensor devices.**: Proceedings of SPIE, 7418, (2009), p. 74180B/01 - 74180B/18

VI. CONFERENCES

Talks

2012:

Neuhold, A.

Morphology of Orthogonal Soluble Polymer Transistors.: International Conference on Organic Electronics 2012. Tarragona: 25.06.2012

Neuhold, A:

Structural Characterization of Organic/Organic Interfaces of Orthogonal Soluble Polymers.: winterschool on organic electronics: self-assembly and hybrid devices. Plannersalm, Donnersbach: 04.03.2012

Neuhold, A.

Structural Investigations on Interfaces of Orthogonal Soluble Polymer Stacks.: NFN Final Meeting. Leoben: 18.01.2012

2011:

Neuhold, A.

Characterization of Organic/Inorganic Interfaces by X-ray Reflectivity and Transmission Electron Microscopy.: 8th Autumn School on X-ray Scattering from Surfaces and Thin Layers. Smolenice: 04.10.2011

Neuhold, A.

Investigation on Organic/Organic Interfaces and Organic/Inorganic Interfaces by X-ray Diffraction.: ISOTEC Meeting WP4, Graz: 07.07.2011

2010:

Neuhold, A.

Organische Vielschichtdiode: X-ray Streuung an Heterostrukturen verglichen mit AFM und SEM Aufnahmen.: ISOTEC Meeting 2010. Reinischkogel: 25.11.2010

Neuhold, A.

Structural and Morphological Characterization of an Organic Multilayer Photodiode with X-Ray Scattering Techniques, SEM and AFM.: NFN Meeting. Schloss R thelstein, Admont: 29.09.2010

Neuhold, A.

Organic Heterostructure Photodiodes – Structure and Morphology of the Multilayer Device.: NFN Meeting. Graz: 04.05.2010

2009:

Neuhold, A.

Organic Semiconductors: Fundamentals and Applications (Polymer Multilayer OLEDs): International Conference of Physics Students 2009. Split: 14.08.2009

Neuhold, A.

Investigation on an Organic Hetero-Structure Photodiode by X-ray Diffraction.: ISOTEC Seminar November 2009. Reinischkogel: 19.11.2009

2008:

Neuhold, A.

Organic Semiconductors: Fundamentals and Applications (OLED based Sensors and Dark Spot Research).: International Conference of Physics Students. Krakau: 08.08.2008

Poster Presentations

2011:

Neuhold, A.; Novak, J.; Flesch, H.-G.; Moser, A.; Djuric, T.; Grigorian, S.; Grodd, L.; Pietsch, U.; Resel, R.: **X - ray radiation damage on organic thin films under inert conditions.**: Austrian Synchrotron User Meeting 2011. Wien, Bundesministerium für Wissenschaft und Forschung: 18.10.2011

Neuhold, A.; Fladischer, S.; Neuschitzer, M.; Salzmann, I.; Kraker, E.; Lamprecht, B.; Grogger, W.; Resel, R.: **Structural and Morphological Characterization of Organic/Inorganic Interfaces by X-ray Reflectivity and Transmission Electron Microscopy.**: European Conference on Molecular Electronics 2011. Barcelona, Spain: 06.09.2011

Neuhold, A.; Novak, J.; Flesch, H.-G.; Moser, A.; Djuric, T.; Grigorian, S.; Grodd, L.; Pietsch, U.; Resel, R.: **X-ray radiation damage of organic semiconductor thin films during grazing incidence diffraction experiments.**: E-MRS 2011 Spring Meeting. Nizza: 09.05.2011

2010:

Neuhold, A.; Fladischer, S.; Mitsche, S.; Matsko, N.; Flesch, H.-G.; Moser, A.; Smilgies, D. M.; Kraker, E.; Grogger, W.; Resel, R.: **Structural and morphological characterization of an organic multilayer photodiode with X-ray scattering techniques, electron microscopy and AFM.**: 10th Biennial Conference on High Resolution X-Ray Diffraction and Imaging (XTOP). Warwick (UK): 20.09.2010

Neuhold, A.; Novak, J.; Flesch, H.-G.; Grigorian, S.; Grodd, L.; Pietsch, U.; Resel, R.: **In-situ X-ray characterisation of voltage induced changes in organic semiconductors.**: 10th Biennial Conference on High Resolution X-Ray Diffraction and Imaging (XTOP). Warwick (UK): 20.09.2010

Neuhold, A.; Fladischer, S.; Mitsche, S.; Moser, A.; Flesch, H.-G.; Novak, J.; Kraker, E.; Smilgies, D. M.; Haase, A.; Grogger, W.; Resel, R.: **Organic Multilayer Photodiode: Interface Roughness and Electron Density Profile in a Stacked Device Structure.**: International Conference of Organic Electronics 2010. Paris, Frankreich: 22.06.2010

Neuhold, A.; Fladischer, S.; Mitsche, S.; Moser, A.; Flesch, H.-G.; Novak, J.; Kraker, E.; Haase, A.; Smilgies, D. M.; Grogger, W.; Resel, R.: **Organic Heterostructure Photodiodes – Thin Film Morphologies and Crystal Structures of the Organic Layers.**: Winterschool on Organic Electronics. Planneralm, Donnersbach: 06.03.2010

VII. CURRICULUM VITAE

Alfred Neuhold

Dipl.-Ing. (Physics)

alfredneuhold@gmx.at

born in 1982

in Graz/Austria

Austrian citizen



Higher Education

09|96 – 06|01 **Technical Collage**, electrical engineering, *BULME Graz-Göding, Austria*

10|02 – 06|09 **Studies of Physics**, *Graz University of Technology (TU Graz), Austria*,
Diploma thesis in the field of organic light emitting diodes and organic oxygen
sensors

09|09 – 10|12 **Doctoral thesis** of technical sciences in the field of X-ray Reflectivity and X-
ray Diffraction on thin organic films, *Graz University of Technology (TU
Graz), Austria*

Working & science-related activities

07|03 – 05|08 **Employee** (part time/full time), specialist for application engineering and
software solutions, *GE General Electric GmbH GE Energy services –
Optimization Software, Graz*, <http://www.ge-energy.com/>

05|08 – 06|09 **Employee** (part time), experiments and investigations in the field of organic
heterostructure light emitting diodes and organic oxygen sensors,
NanoTecCenter Weiz Forschungsgesellschaft mbH, Weiz, [http://www.ntc-
weiz.at/](http://www.ntc-weiz.at/)

3rd to 11th Nov. 09

Experimental stay, *Grazing Incidence Diffraction experiments on thin organic
films*. Cornell High Energy Synchrotron Source (CHESS), Ithaca, NY

1st to 12th Dec. 09

Experimental stay, *Grazing Incidence Diffraction experiments and X-ray
Reflectivity experiments on thin organic films*. European Synchrotron Radiation
Facility (ESRF), Grenoble, France

20th to 26th Jul. 10

Experimental stay, *Grazing Incidence Diffraction experiments and X-ray
Reflectivity experiments on thin organic films*. Hamburger
Synchrotronstrahlungslabor (HASYLAB), Hamburg, Germany

11th to 17th Nov. 10

Experimental stay, Grazing Incidence Diffraction experiments and X-ray Reflectivity experiments on thin organic films. Hamburger Synchrotronstrahlungslabor (HASYLAB), Hamburg, Germany

29th May to 3rd Jun. 12

Experimental stay, Grazing Incidence Diffraction experiments and X-ray Reflectivity experiments on thin organic films. Hamburger Synchrotronstrahlungslabor (HASYLAB), Hamburg, Germany

03|12-03|13 **Teaching, “Praktikum für Fortgeschrittene”** at the Graz University of Technology

Computer

OS	Windows (good), LINUX (basics)
Desktop	MS Office (Word, Excel, Powerpoint), CorelDraw
Programming	Matlab (good), AutoCAD(basics), Pspice(basics), EPLAN(basics)
Typography	LATEX (basics)

Languages

German	Mother Tongue
English	Very Good (<i>Diploma thesis in English</i>)
Spanish	Good (<i>11 months main residence and study at the UAB Barcelona, Spain</i>)

Publications

10	Publications (author or coauthor)
10	Poster presentations at international conferences
1	Scientific report
12	Talks at international conferences

Awards

Young Scientist Award 2011, European Materials Research Society, France

<http://www.emrs-strasbourg.com/>



(Dipl.-Ing. Alfred Neuhold)